



An overview of how parity-violating electron scattering experiments are performed at CEBAF

P.A. Adderley^a, D. Bullard^a, Y.C. Chao^b, C.H. Garcia^a, J. Grames^a, J. Hansknecht^a, A. Hofler^a, R. Kazimi^a, J. Musson^a, C. Palatchi^c, K. Paschke^c, M. Poelker^{a,*}, G. Smith^a, M.L. Stutzman^a, R. Suleiman^a, Y. Wang^a

^a Thomas Jefferson National Accelerator Facility, Newport News, VA 23606, USA

^b Fermi National Accelerator Laboratory, Batavia, IL 60510, USA

^c University of Virginia, Charlottesville, VA 22903, USA

ARTICLE INFO

Keywords:

Parity violating electron scattering
Parity violation
Accelerator-based methods for conducting
parity violation experiments

ABSTRACT

Parity-violating electron-scattering experiments represent an important focus of the nuclear physics experimental program at the Continuous Electron Beam Accelerator Facility (CEBAF) at Jefferson Lab. These experiments pose significant challenges because the scattering asymmetries can be very small, of the order parts-per-million and smaller. To succeed, the properties of the electron beam such as current, position, size and energy, must be very nearly identical in the two electron-polarization spin states (parallel and anti-parallel relative to the direction of beam motion at the scattering target). This paper describes the origins of unwanted helicity-correlated beam asymmetries present on the electron beam and methods to minimize them to acceptable levels.

1. Introduction

A wide range of electron-scattering experiments are performed at the Continuous Electron Beam Accelerator Facility (CEBAF) [1,2], including the study of charge distributions, nucleon form factors, structure functions, generalized parton distributions, and meson spectroscopy [3,4]. Experiments with polarized electron beams aim to measure spin-dependent scattering asymmetries that result when the direction of the polarization spin-axis (or *helicity*) is flipped parallel/anti-parallel relative to the electron momentum at the target. The scattering asymmetries related to elastic form factors and spin structure functions are comparatively large, of the order 1%, whereas asymmetries related to parity-violating phenomena can be much smaller.

When conducting parity-violating electron-scattering experiments [5], it is imperative that the electron beam possess identical properties (e.g., beam current, position, energy and size) in the two helicity spin-states in order to clearly distinguish the interesting physics asymmetry from a false asymmetry that can result from variations in the way the target and detector respond to dissimilar beam conditions. These unwanted helicity-correlated beam asymmetries must be maintained much smaller than the physics asymmetry being measured, which is typically of the order of several parts per million and smaller.

The superconducting linacs at CEBAF enable “continuous” beam delivery, with radio frequency (RF) energy applied to accelerating cavities

continuously and with electron bunches filling every RF period (with the addition of Hall D, there are some “empty buckets” now [6,7]), thereby providing experiments with relatively high average current but at low bunch charge. As a result, experiments are conducted in an environment with low accidental background rates compared to conditions at pulsed radio-frequency machines. In addition, because the RF is always applied to the superconducting radio-frequency (SRF) accelerating cavities and the beam is always present, there is little beam loading of the accelerator cavities resulting in very stable beam conditions. These characteristics make CEBAF ideal for conducting parity-violation experiments.

To date, ten parity-violating electron-scattering experiments have been completed at CEBAF and these experiments fall into three categories: (1) experiments performed that use the phenomenon of parity violation to measure the contribution of the strange quark to nucleon structure, (2) experiments to study the distribution of neutrons in nuclear matter, and (3) experiments that look for physics beyond the standard model. The measured physics asymmetries of these experiments are shown in Table 1.1 with asymmetries ranging from ~40,000 to 35 parts per billion [8–28, refs for each parity-violating electron-scattering experiment]. Historically, the successful completion of one parity violation experiment has led to a more demanding proposal for a future experiment, with the goal of measuring an even smaller physics asymmetry. This paper describes CEBAF hardware associated

* Corresponding author.

E-mail address: poelker@jlab.org (M. Poelker).

Table 1.1

The parity-violating electron scattering experiments performed at CEBAF, or proposed for CEBAF. The table includes beam specifications (energy, polarization and beam current), the physics target, the parity-violating physics asymmetry measured or expected by the experiment, A_{PV} , and helicity-correlated beam asymmetry values averaged over the duration of the experiment. The goals tabulated for the future experiments in the last 2 rows are aspirational.

PV experiment	Energy (GeV)	Pol (%)	I (μ A)	Target	A_{PV} (ppb)	Charge asym (ppb)	Position diff (nm)	Angle diff (nrad)	Size asym ($\delta\sigma/\sigma$)	Refs.
HAPPEX-I 1998–1999	3.3	38.8 68.8	100 40	^1H (15 cm)	15,050	200	12	3	$<10^{-3}$	[8–10]
G0-Forward 2003–2004	3.0	73.7	40	^1H (20 cm)	3000–40,000	300 ± 300	7 ± 4	3 ± 1	$<10^{-3}$	[11]
HAPPEX-II 2004–2005	3.03	87.1	55	$^1\text{H}, ^4\text{He}$ (20 cm)	1580, 6400	400	2	0.25	$<10^{-3}$	[12–14]
G0-Backward 2006–2007	0.359, 0.688	85.8	60	$^1\text{H}, ^2\text{H}$ (20 cm)	9700–37,400	-30 ± 300	47 ± 9	1.2 ± 0.5	$<10^{-3}$	[15]
HAPPEX-III 2009	3.484	89.4	100	^1H (25 cm)	23,800	200 ± 10	3	0.5 ± 0.1	$<10^{-3}$	[16]
PVDIS 2009	6.067	89.0	105	^2H (20 cm)	60,000–160,000	100	100	40	$<10^{-3}$	[17–19]
PREx-I 2010	1.056	89.2	70	^{208}Pb (0.5 mm)	657 ± 60	85 ± 1	4	1	$<10^{-4}$	[20]
QWeak 2010–2012	1.162	88.7	180	^1H (34 cm)	226.5 ± 9.3	20.5 ± 1.7	-4.6 ± 0.2	-0.07 ± 0.01	$<10^{-4}$	[21–24]
PREx-II 2019	0.953	89.7	70	^{208}Pb (0.5 mm)	550 ± 18	20.7 ± 0.2	2.2 ± 4	0.3 ± 0.3	$<6 \times 10^{-5}$	[25]
CREx 2019–2020	2.18	87.1	150	^{48}Ca (5 mm)	2668 ± 113	-88 ± 26	-5.2 ± 3.6	-0.13 ± 0.08	$<6 \times 10^{-5}$	[26]
MOLLER 2025–2027	11	90	65	^1H (125 cm)	35.6 ± 0.74	<10	<0.6	<0.12	$<10^{-5}$	[27]
SoLID 2030–2032	11	90	50	$^1\text{H}, ^2\text{H}$ (40 cm)	$500,000 \pm 3000$	<200	<3	<1	$<10^{-4}$	[28]

with parity-violating electron scattering experiments (PV experiments, hereafter) and strategies and methods that have enabled successful completion of these experiments.

2. Overview of CEBAF

CEBAF [1] is a multipass, recirculating-linac electron accelerator with racetrack-shape, composed of two nominally identical superconducting radio frequency (SRF) linac sections that each provide ~ 1.1 GeV energy gain per pass, and ten magnet-arc strings (see Fig. 2.1). Approved for construction in the 1980s, commissioned in 1990s and upgraded in 2012 [2], CEBAF supports simultaneous beam delivery to four experiment halls. Because of the nature of the Hall D physics program, Hall D always requests the highest electron beam energy, 12 GeV, obtained via eleven linac passes. Beams to Halls A, B and C can pass through the linac sections at most ten times, providing a maximum beam energy of 11 GeV. Lower electron beam energies are obtained using fewer passes, or by operating the linacs at lower accelerating gradient. PV experiments are performed only at the high current experiment Halls A and C.

The maximum beam current that can be delivered to an experiment hall (neglecting target considerations) is limited by the available RF klystron power used to excite the 400 SRF linac cavities that provide beam acceleration, the cooling capacity of the central helium liquefier and the end-station refrigerator, and the beam dumps at the high power Halls A and C. Based on these considerations, the maximum beam power for all four halls combined is 1 MW. Since beam current to Halls B and D is typically low ($< 1 \mu\text{A}$), the combined maximum current delivered to Hall A and C at 11 GeV is $\sim 90 \mu\text{A}$. Efforts are underway to raise these limits.

The original proposal for CEBAF did not include electron-spin polarization as a requirement, but shortly after project approval, it was recognized that electron-spin polarization would significantly enhance the science capabilities of the facility. Today a large portion of the physics program relies on electron-spin polarization. In fact, the thermionic electron gun that provided unpolarized electron beams was removed

from the accelerator in the late 1990s. Now, all experiments receive electron beams from a spin-polarized photoelectron gun even if polarization is not required.

Each experiment hall receives electron beam from the same photocathode inside a direct current (DC) high-voltage photogun, using four independent drive lasers with interleaved RF-time structure (more in Section 11). The drive lasers provide electron beams to the experiment halls at 499 MHz or 248.5 MHz, the third and sixth subharmonics of the 1497 MHz CEBAF accelerating cavity frequency. PV experiments (and most other experiments that request polarized electron beams) require longitudinal spin direction at the target. The spin direction is longitudinal when the electrons leave the photocathode but precesses by thousands of degrees in the recirculating arcs and transport lines leading to each hall, with the exact value of spin precession different for each hall. A spin manipulator at the injector, described in Section 9, is used to orient the polarization longitudinal at the experiment halls, and fortunately, there are linac energies that can provide significant longitudinal polarization to three halls simultaneously (Hall D does not require polarized beam) [29–31]. There is even more flexibility if the linac energies are “unbalanced”, i.e., operating at different gradient [32,33].

The accuracy of a PV experiment is ultimately limited by the knowledge of the electron beam polarization. As such, considerable effort has been devoted to polarimetry at CEBAF. At Halls A and C, beam polarization is measured using Compton-backscatter and Møller polarimeters [34–40], Hall B using a Møller polarimeter, and at the injector using a high-precision 5 MeV Mott-scattering polarimeter [41]. The injector Mott polarimeter was extremely useful in helping to evaluate the accuracy of the hall polarimeters during CEBAF commissioning [42]. All of the polarimeters used at CEBAF have undergone significant upgrades [43], with much of the improvement effort aimed at enabling PV experiments.

3. Photocathodes

The helicity-correlated beam asymmetries that can complicate efforts to conduct a PV experiment originate at the injector photocathode

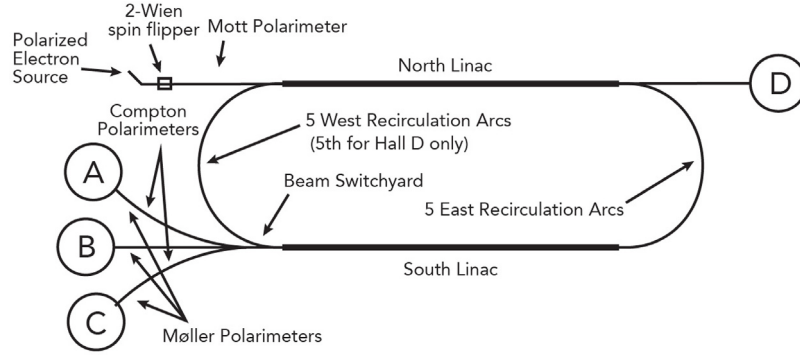


Fig. 2.1. Schematic representation of the CEBAF accelerator: spin-polarized photoinjector, two linac sections, multiple recirculation arcs, various polarimeters and the four experiment halls.

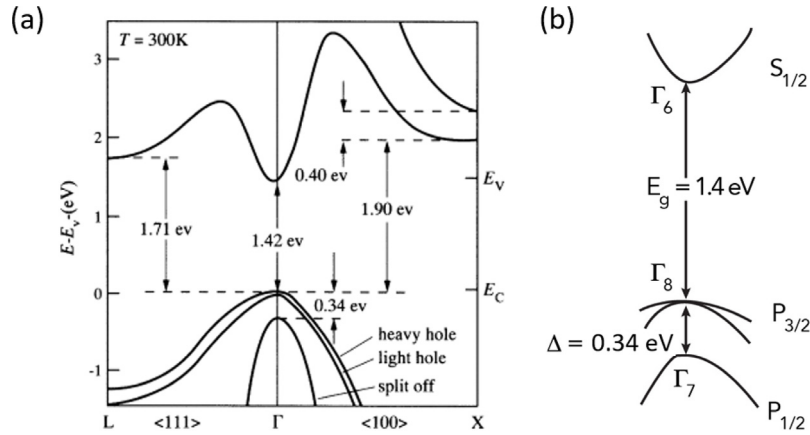


Fig. 3.1. Energy level diagrams of bulk GaAs [45,48]: (a) Conduction and valence band energies of GaAs as a function of wave vector, (b) “close-up” view near valence band maxima and conduction band minima.

Source: Reprinted with permission from Blakemore 1982.

which is composed of GaAs. GaAs is a direct-transition III-V semiconductor with zinc blende crystal structure [44,45]. It can absorb laser light across the broad visible spectrum but only the near-infrared wavelengths provide polarized photoemission [46,47]. This can be understood by looking at the energy level diagram of bulk GaAs with Fig. 3.1 showing detailed and simplified representations [45,48] of the band structure. Electron spin-orbit coupling splits the $P_{1/2}$ and $P_{3/2}$ energy levels of the valence band into two states separated by ~ 0.34 eV, which is large enough to avoid optical excitation from the lower energy $P_{1/2}$ state using a typical laser.

Polarized photoemission takes advantage of the quantum mechanical selection rules noting that for circularly polarized laser light, conservation of angular momentum requires an electron's spin-angular momentum quantum number to change by one unit, $\Delta m_j = +/\!-\!1$. Furthermore, some transitions are more favorable than others as indicated by the transition probabilities shown in Fig. 3.2a. So by using circularly-polarized laser light with near-bandgap energy, the conduction band can be preferentially populated with a particular spin state.

Electron polarization is defined as:

$$P = \frac{N_{\uparrow} - N_{\downarrow}}{N_{\uparrow} + N_{\downarrow}} \quad (3.1)$$

where N refers to the number of electrons in the conduction band of each spin state, “up” or “down”. For bulk GaAs, the theoretical maximum polarization is 50%, corresponding to three electrons of the desired spin state and one electron with opposite spin. In practice however, maximum polarization from bulk GaAs is less than 50%, owing to various depolarization mechanisms such as the Bir-Aronov-Pikus process [49], the D’Yakonov-Perel process [50], the Elliot-Yafet process [51], and radiation trapping [52]. A less academic description

simply attributes depolarization to imperfections within the photocathode material that result in reduced diffusion length which serves to prevent electrons from efficiently reaching the surface of the photocathode, thereby providing more opportunity for the electrons to depolarize on the way out.

The first photocathode used at CEBAF was inexpensive bulk GaAs providing very high quantum efficiency (QE) but polarization only $\sim 35\%$ [46,53]. A common figure-of-merit used to compare conditions associated with achieving a desired level of experimental accuracy is P^2I , where P is beam polarization and I is beam current. Because of the quadratic nature of beam polarization on the figure of merit, increasing beam polarization has a dramatic effect on scheduling, more so than beam current, which typically cannot simply be increased without limit (e.g., there are target limitations, and the accelerator power limitations mentioned above). As such, there is great incentive to increase polarization.

Maruyama et al. at the Stanford Linear Accelerator (SLAC) were the first to break the 50% polarization limit of bulk GaAs. They accomplished this by growing an epitaxial surface layer of InGaAs on GaAs [54]. The crystal-lattice mismatch between the two compounds introduced an axial strain that served to break the $P_{3/2}$ valence-band energy-level degeneracy as illustrated in Fig. 3.2b, thereby providing a means to limit optical excitation from the unwanted valence-band spin state. This new type of photocathode provided polarization 70% but with very small yield, or quantum efficiency (QE, the ratio of emitted electrons to incident photons). Soon after, similar demonstrations were reported by groups at Nagoya University in Japan [55], and St. Petersburg Technical University in Russia [56,57]. Accelerators around the world were quick to install these so-called “strained-layer”

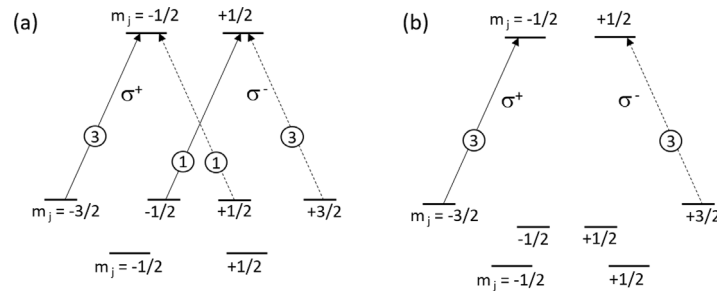


Fig. 3.2. (a) Simplified view of the valence band maxima and conduction band minima of bulk GaAs, showing individual spin-angular momentum states and transition probabilities, circled. For each circularly polarized light condition (σ^+ and σ^-) there is always one electron of the undesired spin state excited to the conduction band for every three electrons of the desired spin state, thereby providing theoretical maximum polarization of 50% $P = \frac{3-1}{3+1}$, (b) when strain is introduced, the valence-band energy-level degeneracy is eliminated enabling polarization > 50%.

photocathodes, with reports of beam polarization approaching 80% but with QE only of the order 0.1% (i.e., for every 1000 photons incident on the photocathode, one electron is emitted).

The single, relatively-thick, strained-layer photocathode suffered from the give and take of polarization versus QE. Higher QE could be obtained using a thicker strained-layer but at the expense of polarization. There was a limit to how thick the top strained layer could be – too thick and the strain would relax, with polarization returning to the typically low value of bulk GaAs.

The problem of strain relaxation was overcome by growing *superlattice* photocathodes composed of many thin-layer pairs of lattice-mismatched material. The combination of many thin-strained layers yielded both high polarization and high QE. The same institutions that pioneered single-strained-layer photocathodes were also the ones to pioneer strained-superlattice photocathodes – SLAC, Nagoya University, St. Petersburg Technical University [58–62].

The high-polarization photocathodes used at CEBAF were purchased from commercial vendors funded via the government's Small Business Innovation Research (SBIR) and Small Business Technology Transfer (STTR) programs: single-strained-layer photocathodes providing ~75% polarization and 0.1% QE from SPIRE/Bandwidth Semiconductor [63], and later SVT Associates [64] marketed a strained-superlattice photocathode providing ~90% polarization and 1% QE, which represents today's benchmark for success. Both of these photocathodes are based on GaAs grown on GaAsP (shown schematically, Fig. 3.3). Different stoichiometric combinations of Ga, As and P, as well as In and Al, can be used to modify the bandgap and correspondingly, the appropriate drive laser wavelength. Beam polarization at CEBAF as a function of calendar year is shown in Fig. 3.4. Although polarization ~90% is now fairly routine, there remains a vigorous R&D effort today focused at increasing photocathode polarization and QE [65–71].

4. Origins of helicity-correlated beam asymmetries

As described above, circularly-polarized laser light with photon energy comparable to the bandgap is required to generate polarized-electron beams from GaAs-based photocathodes. Because PV experiments (and other experiments) benefit from fast flipping of the direction of the electron polarization at the target, an electro-optical element called a *Pockels cell* [72,73] is used to convert linearly-polarized laser light into circularly-polarized light, flipping between the two helicity states at frequencies ~30 Hz or greater. Important details of the Pockels cell, including alignment procedures and the high-voltage switch, are described in more detail in Sections 12 and 13.

For nearly all experiments performed at CEBAF, a Pockels cell made of KD*P (potassium di-deuterium phosphide) [74–76], with electric field oriented longitudinal to the optical axis, was used to create circularly-polarized laser light. Recently, a Pockels cell composed of two RTP (rubidium titanyl phosphate) [77–79] crystals with electric field applied transverse to the optical axis has been employed, and chosen for its low piezo-electric coefficient and modest switching voltages

– more on this in Section 13. To appreciate the origin of helicity-correlated beam asymmetries, in the following text we focus on KD*P, but similar considerations apply to RTP Pockels cells as well. There are excellent reviews describing the origins of helicity-correlated beam asymmetries [80–84]; only a concise summary is presented here.

The KD*P crystal used at CEBAF is cylindrical (19.5 mm clear aperture, Cleveland Crystal model QX2035) with ring electrodes bonded to the circumference at each end to provide longitudinal electric field aligned parallel/antiparallel to the laser light passing through it. At CEBAF, voltage is applied to one ring electrode, with the other grounded. Pockels cells possess a voltage-induced birefringence, and when properly aligned can convert linearly-polarized laser light into circularly-polarized light, by delaying the phase of one transverse component of the light's electric field by 90° relative to the other. The so-called “quarter-wave” voltage depends on the wavelength of the laser light: for KD*P at 780 nm, the quarter-wave voltage is approximately ± 2000 V.

To avoid etalon effects stemming from multiple internal reflections, a 0.5 degree wedge is applied to one surface, although this is likely not that important, as the KD*P is relatively long and the optical pulse duration is fairly short, such that there is not much back-reflection overlap. The faces of the Pockels cell are anti-reflection coated, and despite the hydroscopic nature of KD*P, glass windows are not employed. Instead, the vendor recommends a SolGel [85] coating to minimize damage induced by humidity.

The optical axis of the Pockels cell must be precisely aligned to the propagation direction of the laser beam, and the voltage-induced phase retardation must be precisely set. The basic alignment procedure of the KD*P Pockels cell is as follows [86,87]. There are four cell parameters to adjust: pitch, yaw, roll and operating voltage. To provide coarse alignment of pitch and yaw, the Pockels cell is placed between two crossed-linear polarizers, with no voltage applied to the cell and a piece of cellophane tape placed on the input aperture to create an interference isogyre/isochromate pattern, which looks like a Maltese cross (isogyre) surrounded by a series of dark rings (isochromates). The cell pitch and yaw are adjusted to center the isogyre/isochromate pattern on the undisturbed portion of the transmitted laser beam. At this point the cellophane tape is removed from the input aperture of the cell, the upstream linear polarizer is removed, and the expected voltage for quarter-wave operation is applied to the cell, switching between both helicity states with \pm polarity. A spinning halfwave plate is then placed between the cell and downstream fixed linear polarizer, with the transmitted light monitored using a photodiode and oscilloscope, and producing a sinusoidal variation for each of the applied cell voltages. The cell roll and operating voltages are adjusted to minimize the amplitude of the sinusoidal waveforms. Following this coarse alignment of the cell, iterative adjustments to pitch, yaw, roll and operating voltage are made to further reduce the amplitude of the sinusoidal wave forms. The process is deemed effective when the observed sinusoidal variation in transmitted laser power becomes more

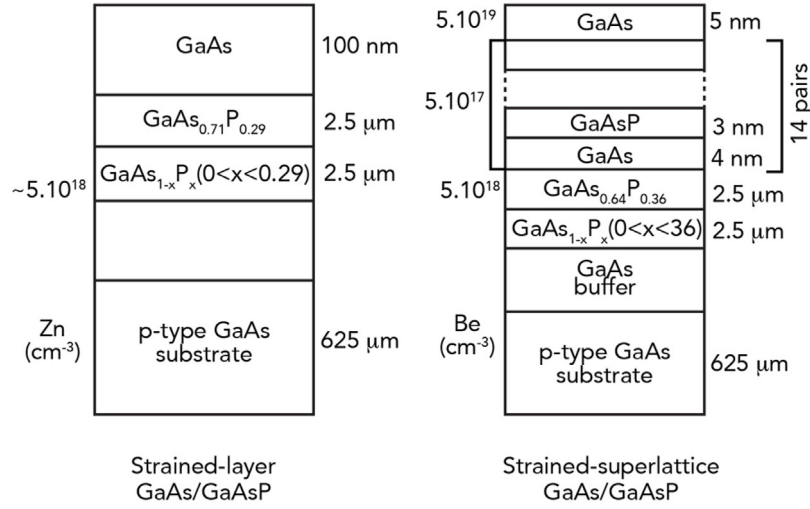


Fig. 3.3. Two types of GaAs photocathode structures used at CEBAF that provide high electron-beam polarization. The diagrams show the layer composition and thickness for these complicated heterostructures: (left) single-strained-layer GaAs/GaAsP photocathode with Zn dopant, and (right) strained-superlattice GaAs/GaAsP photocathode with Be dopant. The dopant concentration (atoms per cubic cm) is shown to the left of each image.

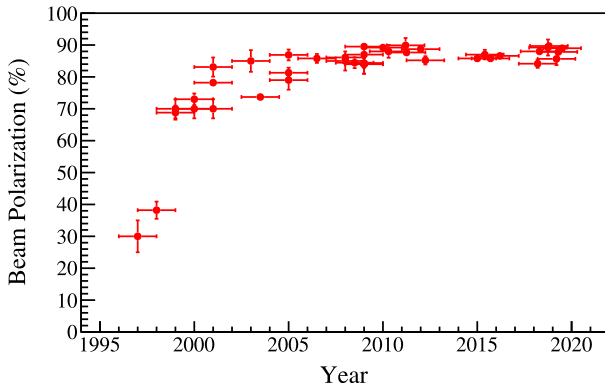


Fig. 3.4. Evolution of beam polarization at CEBAF using three different types of photocathodes: bulk GaAs, single-strained-layer GaAs/GaAsP and strained-superlattice GaAs/GaAsP. These measurements are mostly from Hall polarimeters and represent a small subset of polarization measurements made over the lifetime of CEBAF. The horizontal error bars do not represent uncertainty but rather the approximate dates over which measurements were made.

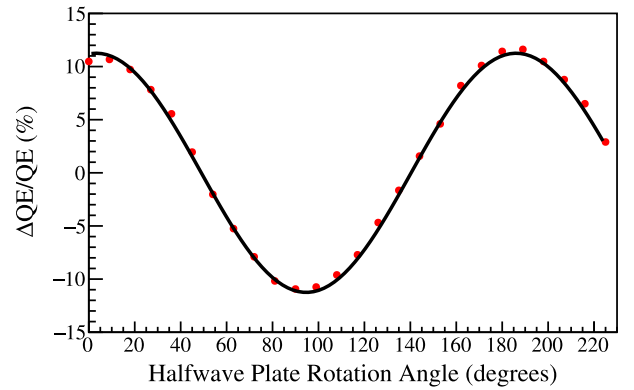


Fig. 4.1. Measurement of the QE anisotropy (or analyzing power) of a single-strained-layer GaAs/GaAsP photocathode. This describes the QE variation observed when the photocathode is illuminated with linearly polarized light, while the direction of linear polarization is varied using a rotating halfwave plate. The data points represent measurements, and the solid line is a sinusoidal fit. This photocathode was assigned an analyzing power of 11.3%.

and more sensitive to each adjustment. For a perfectly aligned Pockels cell producing perfectly circularly polarized light, there would be no sinusoidal modulation present on the oscilloscope waveform, and the signal strength from the photodiode would be half the value detected with the downstream linear polarizer removed. The degree of circular polarization (DoCP) can be quantified using the formula:

$$DoCP = \frac{2\sqrt{P_{max}P_{min}}}{P_{max} + P_{min}} \quad (4.1)$$

where P_{max} and P_{min} refer to the maximum and minimum values of the sinusoidal waveform observed on the oscilloscope, for each Pockels cell voltage state, positive and negative. It is relatively easy to obtain > 99.8% circular polarization in just minutes. The problem for parity-violating electron scattering experiments is that even for a well-aligned Pockels cell producing highly circularly-polarized light, there can remain a significant amount of linearly-polarized (DoLP) light:

$$DoLP = \sqrt{1 - DoCP^2} = \frac{P_{max} - P_{min}}{P_{max} + P_{min}} \quad (4.2)$$

For example, light with 99.8% DoCP provides 6.3% DoLP.

Residual linear-laser polarization is problematic because high-polarization photocathodes suffer “QE anisotropy” [88], also referred to as “photocathode analyzing power” [89], where the QE of the photocathode depends on the orientation of any residual linear polarization. QE anisotropy originates from the induced strain within the photocathode necessary to break the energy-level degeneracy of the ground state, to provide polarization > 50%. Whereas the QE anisotropy of bulk GaAs is zero, single-strained-layer photocathodes exhibit QE anisotropy of ~12% [89] and strained-superlattice photocathodes between 3 and 7% [90,91]. Photocathodes with smaller analyzing power provide are preferred because, for the same drive laser light, they provide smaller helicity correlated asymmetries. The plot in Fig. 4.1 shows the evaluation of photocathode analyzing power for a single-strained-layer GaAs/GaAsP photocathode, obtained by illuminating the photocathode with linearly-polarized light, while measuring photocathode QE as the orientation of the linear polarization is rotated through 180° using a halfwave plate. The analyzing power assigned to this photocathode was 11.3%.

To summarize, photocathode QE anisotropy combined with residual linearly-polarized light, is the dominant reason for helicity-correlated beam asymmetries, and in particular “charge asymmetry”, which describes unequal beam currents in the two electron beam helicity states.

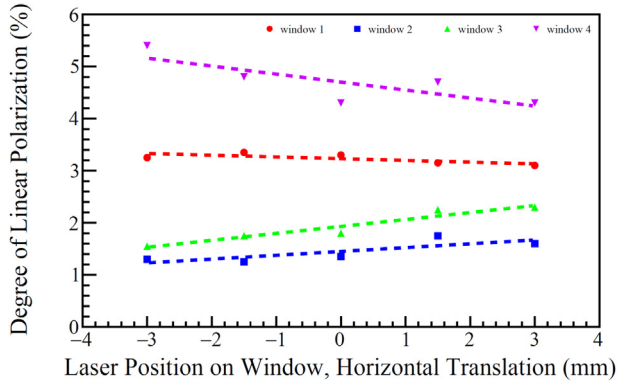


Fig. 4.2. Measurement of the DoLP after passing circularly-polarized light through four prospective vacuum windows, moving the laser beam horizontally across each window. Similar results were obtained with vertical translation of the laser beam. The original beamline-vacuum window used during CREx was window #4: it induced 5–6% additional DoLP. It was replaced with window #2 which induced only ~1% DoLP [93]. The lines displayed on the graph were applied to aid the eye.

Imperfections in Pockels cell electric-field uniformity, combined with Pockels cell alignment errors, create a polarization gradient across the profile of the laser beam which in turn creates dissimilar electron beam spatial profiles in the two helicity states that result in electron beam “position difference”. Position difference can also arise from physical modification of the cell dimensions when voltage is applied, leading to helicity-correlated beam steering or focusing (helicity-correlated “spot size asymmetry”).

Finally, the vacuum window used to deliver laser light to the photocathode can be the source of helicity-correlated beam asymmetries. This stems from the manner in which the glass is attached to the kovar metal ring of the vacuum window and combined with the force of atmosphere on one side of the glass, can introduce a strain which in turn leads to birefringence [92] that degrades circular polarization, adding linear polarization. Fig. 4.2 shows measurements of DoLP introduced by vacuum window birefringence, for four different windows, as a function of laser position across the window profile. Window #2 was chosen for installation on the baked beamline during a recent photoinjector upgrade, reducing induced DoLP from ~5% to 1% [93].

It is often stated that if perfect circular polarization were obtained, helicity-correlated beam asymmetries would be very small. This is largely true, even if QE anisotropy were present. However the birefringence of vacuum window is difficult to eliminate, and the four-laser nature of the CEBAF laser table – with pairs of laser beams combined with orthogonal linear polarization – prevents the use of “clean-up” polarizers required to make 100% circularly polarized light (the laser table is described in Section 11).

Helicity-correlated energy asymmetry is sometimes discussed. Its origin would stem from an unmanaged helicity-correlated charge asymmetry on any of the electron beams in the accelerator, even those delivered to neighboring halls. Helicity-correlated charge asymmetry could cause “beam loading” [94,95] in the SRF linacs. Beam loading, in the context of PV experiments, describes a condition in which the beam in one helicity state extracts stored energy from the SRF cavities, and this reduces the field in the cavities for the beam arriving in the next helicity state, providing less acceleration. The CEBAF low level RF systems [96] are designed to counter beam loading, but on a microscopic scale it is possible unmanaged helicity-correlated charge asymmetry could lead to different beam energies in each helicity state. In practice, it is difficult to tell the difference between helicity-correlated energy asymmetry and a helicity-correlated position asymmetry (difference) in the horizontal plane. Still, dedicated optical elements referred to as IAs (abbreviation for *intensity asymmetry*, more in Section 11) reside in each drive-laser beam path and they are used to minimize the charge

Table 5.1
JLab BCM cavity parameters.

Parameter	Symbol	Value
Cavity radius	a	7.74 cm
Unloaded Q	Q_0	3200
Loaded Q	Q_L	1600
External Q	Q_E	3200
Coupling coefficient	β	1.05
Source impedance	Z	50 Ω
Shunt resistance	R_{sh}	180 Ω
R/Q		93 Ω
Material	SS304	Stainless steel
Beam pipe radius	ρ	1.75 cm
Probe type		Magnetic loop

asymmetry for beams delivered to neighboring halls, and thus eliminate the potential for helicity-correlated energy asymmetry due to beam loading.

5. Beam monitoring

Like all accelerators, there are many beam-monitoring diagnostics used at CEBAF, including beam-current monitors [97], beam-position monitors [97], wire scanners (so called “harp”) to measure beam spatial profile [98], view screens that fluoresce when struck by electron beam [99], synchrotron light monitors located at bends [100], insertable Faraday cups and beam dumps. Of all these diagnostics, beam-current monitors (BCMs) and beam-position monitors (BPMs) are the most important monitoring diagnostics for PV experiments. These diagnostics permit non-invasive measurement and correction of helicity-correlated beam asymmetries throughout the duration of the experiment.

5.1. Beam-current monitors

Although the methods used to measure the yield of an experiment’s detector can vary from one experiment to the next, one thing every experiment has in common is the need to normalize the detector yield to the beam charge. At CEBAF, the beam charge is measured using “pillbox”-style TE₀₁₀ mode resonant RF cavity beam-current monitors (BCMs) tuned to the third harmonic of the beam bunch-repetition rate (1497 MHz), and temperature stabilized at 43 °C to preserve the tune. There are currently 33 of these cavities employed at CEBAF which provide stable, low noise, continuous and non-invasive measurement of the beam current. For PV experiments, the most important characteristics of the BCMs are linearity, precision, accuracy, and noise.

The BCM electronics (analog or digital, depending on the application) are typically situated outside the experimental hall to avoid radiation damage. The basic “Cavity Facts”, pertaining to expected BCM performance are shown in Table 5.1.

For PV experiments like the Qweak experiment [14–17], PREx2 [18] and CREx [19], the digital electronics used 18-bit, 1 MHz digital-to-analog converters (DACs) to generate the output voltage. Voltage levels proportional to the beam current and band-limited to 100 kHz were provided to 18-bit sampling analog-to-digital converters (ADCs) using heliex cables [101], which improve the signal-to-noise ratio at high frequencies relative to air-core coax. The BCM signals were matched to the detector pre-amplifier bandwidth of 26 kHz.

BCMs are calibrated against a parametric current transformer [102] at the experimental hall for electron beam currents greater than 20 μ A. At lower current, a Faraday cup at the injector is used for calibration. Typically, BCM measurements are made over 90 s intervals at successive beam currents spanning the range used in a given experiment and alternated with measurements of the beam-off baseline. After calibration, the BCM linearity is typically better than 0.5%.

BCM precision was studied using a Goubau Line [103], which employs a wire suspended through the cavity excited by a 1497 MHz sine

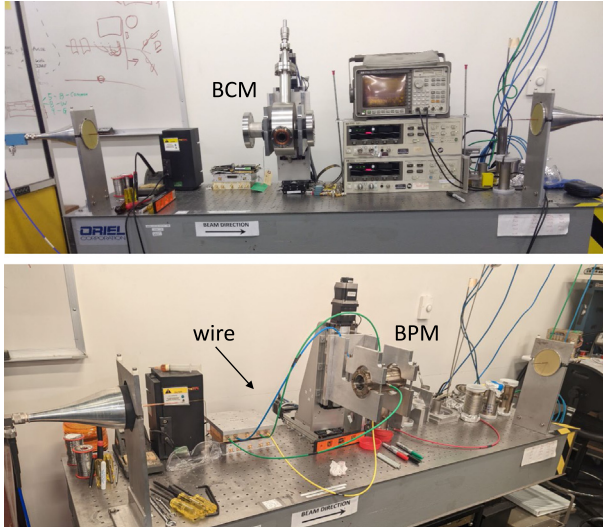


Fig. 5.1. Photographs of the Goubau Line test stand, showing a BCM (top) and BPM (bottom) under test.

wave to simulate the electron beam, with the cavity output monitored using the same electronics employed by the PV experiment (Fig. 5.1). The Goubau Line measurements indicate good agreement with actual beam-based measurements to within 2 dB. This agreement justifies using several rules-of-thumb (the formulas presented below) for which receiver electronics can be evaluated. Knowing the expected sensor output allows one to quickly establish a linearity constant for I_{beam} vs V_{out} , which in the case of a standard CEBAF BCM cavity is:

$$K = 447 \times 10^{-6} \frac{\mu A}{uV} \quad (5.1)$$

For typical PV experiments operating at beam current $> 10 \mu A$, the CEBAF BCMs provide plenty of signal.

BCM resolution was quantified by measuring the system signal-to-noise ratio. For this, the receiver electronics must be evaluated, as well as the amount of signal loss between the sensor and the receiver. For a perfect system (0 dB noise figure) operated at room temperature, the noise power for the typical 50 Ohm receiver possessing a 1 Hz bandwidth is given by [104]:

$$P_n = k_B T B = -174 \text{ dBm} \quad (5.2)$$

where k_b is Boltzmann's constant, T is 290 K, and B is the bandwidth of 1 Hz. Scaling for bandwidth is trivial, simply using the new bandwidth in place of 1 Hz. This noise expression can be combined with the derivative of the previous I_{beam} vs V_{out} relationship (Eq. (5.1)), to get an ultimate current resolution of [104]:

$$\delta I_{beam} = \frac{\delta V_{noise}}{K} \approx 1 \text{ pA} \quad (5.3)$$

However, real-world receivers are not perfect, so the receiver noise figure (in dB) must be considered. Similarly, cable losses, finite bit resolution and the fact that we intentionally design the receivers for the larger signals of CEBAF all impact the ultimate sensitivity. Years of experience indicates a minimum detectable signal of $\sim 500 \text{ pA}$ (1 Hz detection bandwidth).

Ideally, the helicity-correlated charge asymmetry, A_Q , is a property of the beam itself but as discussed below, it can also be affected by helicity-correlated position differences, especially for beam trajectories far from the BCM boresight. We discuss it here for completeness and reference the Qweak experiment [14–17] as representative of today's state of the art. Assuming a detector non-linearity of $\leq 1\%$, the Qweak experiment required that the overall helicity-correlated charge asymmetry be kept below 100 ppb in order to limit this contribution to the

uncertainty in the asymmetry measurement to no more than 1 ppb. Since the measured helicity-correlated charge asymmetry was typically a few thousand ppb over a 1 min interval, an active charge feedback system was used that relied on making small adjustments to Pockels cell voltages, as described in Section 12. The cumulative helicity-correlated charge asymmetry A_Q was measured in 80 s intervals, and the active feedback scheme adjusted the Pockels cell voltages (differently for each helicity) at the injector polarized electron source to null A_Q at the experimental hall. This generally works well to correct for charge asymmetries from the Pockels cell, but less well to correct charge asymmetries from helicity-correlated beam motion at the apertures in the polarized source. Over a month of running, A_Q was typically only 40 ppb.

BCM accuracy was one of the largest systematic uncertainties in the Qweak experiment. It was determined using the charge-normalized detector asymmetries A_j^{det} obtained from each BCMj:

$$\Delta A_{syst}^{BCM} = \sqrt{\frac{\sum_j (A_j^{det} - A_{avg}^{det})^2}{n(n-1)}} - \sigma_{BCM}^2 \quad (5.4)$$

for n BCMs. The summation index j runs from 1 to n . The asymmetries A_j^{det} are charge-normalized to each BCMj according to $A_j^{det} = (Y^+ / Q_j^+ - Y^- / Q_j^-) / (Y^+ / Q_j^+ + Y^- / Q_j^-)$, where Y^i and Q_j^i denote the detector yield Y^i and beam charge Q_j^i measured for beam helicity i using BCM j . The average asymmetry $A_{avg}^{det} = \sum_j A_j^{det} / n$. The $\sim 10\%$ BCM noise correction σ_{BCM} is subtracted because it is already included in the statistical uncertainty. During the Qweak experiment, the asymmetries A_j^{det} differed by several ppb depending on which BCM was used to form A_j^{det} . This represented an uncertainty floor $\Delta A_{syst}^{BCM} = 2.1 \text{ ppb}$ which limited the final uncertainty which could be achieved in that experiment.

It is presently not understood what limits the BCM accuracy. Using more BCMs does not help reduce this uncertainty, although obviously more than one BCM is required to be aware of and to measure the extent of the problem. However as shown in Fig. 5.2, the signal measured from each BCM is proportional to the cavity's electric field, which falls off non-linearly from the central axis of a TE₀₁₀ resonant cavity according to $E(r)/E_0 = J_0(k_n r)$, with $k_{010} = 2.045/R$. The cavity radius $R = 77.381 \text{ mm}$. For a beam displaced 2 mm from the cavity's central axis, the BCM signal drops 0.1%, and a sensitivity to helicity-correlated beam motion of -1 ppb/nm is expected, as shown in Fig. 5.3. Although alignment accuracy is typically about $250 \mu\text{m}$ along the ideal beamline, the mechanical and electrical axes are usually not the same. Furthermore, beam steering needed to center the beam on the experimental target can easily result in the beam being displaced from the central axis in any given BCM by 1 or 2 mm, and the displacement will be different in each BCM. In addition, the injector feedback system used to reduce the charge asymmetry (adjustments to Pockels cell voltages, as discussed in Section 12) can only use one representative BCM signal. Finally, the requirement to raster (dither) the beam to reduce the beam power density at the experimental target also means that the beam traverses each BCM at a different radius as a function of time and position along the beamline. During the Qweak experiment, all of the BCMs used to charge-normalize the experiment were downstream of the nominally 26 kHz raster magnets, for two reasons. First, the raster magnets have to be situated well upstream of the target in order to have enough lever arm to achieve the desired raster pattern at large beam momenta. The Qweak raster pattern was $4 \times 4 \text{ mm}^2$ at the target. Second, the BCMs used to charge-normalize the experiment should ideally be as close to the target as possible in order to record the beam that actually hits the target – some beam is lost upstream due to synchrotron radiation in the transport lines and scattering from residual gas due to imperfect beamline vacuum.

To summarize, since the beam axis passes through each cavity at a slightly different position, the beam charge measured by each cavity will inherently be slightly different, as will the charge asymmetry from

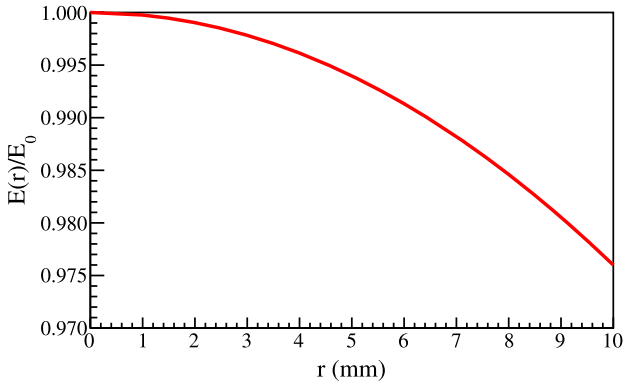


Fig. 5.2. Relative electric field in the CEBAF resonant BCM cavity as a function of radius from the central axis.

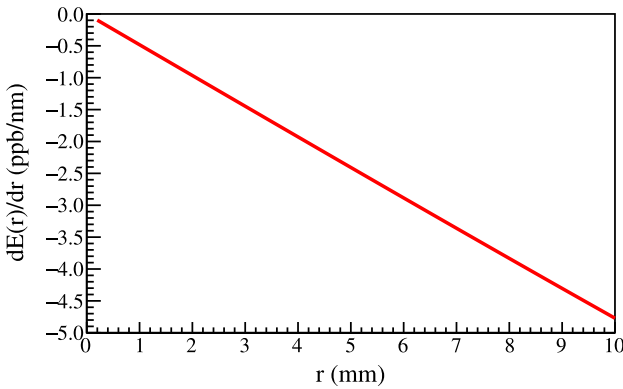


Fig. 5.3. Slope of the beam current measured from the electric field in the previous figure, as a function of distance from the boresight. This indicates how the beam current measurement depends on small position changes as the beam axis traverses the cavity at different distances from the cavity's central axis.

each BCM. For a precision PV experiment, a sensitivity of 1 ppb/nm (2 mm from the central BCM axis) can become a limiting uncertainty.

Brief test measurements to explore the sensitivity of BCM charge asymmetries to beam position were made during the Qweak experiment using kicker magnets in the injector which were normally used to reduce helicity-correlated beam motion. During these tests, different beam positions induced different charge asymmetries in the experimental hall for each BCM which were loosely consistent with the above sensitivity.

Helicity-correlated position and angle changes can be and have been improved since the Qweak experiment (see Section 13 describing fast helicity flipping using an RTP Pockels cell). Future tests are envisioned to further explore the BCM response to off-axis beam, which may help provide clues to break through the systematic uncertainty floor which the BCM accuracy currently represents.

BCM noise is important because it contributes to the statistical and systematic BCM uncertainty as mentioned in the previous section, and it affects the time required to achieve a given precision $\Delta A = \sigma_A / (P\sqrt{N})$ in an asymmetry measurement. Here P is the beam polarization, N refers to the number of helicity patterns, and σ_A represents the helicity-pattern asymmetry width. The latter is the quadrature sum of the statistics per helicity pattern accumulated in the detectors corrected for the helicity-reversal switching time and detector resolution, the width from noise (density fluctuations) in the liquid hydrogen target, and the beam-current monitor resolution. The beam-current monitor

instrumental resolution is determined from the double difference (DD) between a pair of BCMs

$$DD_{ij} = (Q_1^+ - Q_1^-) / (Q_1^+ + Q_1^-) - (Q_2^+ - Q_2^-) / (Q_2^+ + Q_2^-) = A_Q^1 - A_Q^2, \quad (5.5)$$

where Q_i^j denotes the beam charge measured from BCM i for helicity j , and A_Q^i is the charge asymmetry for BCM i . The DD is insensitive to fluctuations in Q and thus represents just the instrumental resolution of BCMs i & j . The noise of an individual BCM i was estimated as $DD_{ij}/\sqrt{2}$.

During the most precise asymmetry measurement performed at CEBAF to date – the Qweak experiment [14–17] – the helicity was reversed up to 960/s and pseudo-random helicity patterns (+--+ or -+--) were formed in quartets at 240 Hz. Thus, there were approximately $N \sim 10^7$ asymmetry quartets per day at 50% efficiency. Polarization was $\sim 88\%$. The helicity-quartet detector statistics dominated σ_A at about 215 ppm corrected for the 70 μ s helicity-reversal switching time, 42 μ s electronics gate delay used to avoid distortion of the input signals at the beginning of each gate, and 10% detector resolution. The helicity-quartet target noise was measured to be ~ 55 ppm. Typical values for the helicity quartet BCM DD were ~ 60 ppm. Therefore, the impact of the BCM noise was small in the Qweak experiment because the detector statistics dominated the total statistical asymmetry width, and the BCM accuracy dominated the BCM systematic uncertainty.

5.2. Beam-position monitors (BPMs)

All experiments require beam-position monitors (BPMs) in order to implement the desired beam tune and to steer the beam through the different elements of the beamline onto the experimental target. Most experiments also employ position locks using BPMs and corrector magnets to keep the beam centered on the experimental target, especially at the higher beam currents characteristic of PV experiments. In addition to these basic applications, PV experiments also require BPMs in order to characterize helicity-correlated beam asymmetries which have to be minimized and corrected for beyond the suppression that can be achieved with careful tuning at the polarized source and use of a symmetric detector array in the experimental hall.

The false asymmetry A_{beam} which arises due to helicity-correlated beam asymmetries is determined from

$$A_{beam} = \sum_i \frac{\partial A_{raw}}{\partial \Delta \chi_i} \Delta \chi_i, \quad (5.6)$$

where χ_i denotes either beam position (X or Y), beam angle (X' or Y'), or beam energy (E) at the experimental target, $\partial A_{raw}/\partial \Delta \chi_i$ is the measured detector sensitivity to variations in beam parameter χ_i , and $\Delta \chi_i$ is the helicity-correlated difference measured for beam parameter χ_i . Note that the energy is treated as a position because the energy differences are measured as a position difference in the dispersive transport lines. Both the sensitivities and the differences are measured over the helicity pattern, typically quartets, (+--+ or -+--). The detector sensitivities can be measured either by making use of the 60 Hz (and higher harmonics) natural jitter always present in the beam, or by deliberate periodic modulation using four air-core magnets in the beamline. The latter method is preferred because correlations between beam parameters can be suppressed.

Just as charge asymmetries measured in the experimental hall can be reduced with helicity-dependent adjustments to the Pockels cell voltages, the helicity-correlated beam asymmetries in position and angle can be reduced by appropriately pulsing dipole magnets in the 5 MeV injector region to reduce helicity-correlated beam asymmetries measured in the experimental hall (see Section 14 below). These magnets are situated downstream of the injector apertures to avoid inducing additional charge asymmetries. During the Qweak experiment, use of these helicity magnets decreased the 8-h helicity quartet average position difference at the target from about 100 nm to about 25 nm

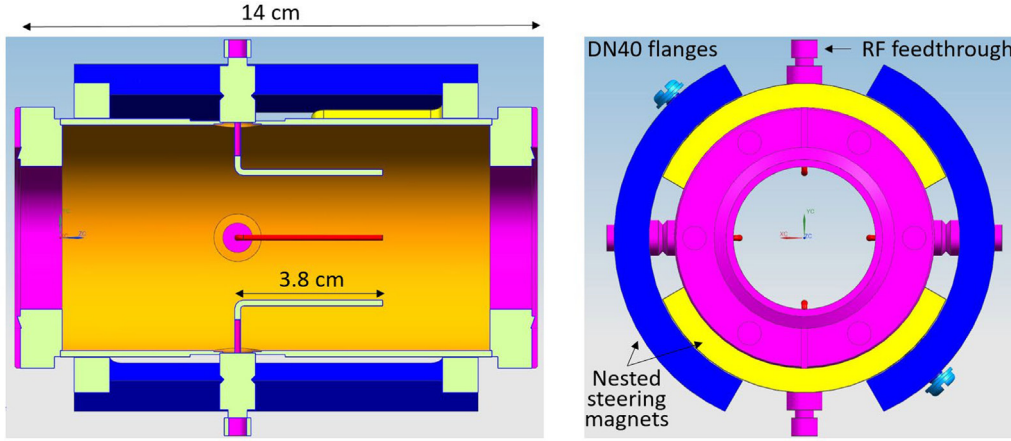


Fig. 5.4. Drawing of the antenna BPM used at the photoinjector. Nested dipole steering magnets can be placed on the BPM to save space along regions of congested beamline.

in X, and from about 35 nm to 10 nm in Y. The improvement was relatively stable for a given beam tune, and was typically re-optimized only every few days.

The beam energy is measured with an accuracy of $\sim 10^{-4}$ using wire scanners (harps) [98] at the entrance, exit, and dispersed focus of a magnetic arc, which effectively serves as a spectrometer just upstream of the entrance to the experimental hall. This is, however, an invasive measurement with arc quadrupoles off, and is only made infrequently. During a PV experiment, a BPM at the dispersed focus (typically 4 cm/%) of the magnetic arc is used to continuously and non-invasively measure the beam energy and the helicity-correlated beam asymmetries associated with it. This BPM is combined with other BPMs in the drift region just upstream of the target using beam transport matrices to deduce the beam energy at the target. A superconducting RF cavity in the accelerator periodically modulates the beam energy to facilitate the measurement of the sensitivity, and thus the correction to the measured physics asymmetry due to the helicity-correlated beam asymmetries associated with this parameter.

There are three styles of BPMs used at CEBAF: antenna-wire BPMs, stripline BPMs and cavity BPMs. The majority of BPMs used for PV experiments are antenna BPMs – described as type M20 (Fig. 5.4) – with four equally-spaced antennas which detect the presence of the beam via capacitive coupling to the electron beam’s electric field. The signal from each wire is proportional to both the electron beam current and the proximity of the electron beam to the wire in question. The antennas are oriented in the horizontal/vertical planes at the injector, or rotated 45° in the higher energy regions of the machine to avoid illumination of the antennas with synchrotron light [105].

The readout of each antenna pair is multiplexed using switched-electrode electronics every $4.2 \mu\text{s}$ to eliminate the effects of gain differences in the electronics. For modern PV experiments, each of the four antennas from each BPM are monitored in each helicity state using 18-bit sampling ADCs custom built to accommodate faster reversal rates. There are 24 BPMs monitored at the injector, and 23 in the Halls A and C beamlines.

To monitor beam position and angle at the target, multiple BPMs are employed. The beam position and the angle at the target are determined from a linear least squares fit of 4 or 5 BPMs located in a magnetic field-free drift region between ~ 1 and 10 m upstream of the target.

CEBAF BPMs (particularly the newer stripline variety) undergo a bench calibration using the Goubau Line described above [103]. The Goubau Line is particularly useful for evaluating low-Q structures, while emulating the characteristics of the nominal $160 \mu\text{m}$ -diameter electron beam. A high-resolution X–Y stepper system moves the BPM in $250 \mu\text{m}$ steps (with $0.25 \mu\text{m}$ resolution) to create the electromagnetic field map mesh for regression. A variety of analysis techniques have

been studied [106]. The Goubau Line measurements indicate the minimum position resolution σ (into ideal noiseless electronics) for the M15 style antenna BPM of:

$$\sigma \approx \frac{2\mu\text{m} \cdot uA}{\sqrt{\text{Hz}}} \quad (5.7)$$

Typical resolution values for a broadband, single bunch reading is 10^{-3} of the beam pipe radius or roughly $\simeq 100 \mu\text{m}$. For averaged readings on a typical time scale of 10 to 1000 ms, a resolution of 10^{-5} of the beam pipe radius or roughly $\simeq 1 \mu\text{m}$ can be reached, and this extends $\pm 5 \text{ mm}$ from the centerline of the BPM, the so-called “sweet spot” of the BPM.

BPM accuracy describes the ability to measure the electron beam absolute position relative to a mechanical fix-point or to any other absolutely known axis e.g. the symmetry axis of a quadrupole magnet. The stripline BPM sensors are CNC machined, complete with external fiducial dimples on the main corpus to facilitate precise placement on the beamline, and directly traceable from the prints to within CNC tool accuracy. Antenna BPMs however lack survey fiducials. Typical offsets of $200\text{--}400 \mu\text{m}$ can exist. During the Qweak experiment, using 2 of the 5 BPMs upstream of the target as a reference, offset corrections as large as 1 mm were required to bring all 5 BPMs into agreement. However, those corrections remained stable at the $25 \mu\text{m}$ level for the duration of the experiment. Stable offsets are of course what is required for the measurement of the helicity-correlated position and angle differences $\Delta\chi_i$. To ensure that BPM offset inaccuracy does not interfere with centering the beam properly on the target, carefully surveyed hole targets attached to the target ladder are used in conjunction with the beam raster to fine-tune the beam position in most experiments. Within the 5 mm boresight radius, accuracy is maintained at $\pm 50 \mu\text{m}$ for $1 \mu\text{A}$ CW beam [107].

BPM precision is a function of beam current and the helicity reversal frequency. This dependence was measured during the Qweak experiment (240 Hz helicity quartets) by comparing the position measured in one BPM to the projected position in that BPM using two nearby BPMs. All three BPMs were in a field-free drift region. The standard deviation of this difference was taken to be the resolution of one BPM [108]. At the $180 \mu\text{A}$ employed in the experiment, the helicity-quartet BPM resolution was $0.90 \mu\text{m}$ (X) and $0.96 \mu\text{m}$ (Y), or about 1 nm in an hour [$0.90 \mu\text{m}/\sqrt{(240 \text{ quartets/s} \times 3600 \text{ s/hr})}$] (Fig. 5.5).

6. Helicity generator

There is a versatile VME-based *Advanced Programmable Logic Generator* – or helicity-control board – located at the CEBAF injector used to change the spin-direction (aka *helicity*) of the electron beam and to control devices that minimize helicity-correlated beam asymmetries

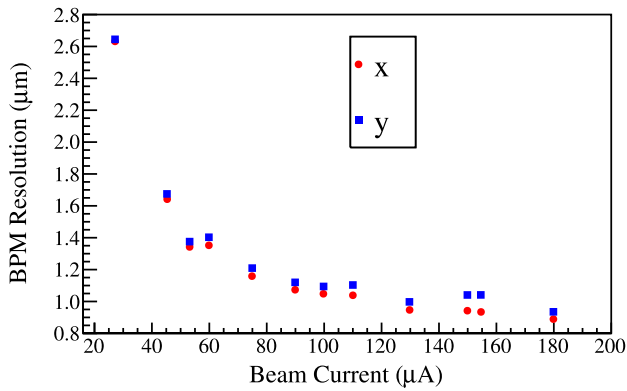


Fig. 5.5. Measured dependence of the resolution of a BPM as a function of beam current during the Qweak experiment. Resolution plotted per helicity quartet.

via feedback described in Sections 13 and 14. The helicity-control board [109] permits helicity spin-flipping at repetition rates from 1 to 2000 Hz, limited by characteristics of the Pockels cell and the speed of data acquisition systems related to experiments. Helicity flipping can be “line locked” to the power company 60 Hz alternating current (AC) voltage or free running, with repetitive or pseudo-random flipping in pairs, quartets or octets, and with direct or delayed reporting of the helicity information to the experiment halls and polarimeter data acquisition systems. The experimenters choose the settings of the helicity-control board based on adopted strategies they think best serve their goals. The helicity-control board and related electronic and laser-table optical elements are shown schematically in Fig. 6.1 with key features described below.

When conducting PV experiments it is vital to prevent electronic cross-talk that could transmit real-time helicity information to the “outside world” (e.g., experiment hall counting house, polarimeter DAQs), including via ground loops, that could produce false raw (detector) asymmetries. In designing the helicity-control board, the following precautions were taken (with many illustrated in Fig. 6.1):

- The helicity-control board is located within an electrically-isolated VME crate at the Injector Service Building, powered by an isolation transformer and floating at 62 VAC.
- The helicity-control board generates two real time helicity signals called *Helicity Flip* and its opposite, *nHelicity Flip*. In this manner, the current drawn by the board does not depend on the helicity state.
- The Pockels cell and so-called IA charge-asymmetry controllers at the injector drive-laser table are the only devices that receive a real-time helicity signal (*Helicity Flip*). The setpoint voltages for these devices pass through a galvanic-isolation card and there are no readbacks of these setpoint voltages. This card uses a precision isolation amplifier (ISO-124) to isolate signals from -10 V to $+10$ V with a bandwidth of up to 50 kHz.
- The helicity magnets are powered using an independent electrically-isolated VME crate powered by an isolation transformer that receives one of the two real-time helicity signals (*nHelicity Flip*).
- The beam helicity signal is generated by a pseudo-random bit generator, to prevent a correlation between the helicity signal and any other signal at the accelerator or experiment hall.
- The “outside world” receives only a delayed helicity signal (*Delayed Helicity*) so there is no knowledge of real time helicity.

- During the experiment, all helicity-correlated beam asymmetries (position, angle, charge, energy, and size – and thus beam scraping) are minimized so that helicity is the only real time property of the beam that is changing.

Besides the signals mentioned in the text above (*Helicity Flip*, *nHelicity Flip* and *Delayed Helicity*), the helicity-control board generates the following additional signals: *T_Settle*, *Pair Sync*, *Pattern Sync*, and a 20 MHz clock signal.

The signal *T_Settle* refers to the transition time between the two helicity states, and the time over which the beam polarization is stable is called *T_Stable*, such that $T_{Settle} + T_{Stable}$ is equal to the length of one helicity window, and which sets the frequency of the helicity board, $1/(T_{Settle} + T_{Stable})$. The board user interface allows the experimentalist to choose both times independently. The experimenters do not collect data during *T_Settle*. The choice of the *T_Settle* must be long enough to allow the Pockels cell voltage to “settle” and the choice of the helicity reversal frequency must be matched to the speed of data acquisition systems.

Pair Sync is a simple toggle signal (high or low). The DAQs in the experimental Halls use this toggle signal to check signal fidelity from the helicity board.

Pattern Sync indicates the start of each pattern. If the pattern is “pair”, then it is identical to *Pair Sync*.

The helicity-control board possesses an internal 20 MHz clock which is used as the reference clock for the analog-to-digital converters (ADCs) employed at the injector and experiment halls, to ensure that all systems are sampling at the same time. The 20 MHz clock signal is also used to synchronize the raster magnets at Hall A.

The signals produced by the helicity-control board are transmitted via fiber optic cable. The experiment halls receive only *T_Settle*, *Pair Sync*, *Pattern Sync*, and *Delayed Helicity*.

Helicity-board settings

Each experiment collaboration chooses the helicity-board settings for their experiment. To date, all parity violation experiments have requested “delayed reporting” of the helicity information since this is a prudent way to avoid unintended false asymmetries due to helicity-signal electronic pickup or crosstalk. Other settings are chosen with the common overarching desire to minimize the impact of 60 Hz power line “noise” which introduces unwanted beam motion that increases the width of the helicity-correlated position-asymmetry distribution. The helicity board was designed to provide three strategies to reduce the contribution of 60 Hz line noise on helicity-correlated position asymmetry;

1. Operate in Free Clock Mode, and integrate over 60 Hz noise per helicity window. Select $T_{Stable} = 33,330 \mu s$ (exactly two 60 Hz cycles). This provides a nearly exact cancellation and the data collected will have no information about 60 Hz line noise. This is what most experiments at Jefferson Lab have been using. (strictly speaking, the cancellation is not exact because the line frequency is not exactly 60 Hz, but varies by about $\pm 0.1\%$. All phases of the 60 Hz line are sampled since there is a continuous phase slip relative to the line power. *T_Settle* determines the magnitude of this phase slip.) Both Pair and Quartet patterns can be used however the Quartet Pattern provides exact cancellation of linear drifts over the timescale of the sequence. The Pair Pattern requires averaging over other pairs for cancellation of linear drifts. With *T_Settle* of 500 μs , the helicity reversal rate is 29.56 Hz. Thus the phase of the helicity signals will slip continuously with respect to the power line phase and all phases of power line will be sampled every 2.3 s.
2. Operate in Free Clock Mode and select T_{Stable} such that $f > 1$ kHz. In this manner, the helicity-board frequency is far from line harmonics. The contribution of the 60 Hz line noise does not

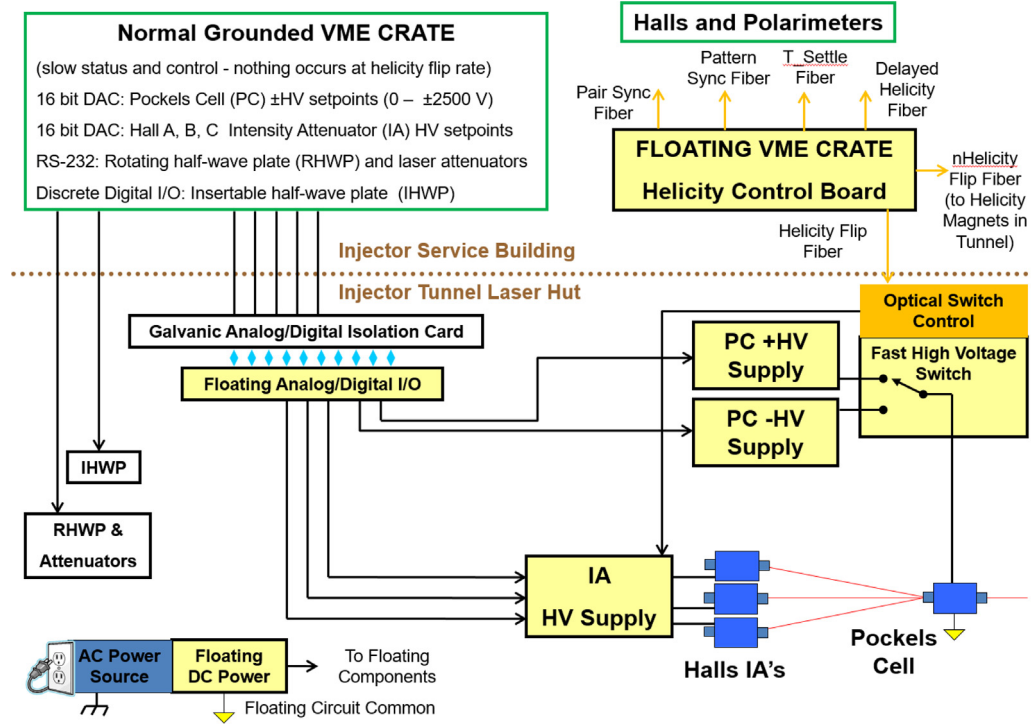


Fig. 6.1. Schematic of the helicity-information distribution system. “IA” references the laser-table optical devices used to minimize the helicity correlated charge asymmetry at neighboring experiment halls, DAQ: data acquisition system, IHWP: insertable-halfwave plate, RHWP: rotatable-halfwave plate, PC: Pockels cell, I/O: input/output, HV: high voltage.

Table 6.1
Line-synchronized mode options.

Helicity flip rate	Helicity pattern	T_{Stable} duration	Formalism for calculating the physics scattering asymmetry. Numbers represent the helicity state of chosen pattern
30 Hz	Pair or quartet	$T_{Stable} = 33,330 \mu s - T_{Settle}$	$A_{PV} = \frac{+1-2}{+1+2}$ or $A_{PV} = \frac{+1-2-3+4}{+1+2+3+4}$
120 Hz	Quartet	$T_{Stable} = 8330 \mu s - T_{Settle}$	$A_{PV} = \frac{+1-2-3+4}{+1+2+3+4}$
240 Hz	Octet	$T_{Stable} = 4167 \mu s - T_{Settle}$	$A_{PV} = \frac{+1-2-3+4-5+6+7-8}{+1+2+3+4+5+6+7+8}$

change by much from one window to the next and thus cancels when calculating the asymmetries. Normally, a quartet pattern is used in this case. The data will still have full information about the 60 Hz line noise.

- Operate in Line Synchronized Mode and cancel 60 Hz line noise using patterns shown in Table 6.1 below, where A_{PV} describes the physics asymmetry being measured and the various formulas describe how A_{PV} is calculated by combining different windows in the pattern. The 60 Hz noise does not cancel per window, however it cancels when the asymmetries are calculated. The start of each pattern is triggered by the Line Sync signal and thus each pattern always starts at the same line phase. In this mode, the helicity-board frequency will track the line frequency and the helicity-board frequency will have the same jitter as the line frequency.

Besides 60 Hz line noise, target-density fluctuations represent another noise contribution [110]. Choice (2) will work as well for other low frequency noises including the noise from target density fluctuations. This kind of noise is peaked at low frequency because it is a mechanical noise due to gas bubbles in the Hall cryogenic liquid target. Choices (1) and (3) are geared for 60 Hz noise; other noises will not cancel. These noises will increase the width of the helicity-correlated distributions as in the case of target-density fluctuations.

Other prominent single-low frequency noises will cause double-horned peak distributions. Method (3) is geared to 60 Hz and not very effective at canceling noise at other frequencies. For more details see Refs. [111–113].

As a specific example of the different helicity board settings for an experiment, consider the MOLLER experiment [27]. MOLLER expects to use the following settings: Free Clock Mode at 1920 Hz, $10 \mu s$ “ T_{Settle} ”, $510.85 \mu s$ “ T_{Stable} ”, 64-window pattern, and 128-window delay. For the helicity pattern, MOLLER requests three different options for the 64-window pattern:

- Type1: Thue–Morse-64 (+--+ +--+ -+--+ -+--+ -+--+ -+--+ -+--+ -+--+ or the complement)
- Type2: 16-Quad (+--+ +--+ -+--+ -+--+ -+--+ -+--+ -+--+ -+--+ or the complement).
- Type3: 32-Pair (+--+ +--+ -+--+ -+--+ -+--+ -+--+ -+--+ -+--+ or the complement)

These three choices for the 64-window pattern provide different levels of cancellation of low-frequency noise (including 60 Hz) with Type1

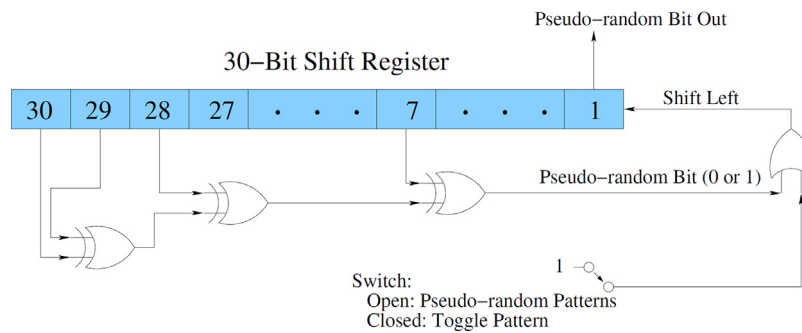


Fig. 6.2. A combination of “exclusive or” gates related to bits 30, 29, 28, and 7 of the shift register determines the first window of a requested helicity pattern.

having the highest level and Type3 the lowest. More details can be found in Ref. [114].

Helicity Board Registers

There are five registers on the helicity board that provide great flexibility. A five-bit read/write (R/W) register sets the “ T_{Settle} ” portion of the helicity period and a corresponding five-bit R/W register sets the duration of “ T_{Stable} ”. Settle-time selections range from 10 to 1,000 μs and associated stable periods range from 400 to 1,000,000 μs . A three-bit R/W register is used to set the helicity pattern: pair, quartet, octet, hexo-quad, octo-quad, and toggle and another three-bit R/W register is used to set the delay of reported helicity signal relative to the real time helicity. The delay time can be set to No Delay, 1 window, 2 windows, 4, 8, 12, 16, 24, 32, 40, 48, 64, 72, 96, 112, and 128 windows.

To eliminate any correlation between the helicity of the beam and any other device in the accelerator or in the experiment hall, a 30-bit shift register (Fig. 6.2) is used to generate pseudo-random combinations of helicity windows. The helicity selection is pseudo-random, and not explicitly “random”, because it is deterministic. Once a sequence of 30 bits is known, the next bits can be predicted, and the sequence repeats after the maximal length. For any initial register value, there are $2^{30} - 1 = 1,073,741,823$ random bits before the sequence repeats. For example, for 1000 Hz helicity reversal rate and a quartet pattern, the pattern repeats every 50 days.

During analysis of PV experimental data, the first 30 patterns of each ~one-hour-long data run are used to initialize the shift register (these data patterns are thrown away). After the initialization, the analysis code can predict what the next pseudo-random bit will be. This prediction is compared to the actual helicity of the first window of each pattern to validate the translation was accurate.

7. CEBAF photoinjector

The *photoinjector* (Fig. 7.1 below) represents the first ~ 20 m of the full CEBAF injector [115–118]. The photoinjector supports concurrent multi-hall operation [119–121], providing CW electron pulse trains of differing bunch charge that the full injector delivers to the main CEBAF accelerator with bunch lengths on the order of 1 ps, 10^{-3} energy spread, and 1 nm transverse normalized emittance. The photoinjector main systems are: a load-locked DC high-voltage photogun [122–124], a 4π spin-manipulator system (also known as the 2-Wien spin flipper) [125], several special purpose bunching and accelerating RF cavities [115–117,119], and magnetic beam optics for beam transport. In the following, the photoinjector systems are principally described in beam line order.

Starting at the photogun, the electrons are photoemitted from a single strained-superlattice GaAs/GaAsP photocathode [62] using four circularly-polarized lasers [126], one for each experimental hall, to produce interleaved longitudinally-polarized electron pulse trains. Laser light passes through a vacuum window chosen to have small birefringence and illuminates the photocathode at normal incidence. CEBAF's

fundamental frequency is 1497 MHz, and the lasers operate at independently configurable subharmonics of the fundamental (499 MHz or 249.5 MHz) [119,121]. During routine multi-hall operation, the beam current delivered to the four experiment halls can differ by six orders of magnitude (100 pA to 200 μ A), and the variation in delivered bunch charge can be even larger depending on the bunch repetition rate requested by the experiment, ranging from 2×10^{-19} to 1.3×10^{-12} C. Electron bunches leaving the photocathode possess a temporal profile similar to the laser pulses used to produce them, approximately 35 ps FWHM. The photogun's DC field accelerates the photoelectrons to 130 keV.

The electron pulse trains exit the gun into a baked beamline and then are bent 15 degrees onto the longitudinal axis of the accelerator using an air-core dipole magnet. The next section of the baked beam line is the 4π spin-manipulator system. The spin-manipulator system consists of two Stanford/Mainz-style Wien filters [127] with two intervening single-wound solenoids. The so-called “2-Wien Spin Flipper” is described in detail in Section 9, below.

The baked beam line ends at two circular apertures that originally served to define the beam emittance during CEBAF's 4 GeV era when the injector source was a thermionic gun [119]. Although no longer needed for this purpose, these apertures help to set the beam launch into the chopper system.

The chopper system [119] sets the temporal acceptance of the front-end of the accelerator. The chopper has three parts: a two-cavity RF-deflector system, two counter-wound solenoids, and a set of three independently adjustable temporal apertures known as chopping apertures. The RF-deflector system is a pair of 499 MHz TM_{210} mode rectangular copper cavities [128,129]. Each cavity is driven in two degenerate orthogonal transverse deflecting modes, phased to sweep the beam in a circle with a revolution frequency of 499 MHz. Beam at the center of the first cavity is imaged to the center of the second cavity by the pair of counter-wound solenoid lenses. The solenoids bracket the chopping apertures, located midway between the two deflecting cavities. The amplitudes and phases of the fields in the second deflecting cavity are set to completely remove the RF kick from the first cavity. A fully open chopping aperture can transmit a bunch with maximum duration of 111 ps. Besides providing control of the electron bunch downstream of the chopping system, the chopper slits serve to regulate very low current beam for experiments requiring beam currents on the order of nA and to manage the bleedthrough beam sourced from the higher current beams used for the other experiment halls.

There are two RF-bunching cavities used at the CEBAF photoinjector. Both of these re-entrant-style TM_{010} pillbox copper cavities operate at 1497 MHz and are used to maintain the desired longitudinal bunch length of the non-relativistic beam. The first buncher cavity is known as the prebuncher [116,117] and it is located roughly equidistant between the photocathode and the chopper. The prebuncher is set to zero-crossing. Its purpose is to compensate for space-charge-force induced bunch-length growth over the distance from the gun to the chopper system. Space-charge forces, even for low charge bunches,

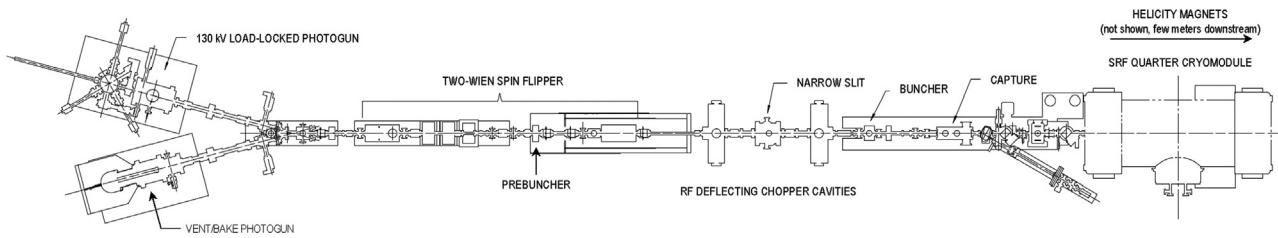


Fig. 7.1. The CEBAF photoinjector. The various beamline elements are described in the text. The helicity magnets (not shown) are located downstream of the quarter cryomodule.

increase the bunch size in space and time [130], and uncompensated, the space-charge forces for the highest bunch charges would grow the bunch length beyond 111 ps, leading to unnecessary beam loss. The second buncher cavity [131], located midway between the center of the chopper system and the following RF cavity known as the “capture”, is the phase reference for the injector and CEBAF accelerator [132]. It is typically phased to zero-crossing or within 20° degrees of zero-crossing to initiate the longitudinal bunch compression.

The capture cavity [115,116,133] is a graded-beta 5-cell side-coupled cavity that accelerates 130 keV beam to ~660 keV and provides additional bunching. It is called a capture cavity because it adds ~500 keV to the beam kinetic energy making it sufficiently relativistic and beta-matched to the two superconducting cavities located downstream.

The two 5-cell superconducting cavities are contained in a cryostat known as the quarter cryomodule [115,116,134]. The original cryomodules for CEBAF contain eight 5-cell Cornell style accelerating cavities and are constructed of 4 subsections each containing one pair of cavities. The quarter cryomodule is so-called because it represents one of these cryomodule subsections [135]. The quarter cryomodule accelerates beam to 6.2 MeV. These cavities are phased off-crest to continue the bunching process started in the second buncher cavity. The bunching process continues with drift bunching in the downstream beam transport line. Beams delivered downstream of the quarter cryomodule can be sent to a Mott polarimeter [43] for polarization measurement, or accelerated to 123 MeV using two full cryomodules.

The beam transport elements between the gun and the quarter cryomodule consist of solenoids distributed along the beam line to focus beam transversely at neighboring downstream elements such as the Wien filters and RF cavities. There are two main categories of solenoids: single-wound and counter-wound. Two single-wound solenoids are located between the gun and the spin-manipulator system, and three counter-wound solenoids, in addition to the two counter-wound solenoids in the chopper system, are between the spin-manipulator system and the quarter cryomodule. The counter-wound solenoids are used after the spin-manipulator system because counter-wound solenoids do not rotate the polarization and spin configuration whereas single-wound solenoids would.

Antenna beam-position monitors are employed along the beamline, to monitor beam position, and to ensure collinearity of the four independent beams. They also provide a means to re-steer the beam to an approved orbit when lasers are moved on the photocathode or when the Wien filter spin angles are adjusted. Refer to Fig. 5.3 for an image of the antenna-style BPM use at the CEBAF photoinjector.

Fig. 7.2 shows the predicted beam energy, beam envelope, energy spread and bunch length along the injector beamline obtained using the particle tracking code GPT [136–138], for simultaneous delivery of low and high current beams with the spin-manipulation system off. Careful adjustment of the RF settings (amplitude and phase) applied to the RF cavities is a critical requirement, as well as optimized solenoid settings that ensure efficient transmission through apertures (more on optics matching in Section 15 below). These simulations demonstrate the flexibility of the CEBAF injector.

8. DC high-voltage photogun

Since the installation of the first polarized-electron source at CEBAF, there have been four major upgrades devoted primarily to improving photogun performance. Each version of the injector supported the successful completion of one or more PV experiments. The first three versions employed “vent/bake” style photoguns and are described in Ref. [123]. As the name implies, “vent/bake” describes the process associated with replacing the photocathode: the photogun must be vented, evacuated and baked to achieve the ultrahigh vacuum condition necessary to sustain long-term beam delivery. This process required approximately four days to complete. To address the unwanted downtime associated with photocathode replacement, two vent/bake style photoguns were installed side-by-side, with the logic being that one photogun would be operational while the other photogun was being serviced. In practice, however, the close proximity of the two photoguns prevented operation of one photogun during vacuum bakeout of the spare photogun: the nearby hot adjoining beam-line resulted in degraded vacuum conditions and poor photocathode lifetime within the operational photogun. To improve photoinjector uptime and to make it possible to evaluate different photocathodes more quickly, the vent/bake photoguns were replaced with a single “load-locked” photogun [124], where the term “load-locked” describes an apparatus composed of multiple vacuum chambers separated by gate valves, with vacuum improving progressively from one chamber to the next (see Fig. 8.1). The CEBAF load-locked photogun employs four vacuum chambers: a portable vacuum “suitcase” used to transport new photocathode samples to the injector, a photocathode loading chamber, a preparation chamber where photocathodes are heated and “activated” with chemicals to reduce the surface work function, and the photogun high-voltage chamber. Each chamber is described briefly below, starting with the high-voltage chamber. The vacuum level inside the photogun high-voltage chamber, especially while delivering electron beam, represents the most important feature of any GaAs-based spin-polarized electron source. The vacuum level sets the photocathode lifetime which is limited by ion bombardment [139], the process whereby residual gas in the high-voltage chamber is ionized by the electron beam. The positive ions created by the electron beam are accelerated toward the photocathode biased at negative high voltage. The ions can sputter away the chemical layer used to create the necessary negative electron affinity condition, or they become implanted producing interstitial defects or vacancies in the crystal structure which reduce the electron diffusion length [140]. In general, for a spin-polarized photogun to exhibit long operational lifetime, the high-voltage chamber must be designed to provide sufficient pumping and manufactured with materials that have a low hydrogen outgassing rate. There must be no field emission from the cathode electrode when biased at the desired operating voltage because field emission will strike the anode or vacuum chamber walls, degrading the vacuum via electron stimulated desorption. And finally, all of the photoemission from the photocathode must be delivered away from the gun, including, for example, the unintentional photoemission produced by low-level illumination of the entire photocathode from scattered ambient light [141]. This unwanted photoemission, particularly from the edge of the photocathode, can

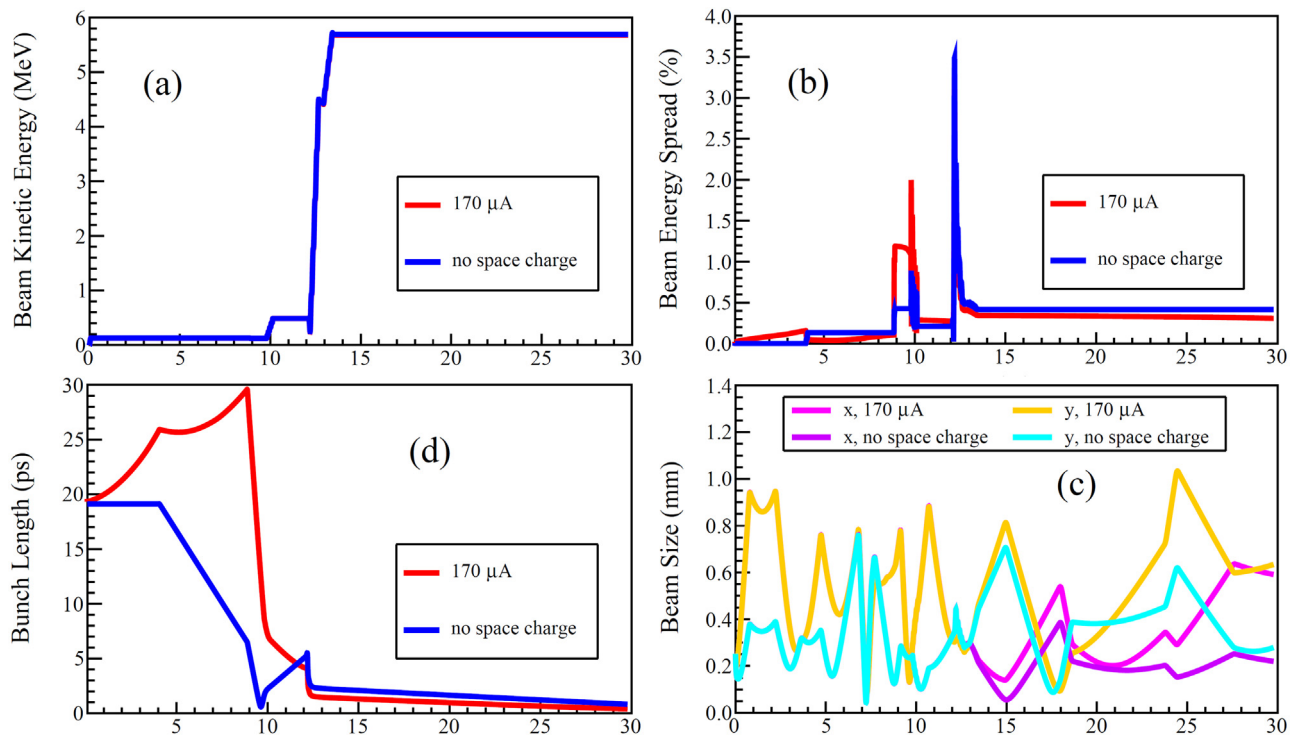


Fig. 7.2. Plots showing the beam characteristics along the length of the CEBAF injector, for high and low current beams (170 μ A and “no space charge”, respectively): (a) beam energy, (b) beam energy spread, (c) beam size, and (d) electron bunch length.

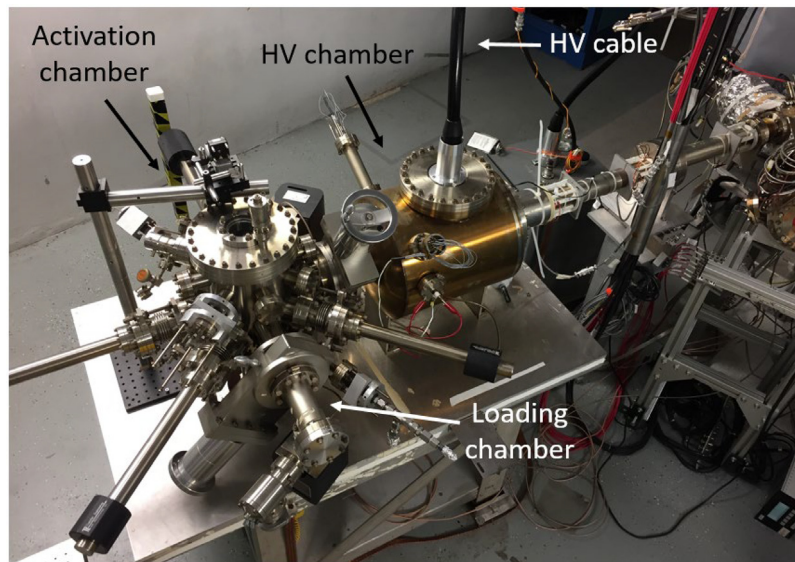


Fig. 8.1. Photograph of the CEBAF DC high-voltage load-locked photogun. The photograph shows three of the four vacuum chambers, separated by valves: loading chamber, activation chamber and high voltage chamber. The “suitcase” vacuum chamber is not shown.

strike the anode electrode or nearby vacuum beamline, degrading vacuum via electron stimulated desorption.

Today’s CEBAF spin-polarized photogun employs a compact, tapered high-voltage insulator (~ 12 cm long) that extends into the vacuum chamber – a so-called inverted-insulator geometry [122] – which offers a number of advantages over photoguns that rely on large cylindrical insulators (see Fig. 8.2). Voltage is applied to the cathode electrode using a commercial high-voltage cable that mates to the insulator. Because there is no exposed high voltage, dry nitrogen gas or SF_6 is not required to suppress corona discharge. And because the insulator also serves as the cathode electrode support structure, there is

considerably less metal biased at high voltage compared to gun designs that require large metal support structures passing through large-bore cylindrical insulators. A smaller cathode structure means there is less metal to polish, and less metal to field emit. Finally, compared to previous versions of the photogun that employed cylindrical insulators with 10” Conflat flanges, the photogun with inverted insulator geometry possesses considerably less surface area, and this provides a considerable vacuum advantage.

During construction, the empty gun high voltage vacuum chamber (35.6 cm dia.) was vacuum degassed at 400 $^{\circ}\text{C}$ for approximately 10 days to reduce the outgassing rate [124,142] and a non-evaporable

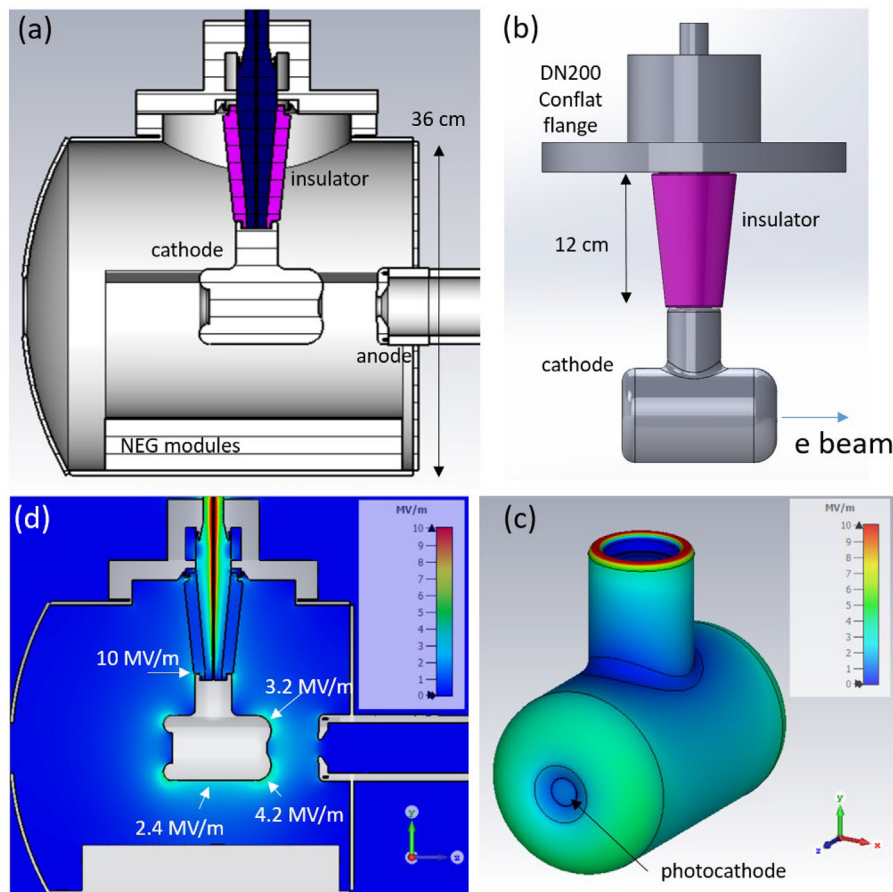


Fig. 8.2. (a) Side view of the CEBAF DC high-voltage photogun with inverted insulator geometry, with essential components labeled, (b) close up view of the tee-shaped stainless steel cathode electrode, (c) the field strength values on the surface of the tee-shaped cathode electrode for 100 kV bias voltage, and (d) an electrostatic field map of the entire photogun.

getter (NEG) thin film coating was applied to the interior surface, similarly to the chambers described in Ref. [143]. Ten commercial NEG modules (SAES WP1250) line the bottom two-thirds of the chamber, with each module oriented to block direct line of sight from the cathode electrode to the vacuum chamber wall. A mesh screen was mounted above the NEG modules and defines the ground plane, minimizing the likelihood that NEG dust could become charged and attracted to the cathode electrode. Most of the internal components were vacuum degassed prior to assembly to minimize outgassing and vented, silver-plated screws were used for internal connections to eliminate trapped gas volume that represent virtual leaks. Internal chamber materials were steel, copper, and Macor or alumina ceramics. Once assembled, the gun chamber was baked in-situ to 250 °C for 36 h to remove water, activate the NEG coating, and partially activate the NEG modules. Additionally, current was applied to the NEG modules near the end of the bakeout to fully activate the modules and maximize pump speed, but electrical shorts in the vacuum feedthrough have prevented full electrical activation. The photogun vacuum chamber also includes a 1 m long beam tube coated with an in-house fabricated NEG thin film. The base pressure in the photogun has been measured to be below 5×10^{-12} Torr using an extractor gauge [143].

The photogun was designed for 100 kV operation, but the bias voltage was increased to 130 kV to improve beam transmission through injector apertures, described below. (A similar photogun with cathode electrode made of large-grain niobium was operated at 200 kV bias voltage [144] at a facility separate from CEBAF.) The main body of the tee-shaped cathode electrode was manufactured from a single piece of vacuum-arc remelt 316LN stainless steel. No welding was performed. A smaller piece – the back face of the electrode – attaches to the main

cathode electrode body with set screws located in a low-field region and serves to capture a spring assembly used to hold photocathode “pucks” inside the hollow electrode structure. The cathode and anode electrodes were polished by hand with silicon-carbide paper and diamond grit of increasingly finer grit. Both the cathode and anode electrodes are shaped to provide focusing. For 100 kV bias voltage, the maximum field strength within the cathode/anode gap is 4.2 MV/m (Fig. 8.2, images c and d). The field strength between the cathode electrode and the NEG pumps and ground screen is only 2.4 MV/m. There is one unintended high field strength region – at the insulator triple point, where metal, insulator and vacuum meet – with field strength 10 MV/m. The anode is located 6 cm from the photocathode and is electrically isolated from ground to permit biasing, as a means to repel ions that originate in the downstream beamline [145,146].

Since the construction of this photogun, a new electrode shape has been developed [147,148] that significantly reduces the field strength at the triple point, which is considered a sensitive area prone to damage. The new electrode will be installed during a scheduled accelerator shutdown and should support reliable operation at 200 kV. It is also worth mentioning that since the construction of this photogun, barrel-polishing has replaced diamond-paste polishing as a means to prepare electrodes for high voltage [149], thereby greatly reducing the time required to put an electrode into service.

The photocathode preparation chamber is dedicated to heating and activating photocathodes, the process whereby a \sim mono-layer of cesium plus oxidant gas (we use NF_3) is applied to the photocathode surface to reduce the surface work function and obtain the necessary negative-electron affinity condition. Only the center portion of the photocathode is activated to negative electron affinity. Restricting the

photocathode active area serves to minimize photoemission from the regions of the photocathode where electrons can travel extreme trajectories that strike the anode or nearby beamline vacuum chamber wall, degrading vacuum and reducing photocathode lifetime [141]. Selective application of cesium is achieved using a mask that rotates in front of the photocathode. Three mask sizes are available: 3, 5 and 7 mm relative to the 12.8 mm diameter of the unmasked photocathode. Ion bombardment and associated QE occurs at the location of the laser beam and along a line to the electrostatic center of the cathode [139, 141]. The QE of the rest of the photocathode remains high while delivering beam. Smaller mask diameters provide the longest operating lifetime but fewer locations to generate beam. In practice, the 5 mm mask provides sufficiently long operating lifetime and approximately four locations to direct the laser beam.

Photocathodes are attached to molybdenum “pucks” using indium solder and a tantalum cup crimped to the side of the puck. The preparation chamber can hold up to four pucks which can be moved from two storage areas, to a heater and into the gun high-voltage chamber using magnetically-coupled sample manipulators. The vacuum within the preparation chamber is typically in the low 10^{-11} Torr range, but increasing to the low 10^{-10} Torr range during photocathode heating and activation. The dominant gas species under all conditions is hydrogen. Prior to activation, photocathodes are heated to 550 °C for one hour to liberate loosely bound adsorbed gas and allowed to cool to room temperature. A yo-yo activation protocol is followed, with typically 10 applications of Cs and NF_3 . Longer heat cycles are employed to restore photocathode quantum efficiency (QE) degraded by long term use from ion bombardment: heating evaporates the surface chemicals, which must be reapplied, but also repairs the damage associated with ion implantation by redistributing the implanted ions over a broad region of the photocathode.

The loading chamber represents the only section of the load-locked photogun that is vented and baked, which happens whenever photocathode samples are removed or installed in the photogun. The loading chamber is relatively small, composed of just a four-way cross with a small ion pump and vacuum window, situated between two all-metal gate valves – one on the preparation chamber and one on the vacuum suitcase used to transport photocathode pucks. Once the suitcase has been attached to the loading chamber, the loading chamber is evacuated and baked at 200 °C for eight hours, then allowed to cool to room temperature. Afterwards, the gate valves on the preparation chamber and suitcase can be opened to move photocathode samples using a long magnetically-coupled sample manipulator attached to the suitcase vacuum chamber which includes a small ion pump. The suitcase chamber weighs approximately 100 lbs. The suitcase is never vented to air. (There is a fifth vacuum chamber, located in a work space away from CEBAF, used to load photocathode pucks into the suitcase).

9. Spin manipulation and the 2-Wien spin flipper

Typically, the experiment halls require spin-polarization oriented longitudinal to the beam propagation direction. Electrons leave the photocathode with spin direction oriented longitudinal to beam motion but spin undergoes precession during passage through dipole magnetic fields within the recirculating arcs and transport lines of the accelerator. The direction of the precession depends on the orientation of the dipole magnet, which may be classified as “in-plane” or “out-of-plane”, where the plane is defined by both linacs. “In-plane” precession occurs if the dipole magnet deflects the beam horizontally and these magnets are found only within the 180° recirculation arcs between linacs and extraction beam lines leading to the experiment halls. At maximum 11 GeV beam energy for polarized beams to Halls A, B and C, the integrated spin precession due to these bending magnets is significant, of the order 21,000 degrees (about 58 revolutions) [150]. In contrast, “out-of-plane” precession occurs if the dipole magnet deflects the beam vertically, and this happens when the elevation of the beamline changes

relative to the linacs. Notably, since all elevation changes in the CEBAF magnet transport system are accomplished using chicanes with zero net bend angle, the “out-of-plane” precession is locally confined and integrates to zero, leaving those sections “spin transparent”.

Consequently, to orient the spin direction properly for an experiment, the injector requires one Wien filter [127,151,152] to rotate the spin direction in the horizontal plane of the accelerator, to counter the “in-plane” precession between the photocathode and the experiment. A Wien filter is a device with static electric (E) and magnetic (B) fields oriented perpendicular to each other and to the velocity (v) of charged particles passing through it (Fig. 9.1). Unit charged particles with velocity $v = E \times B^{-1}$ remain undeflected in passing through the Wien filter, while the spin is rotated in the plane of the electric field. The spin rotation angle, θ_{Wien} , in degrees is given by:

$$\theta_{Wien} = \frac{180}{\pi} \frac{e}{m} \frac{L_{eff}}{\beta c} \left[aB + \left(\frac{1}{\gamma^2 - 1} - a \right) \frac{\beta E}{c} \right] \quad (9.1)$$

where c is the speed of light, e is the electron charge, m is the electron mass, a is the electron anomalous magnetic moment equal to 0.00115965218091, $B = \frac{E}{\beta c}$, β and γ are Lorentz relativistic factors, and L_{eff} is the Wien effective length. At low electron beam energies, most of the spin rotation comes from the electric field. For example, at 200 keV, the rotation due to the magnetic field constitutes only ~0.22% of the total spin rotation. Regardless, the rotations from both fields add, with the rotation occurring in the plane defined by the beam trajectory and the electric field.

A “horizontal” Wien filter has been used at CEBAF [123] since the late 1990’s to orient the spin direction of the beam at the injector by an amount equal but opposite to the spin precession (modulo π) introduced as the beam passes through the arcs and transport lines to the halls. This sets the spin direction longitudinal to the direction of beam motion at the target. The CEBAF Wien filter is similar to the design from SLAC and can provide $\pm 90^\circ$ rotation at beam energies up to ~140 keV. Recently, CEBAF Wien filters were upgraded to provide similar spin rotation for 200 keV beam and one Wien filter was tested successfully for 300 keV beam, which is challenging because the electric field strength required is large (> 5 MV/m) and must be uniformly created by electrodes ~40 cm long [153]. Despite the Wien filter’s effective functionality as a spin-rotator, the magnetic and electric fringe fields [154] tend to degrade the electron beam emittance and energy spread, particularly when spin-rotation angles exceed ~45° degrees. For large spin rotations, quadrupole lenses and bunching cavities are used to manage the longitudinal and transverse beam size.

For parity violation experiments, a second Wien filter was added to the baked beamline, but oriented to rotate spin out of plane, referred to as the “vertical” Wien filter. The motivation for building the 2-Wien Spin Flipper [125] was to provide a “slow” polarization flip – or helicity reversal – at the experiment target. So-called “slow” helicity reversals are important to identify and suppress systematic false asymmetries that can mimic the interesting physics asymmetry being measured [80]. On a daily basis, the helicity of the electron beam is reversed using an insertable-halfwave plate (IHWP) located on the drive laser table, placed immediately upstream of the Pockels cell used to generate circularly-polarized light (see Section 11). The IHWP provides an excellent method for canceling false asymmetries originating from electronics pickup of the helicity signal, however false asymmetries related to the laser polarization do not cancel. The 2-Wien spin flipper provides another means to implement a helicity flip, but in a manner that directly changes the spin direction of the electron beam. The device can be used to orient the spin in any direction [125], a feature that has proven useful for transverse asymmetry measurements [155–160, see for example references].

Besides the Wien filters, solenoid magnets are key elements of the 2-Wien spin flipper. A solenoid magnet provides effective focusing of a low momentum (0.1 – 1 MeV/c) electron beam, where the focal length is inversely proportional to the integral of the square of the magnetic

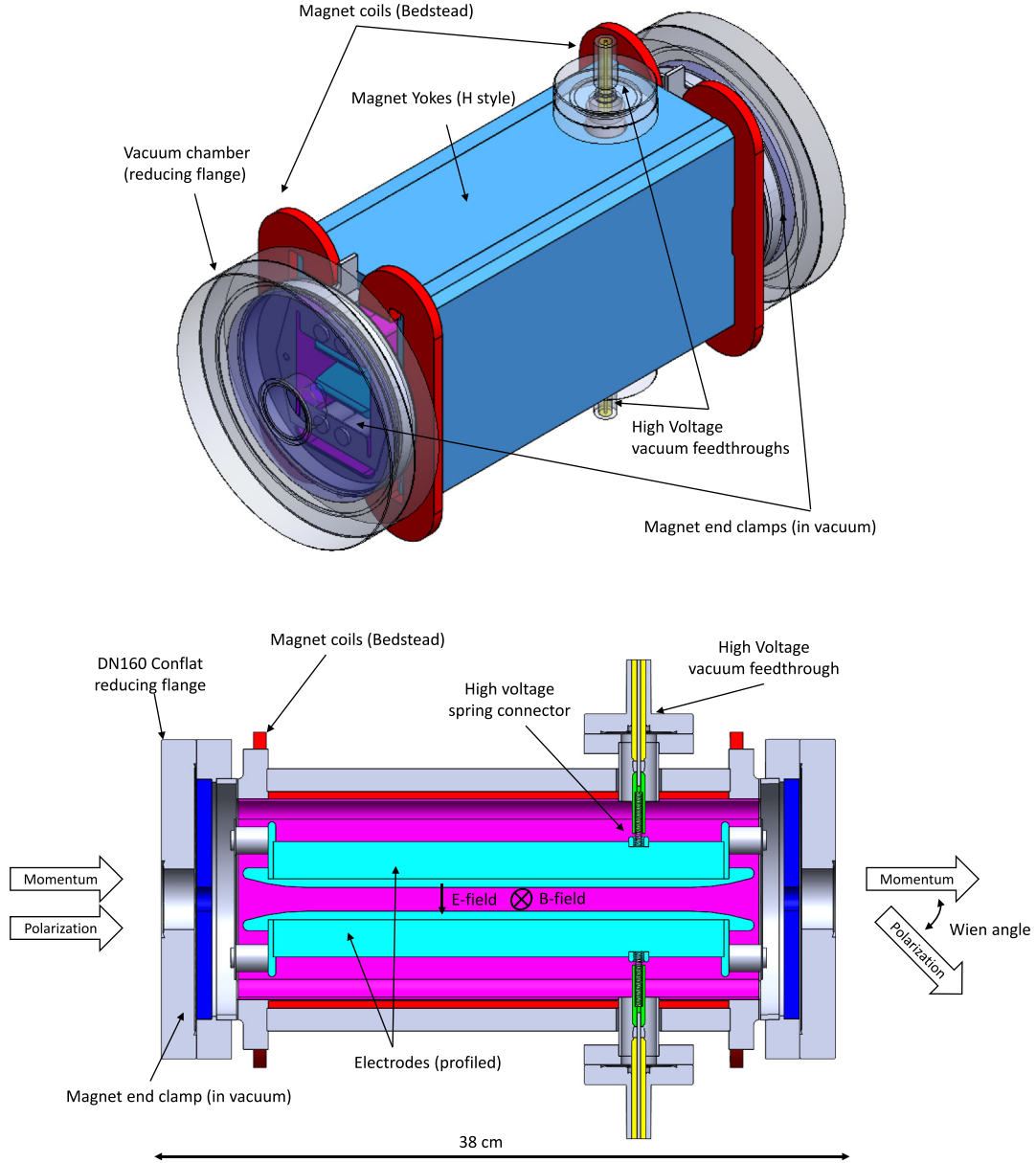


Fig. 9.1. Diagram of a CEBAF Wien filter, based on a SLAC design, and used worldwide. (top) external features, and (bottom) internal features.

field, given in the paraxial approximation by $1/f \propto \int B_z^2 dz$ [161]. Importantly for the spin-flipper, solenoids rotate the spin of a low energy electron beam by an amount proportional to $\int B_z dz$ with spin rotated about the longitudinal magnetic field. It is necessary to use two solenoids in series to simultaneously set both a desired optical focusing and spin rotation. The solenoid spin rotation angle, θ_{sol} , in degrees can be written as:

$$\theta_{sol} = \frac{180}{\pi} \frac{e}{m} \frac{L_{eff}}{\beta c} \left[\frac{1}{\gamma} (a + 1) B_z \right] \quad (9.2)$$

where here, L_{eff} is the solenoid magnetic field effective length. Other symbols were defined for Eq. (9.1).

A “slow” helicity reversal has been approached two ways. In one approach (Fig. 9.2, top), the vertical Wien filter rotates the spin direction 90° into the vertical plane. The intervening solenoids then rotate the polarization back to the horizontal plane, but with spin oriented transverse to the beam propagation direction. Then, by simply changing the direction of the current through each solenoid, the spin direction can be flipped by 180° , while the solenoidal focusing remains

unchanged. Finally, the horizontal Wien filter is used to compensate the spin precession of the accelerator.

The main advantage of this method is that the Wien filter settings, which can have a profound effect on the injector optics (see above), are not changed to enact a spin flip. Only the direction of the current through the solenoid magnets is changed. However, while appealing for its simplicity, this method incurs a correlated *coupled* phase space rotation of the helicity-correlated position and angle differences between slow reversals due to the coupled solenoid magnet fields. As a result, there is imperfect cancellation of the helicity-correlated systematic variations in beam properties that the 2-Wien spin flipper was designed to address.

A second approach was used for the PREx2 [25] and CREx [26] experiments (see Fig. 9.2, bottom). The slow spin flip was achieved by flipping the spin direction using the vertical Wien, set to rotate polarization out of plane $\pm 90^\circ$, and leaving the solenoid currents unchanged. This method provides the desired cancellation of helicity-correlated systematic variations in beam properties, but incurs accelerator downtime to regain acceptable beam optics that provide good injector transmission through apertures. In practice, it takes about 8 h to provide

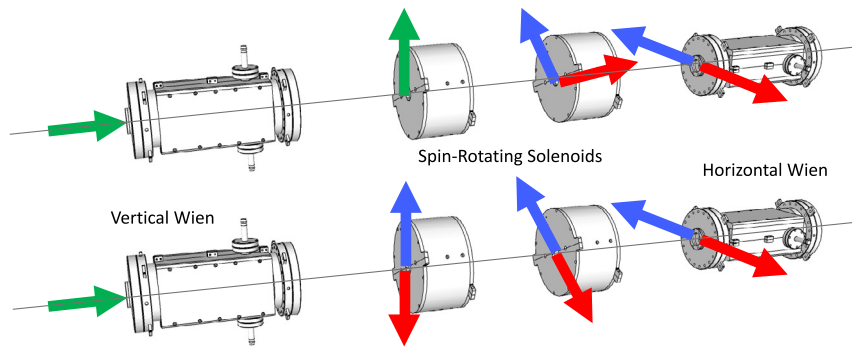


Fig. 9.2. Schematic of the 2-Wien spin flipper composed of vertical Wien filter, spin rotating solenoids, and horizontal Wien filter. Beam travels left to right, with large arrows depicting beam polarization direction. The “spin flip” – polarized beams with spin direction oriented in the horizontal plane but pointing in opposite directions – are created either by reversing the polarities of the two solenoid currents (top) or the Wien filter dipole current and electrode high voltage polarities (bottom). In both cases, the horizontal Wien filter is used to orient the spin direction longitudinal at the experiment hall.

this type of “slow” helicity reversal, with time devoted to steering adjustments to regain the injector beam orbit and to confirm the parity quality beam requirements.

10. Apertures and helicity-correlated beam asymmetries

An important consideration for PV experiments is clean, loss-free transmission of electron beam through apertures. Aperture clipping couples different types of helicity-correlated beam asymmetries: it can transform position differences into charge asymmetries and spot-size asymmetries into position differences, which complicates the feedback corrections necessary to keep helicity-correlated beam asymmetries acceptably small.

Analytical calculations [91] suggest that charge asymmetry variations > 50 ppm can be created by $1 \mu\text{m}$ helicity-correlated position differences, and assuming 5% aperture loss. Aperture losses of 2–5% are typical at the CEBAF injector. Furthermore, helicity-correlated position differences > 70 nm can be created by moderate 2×10^{-4} helicity-correlated spot-size asymmetries, for 1 mm beam spot-size and $\sim 5\%$ aperture loss.

In addition, because there is always some natural beam motion or “jitter”, beam interception at apertures results in transmission fluctuations that increase the distribution widths of the measured helicity-correlated asymmetries, thereby reducing the accuracy of these measurements. Ammeters attached to electrically-isolated apertures can help pinpoint egregious beam loss. On a finer scale relevant to PV experiments, measurements of charge asymmetry A_Q using BPMs along the beamline can alert experimenters and Accelerator Operations staff to beam clipping/losses at unexpected locations, as shown in Fig. 10.1. [91]. In Fig. 10.1, notice how the charge-asymmetry distribution width increases sharply between BPMs 1104 and 1106, corresponding to the vicinity of the Vertical Wien filter and prebuncher. Both of these devices have aperture less than the 1.5” diameter of the beam pipe, and can be the source of clipping that is not always obvious because these elements are electrically grounded. By adjusting the trajectory of the beam through these devices, the width of the distribution of measured helicity-correlated charge-asymmetry could be made small and relatively constant.

During the G0 forward angle experiment [11], the requested beam current was modest, only $40 \mu\text{A}$. But to facilitate time-of-flight detection, the pulse-repetition rate was reduced to just 31.875 MHz (the 48th subharmonic of the 1497 MHz accelerating frequency), which resulted in very high bunch charge by CEBAF standards. And during the Qweak experiment [21–24], the requested beam current was $180 \mu\text{A}$ which is roughly a factor of two greater than typical high current experiments at CEBAF. Achieving clean, loss-free beam transport was very challenging for these experiments.

At the nominal CEBAF gun voltage of 100 kV [123], the beamloss at injector apertures during both of these experiments was significant

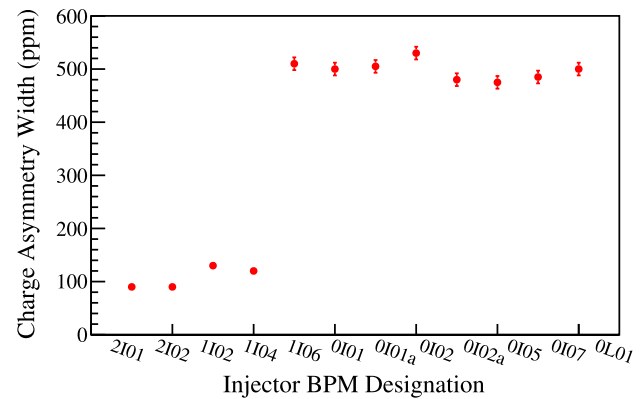


Fig. 10.1. The width of the distribution of measured helicity-correlated charge-asymmetry A_Q using BPMs along the injector beamline. BPMs are listed in sequential order, beam moving left to right from the photogun to the quarter cryomodule. The sharp change in the measured distribution width at BPM 1106 indicates beamloss originating upstream, in the vicinity of the Vertical Wien filter and prebuncher.

($> 30\%$). The beamloss stemmed from space-charge-induced emittance growth and could only be reduced by operating the photogun at higher bias voltage. To illustrate the impact of space charge forces, transmission measurements were made versus beam current for different gun-bias voltages, and with the prebuncher cavity de-energized (Fig. 10.2). The figure illustrates the benefit of higher photogun bias voltage: with the photogun bias voltage set to 130 kV, and with the prebuncher energized, injector transmission during the Qweak experiment was $\sim 90\%$ (i.e., acceptable). To support the MOLLER PV experiment [27], the photogun voltage will be increased to 200 kV, which should provide even better transmission through apertures.

11. Drive lasers and the laser table

There are four nominally identical photogun drive lasers – one for each experiment hall – that produce RF-pulsed light with ~ 35 ps optical pulsewidth (FWHM). The laser beams are combined as described below, with interleaved pulse trains at 248.5 or 499 MHz, and illuminate the same location on the photocathode. The CEBAF drive lasers are fiber-based systems [126] and consist of three main components as illustrated in Fig. 11.1: a gain-switched fiber-coupled diode seed laser at 1560 nm, two ErYb-doped fiber amplifiers used to obtain sufficient optical power, and a periodically-poled lithium niobate (PPLN) frequency-doubler used to produce light at 780 nm required to generate highly polarized beam from the strained-superlattice GaAs/GaAsP photocathode [62]. The term “second-harmonic generation” is synonymous with laser “frequency doubling” [162,163] and describes the non-linear

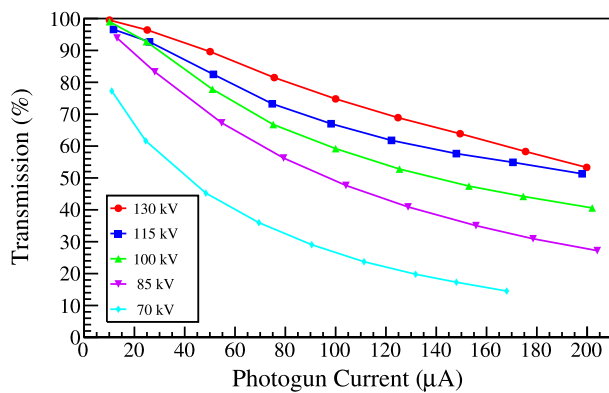


Fig. 10.2. Transmission through photoinjector apertures versus photogun beam current and for different photogun bias voltages. Significantly improved transmission was obtained at 130 kV compared to nominal 100 kV. Note, the RF prebuncher was de-energized during these measurements. With prebuncher energized, transmission reached ~90% with 200 μ A delivered to Hall C.

optical process of converting light at one wavelength to another, in this case from 1560 nm to 780 nm.

Gain-switching is a purely electrical technique [164] with the diode laser biased near threshold and driven with ~ 1 W of RF energy through a bias-network. The optical pulse-repetition rate is equal to the RF drive frequency. For pulse repetition rates > 100 MHz, it is sufficient to simply apply an RF sine wave to the diode via the bias network. At lower repetition rates, it can be advantageous to use a step-recovery diode to create short electrical pulses which are then applied to the diode laser. In contrast to modelocked lasers, no laser cavity-length feedback is required: the optical-pulse train from a gain-switched system stays locked to the accelerator RF reference with timing jitter < 1 ps which ensures highly reliable beam delivery [165].

The CEBAF drive lasers are distributed systems, with low-power components (gain-switched diode laser and Er/Yb fiber preamplifier) located outside the accelerator enclosure and high power components (Er/Yb fiber amplifier and PPLN frequency doubler) located inside a class 100 laser clean room positioned near the photogun and adjacent to the injector beamline. Light is delivered from low-power components to high power components using a polarization-maintaining single-mode optical fiber approximately 25 m long. At the laser wavelength 1560 nm, there are no mirrors to clean or align. Standard fiber-optic components labeled ISO in Fig. 11.1 provide optical isolation between components, to protect sensitive elements from damage. Elements labeled WDM (for wavelength division multiplexing) are also standard fiber optic components and provide a means to optically pump the Er/Yb gain elements within each fiber amplifier. The Er/Yb fiber preamplifier is homemade and the Er/Yb fiber power amplifier is a commercial unit.

Most elements of the CEBAF drive laser system reside on a 4' x 6' bread-board style laser table (Fig. 11.2) located inside a class 100 clean room with interlocked access for laser safety, and with conditioned air to maintain constant temperature and to control humidity. The laser clean room is positioned adjacent to the injector beamline approximately 2 m from the photogun. Because the injector cannot be occupied during beam operations, some of the optical elements are remotely controlled.

After frequency doubling via temperature-controlled phase matching using the PPLN crystal, a dichroic mirror reflects the useful light at 760 nm toward the photocathode and passes residual 1560 nm light, as well as visible light produced within the fiber amplifier via non-linear optical processes, to a laser beam “dump”. Optical elements are described below in roughly sequential order, as the light travels to the photocathode.

The laser settings, including those related to the fiber-power amplifier, are maintained constant. To vary the laser power delivered to the photocathode, the light from each drive laser passes through a stepper-motor controlled “attenuator” composed of a rotating-halfwave plate and fixed downstream linear polarizer.

To combine the four laser beams onto a common path directed at the photocathode, partially-reflective mirrors and a polarization-sensitive optical element are used (See Fig. 11.1). Each drive laser emits linearly-polarized light. For Halls A and B, the linear polarization of the respective drive lasers is oriented *horizontal*, with the two laser beams combined using a partially-reflective mirror that preserves 70% of the light for Hall A and 30% of the light for Hall B. For Halls C and D, the drive laser linear polarization is oriented *vertical*, with light combined using a partially-reflective mirror in a similar manner. Afterwards, the two pairs of laser beams are combined and directed onto a common path using a polarization-sensitive optic called a polarization beam-combining cube. The beam combining ratios set by the partially-reflective mirrors were chosen to meet the beam current requirements of the Halls, with Halls A and C operating at much higher current compared to Halls B and D.

A small percentage of the combined light delivered to the photocathode exits an adjacent port of the beamsplitter cube, and this “pick off” light is delivered to a CCD camera which serves as a virtual photocathode, i.e., the CCD camera is located the same distance from the beamsplitter cube as the photocathode. Some of the transport mirrors on the laser table can be remotely controlled using piezo-controlled motors, to fine tune the position of each laser beam at the CCD camera, and hence, the same position on the photocathode. In addition, there is a Spiricon CCD camera laser beam imaging system – employed when a remotely controlled mirror located near the beamline vacuum window is inserted into the laser beam path – which can be used to make the four laser beams coincident at the photocathode but also to accurately measure/set laser beam sizes.

The collimated light from each laser, combined as described above, is then directed through the Pockels cell, to convert linearly-polarized light into circularly-polarized light. It is worth mentioning that although pairs of laser beams are linearly polarized in orthogonal directions, the Pockels cell still generates circularly-polarized light for all four beams. Two laser beams are polarized right-circular, and the other two laser beams are polarized left-circular, for the same Pockels cell settings.

The last optical element is a focusing lens located immediately in front of the beamline vacuum window. Originally, the focal length of this lens was chosen to produce a tight beam waist at the photocathode, however, this enhanced beam blowup associated with space-charge forces and resulted in poor transmission through injector apertures. Moreover, significantly longer photocathode operating lifetime was achieved using larger laser beam size at the photocathode [141]. A large laser beam produces the same number of ions within the photogun cathode/anode gap (more below), but with the ion damage distributed over a larger area, such that QE decay at any specific photocathode location happens more slowly. To increase the size of the laser spot of the photocathode, it was a simple matter of changing the focal length of the lens. The distance between the focusing lens and the photocathode is approximately 2 m. Whereas originally, a 2 m focal length lens was chosen to produce ~ 0.3 mm (FWHM) laser spots at the photocathode, now a 1.5 m focal length lens generates a beam waist in front of the photocathode, with the laser beam expanding enroute to the photocathode to produce ~ 0.5 mm (FWHM) laser spots.

The focusing lens is attached to an X/Y stepper-motor stage to permit remote positioning of the laser light anywhere on the photocathode within the 5 mm active area. The moveable focusing lens also provides a means to assess the photocathode lifetime in the form of a “QE scan”: Fig. 11.3 shows the evolution of photocathode QE after delivering polarized electron beam from three different photocathode locations. As referenced above, QE reduction is caused by ion back-bombardment

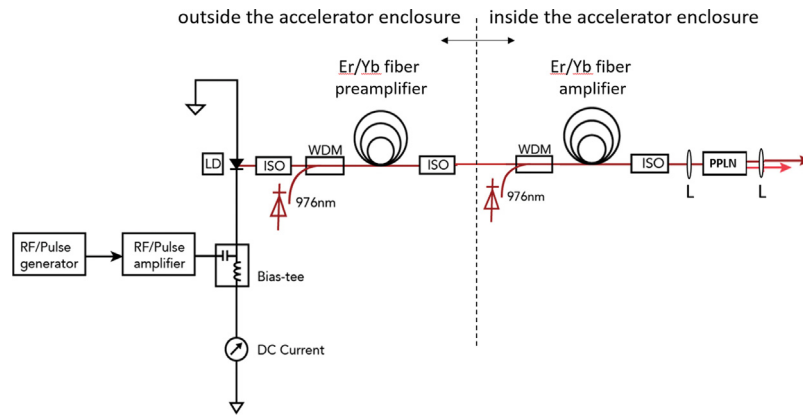


Fig. 11.1. Schematic representation of a typical CEBAF drive laser composed of a gain-switched diode seed laser, two fiber amplifiers to boost power, and a PPLN crystal to convert 1560 nm light to 780 nm light required for generating polarized electrons. LD, laser diode; ISO, optical isolator; WDM, stands for wavelength-division multiplexing and represents an optical fiber component used to combine light of different wavelengths; PPLN, periodically poled lithium niobate.

of the photocathode [139], the process whereby electrons extracted from the photocathode ionize the residual gas within the photogun HV chamber and adjoining beamline. These positively charged ions are then attracted to the negatively biased photocathode. The ions can sputter away the chemicals applied to the photocathode surface necessary to create the negative-electron affinity condition needed for photoemission, or they implant within the photocathode and reduce the electron diffusion length. The ion damage associated with beam production is very localized, limited to the location of the laser spot (where ions produced by the electron beam have low energy) and along a “trench” directed to the electrostatic center of the photocathode (where the highest energy ions are delivered) [141]. As a result, a single photocathode activation can provide months of beam delivery from up to four different locations on the photocathode, depending on the size of the laser beam. For more information on ion back-bombardment and the various means employed at CEBAF to prolong the photocathode operating lifetime, see ref [140].

The remaining optical elements are key for PV experiments. An insertable-halfwave plate (IHWP) located immediately upstream of the Pockels cell can be inserted to provide a 180° helicity spin flip of the electron beam. Ideally, this would only change the sign of the measured physics asymmetry, but not the absolute magnitude. Importantly, this procedure would, for example, help to identify ground loops corrupting the experiment’s data stream. The IHWP rotates the linear polarization of the incoming laser beams by 90° , which means the Pockels cell creates left-circularly polarized light instead of right-circularly polarized light, or vice versa.

Another halfwave plate – attached to a rotating stepper motor stage – is positioned downstream of the Pockels cell. The so-called rotating-halfwave plate (RHWP) is used to rotate the direction of any residual linear polarization (intended or unintended), to counter the effects of residual birefringence of the beamline vacuum window through which the laser beam pass enroute to the photocathode.

Finally, within each laser beam path, there is an optical element referred to as the “IA”, which is an abbreviation for laser *Intensity Asymmetry correction device*. It is used to vary the laser power in each helicity state, to zero the helicity-correlated charge asymmetry present in beams delivered to neighboring halls. Note, the main Pockels cell is used to zero the helicity-correlated charge asymmetry of the beam delivered to the PV experiment hall. But in the process of zeroing the helicity-correlated charge asymmetry at the PV hall, large charge asymmetries can be created on the beams to neighboring halls, and this is unacceptable for those halls measuring scattering asymmetries. An IA consists of halfwave plate, a Pockels cell, and a fixed linear polarizer. The upstream halfwave plate rotates the orientation of the linearly-polarized laser light relative to the downstream fixed linear polarizer, and the intervening Pockels cell is used to counter the polarization

rotation of the half waveplate, but in a helicity-correlated manner, providing more or less light in each helicity state, to provide equal beam currents in each helicity state. The Pockels cell within each IA is made of KD*P but unlike cells used to provide circularly polarized light, it is driven with comparatively low voltage, 90 V. Under typical operating conditions, an IA can vary the amount of laser light in each helicity state by a few percent. The upstream halfwave plate can be rotated (remotely) to vary the extent of this modulation, providing more or less variation in transmitted laser power (i.e., to provide more/less sensitivity to applied IA Pockels cell voltage).

Tune-Mode Generator

The physics experiments conducted at each hall are performed with continuous wave (CW) beam [166], with electron bunches arriving at RF repetition rates of 249.5 MHz or 499 MHz and providing the highest possible duty factor at each experiment hall. However, CW beam is too powerful for machine tune-up, which happens at the start of each run period, with magnet and RF settings adjusted to optimize beam delivery. During machine tune-up, it is not uncommon to “lose” beam, with mis-steered beam striking the beamline vacuum chamber walls. To perform machine tune-up safely, so-called “tune-mode generators” are used to produce beams with low duty factor – enough beam to trigger diagnostics needed for spin-up, but at beam power levels that will not damage accelerator components or burn-through the beamline vacuum chamber. Tune mode generators can also produce a specific “macropulse” time structure needed to precisely set the pathlength of the accelerator, which is very important for multi-pass operation of the linacs.

There is a tune-mode generator [167,168] for each hall composed of a Pockels cell made of RTP (rubidium titanyl phosphate) [169,170] situated between fixed linear polarizers oriented to pass light with the Pockels cell high voltage OFF, and a halfwave plate oriented to rotate the input linear polarization 90 degrees when inserted (Fig. 11.4). The material RTP was chosen for its fast response time (more on this topic in Section 13). When low duty-factor beam is requested for machine tune-up, the halfwave plate is inserted and voltage is applied to the Pockels cell for a relatively short duration. For the time period when high voltage is applied to the tune-mode-generator Pockels cell, light can pass through the downstream fixed linear polarizer, and electron beam at low duty factor is produced. Table 11.1 lists the standard parameters for tune-mode generator operation. Because of the fast time response of RTP, the tune mode generators can quickly turn OFF the electron beam. For this reason, the tune mode generators also serve as important “accelerator credited control” devices for personnel safety [171]. The tune mode generator also includes a mechanical shutter to completely extinguish low level light that might pass through the downstream fixed linear polarizer due to optical element imperfections and misalignment.

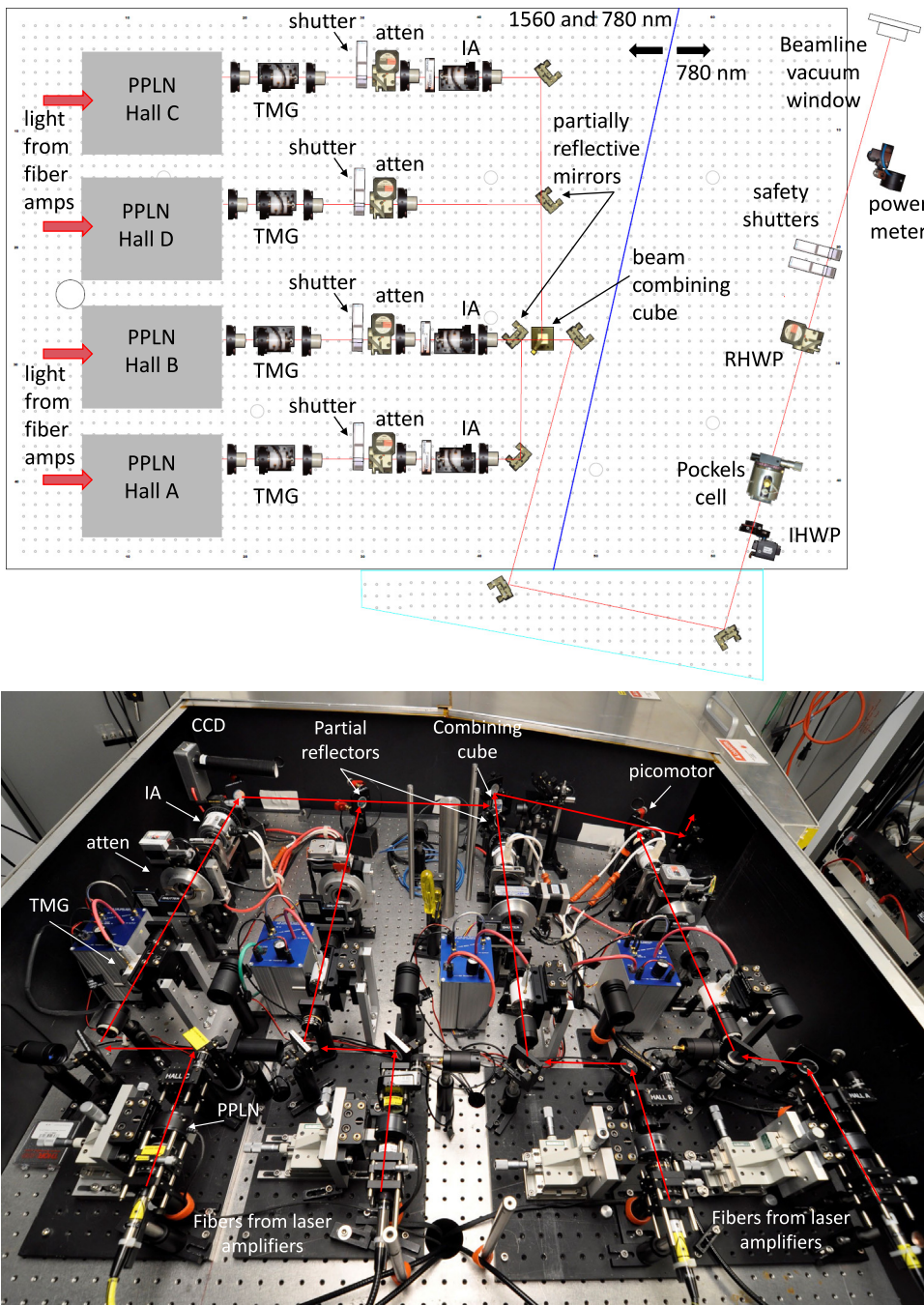


Fig. 11.2. (top) Schematic representation of the CEBAF photoinjector laser table, with the elements labeled and described in the text, (bottom) a photograph of the laser table.

Table 11.1
Tune-mode generator modes of operation.

Beam mode	Macropulse duration at 60 Hz	Duty factor	Tune mode generator Pockels cell	Tune mode generator halfwave plate	Shutter
OFF	N/A	0	ON	IN	CLOSED
Viewer limited	4–10 μ s	0.02–0.06%	ON	IN	OPEN
Tune mode	250 μ s ON, 100 μ s OFF, 4 μ s ON	1.52%	ON	IN	OPEN
CW	N/A	100%	OFF	OUT	OPEN

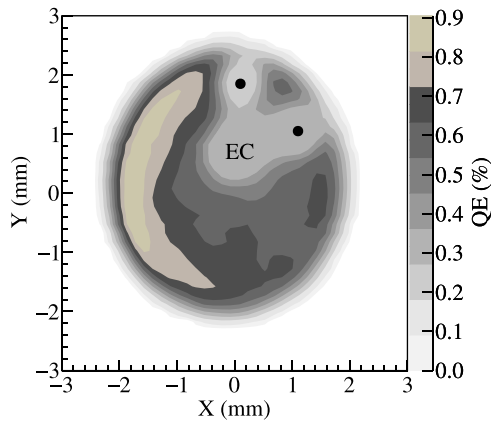


Fig. 11.3. Photocathode “QE scan” showing the evolution of QE following beam extraction from three different photocathode locations. Photocathode QE decays at the location of the laser beam and along a “trench” directed to the electrostatic center (EC) of the photocathode.

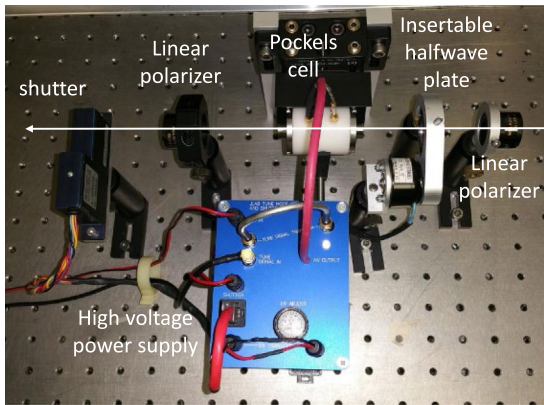


Fig. 11.4. Photo of a tune-mode generator.

12. Pockels cell alignment, slow reversals, and feedback loops – or, “Doing the Experiment”

As mentioned above, when performing a PV experiment, unwanted helicity-correlated beam asymmetries must be maintained such that their contribution to the measured raw (detector) asymmetry is much smaller than the physics asymmetry being measured. And as discussed in Section 4, helicity-correlated beam asymmetries originate at the CEBAF photoinjector, stemming from photocathode QE anisotropy, residual linear polarization of the drive laser light, Pockels cell imperfections or alignment errors, and vacuum window birefringence. While experimenters are not wholly averse to using feedback loops to minimize helicity-correlated beam asymmetries, they prefer to use as little feedback as possible because sometimes feedback to address one helicity-correlated beam asymmetry can impact another. From a practical point of view, only helicity-correlated charge asymmetry, is “easy” to measure and relatively straightforward to control with feedback (described below). Position differences are harder to measure at the experiment hall and not as easy to control using components on the drive laser table (see helicity magnets, Section 14 below). Spot size asymmetries cannot presently be measured in the beamline and there is no mechanism to apply feedback (at least with KD*P Pockel cells), so only careful alignment of the Pockels cell provides a straightforward path to minimizing helicity-correlated beam spot size asymmetries.

Before describing Pockels cell alignment procedures, helicity “slow reversals” must be described. To further suppress uncontrolled systematic effects associated with the fast helicity reversal of the Pockels

cell, the experimenters perform “slow” reversals of the spin direction (“infrequent” is a more accurate description, but “slow” reversal is the widely used terminology). A slow reversal is when the electron-beam helicity is reversed relative to both the electronic helicity-control signals and the voltage applied to the Pockels cell. Slow reversals are used to help cancel systematic errors. There is an insertable halfwave plate (IHWP, see Section 11) upstream of the Pockels cell used to rotate the polarization of the incoming linearly polarized laser light by 90° which in turn flips the helicity of the resultant circularly polarized light, from right to left, which in turn flips the direction of the electron beam polarization. This flip is introduced approximately once per day. In addition, there is the 2-Wien spin flipper described above, which provides the same desired effect but by manipulating the electron beam itself and not the drive laser light. The Wien flip provides a second cancellation method to further suppress systematics including position differences, spot size asymmetries and, depending on how the Wien flip is performed, transverse polarization components.

A more detailed description of the Pockels cell alignment procedure is presented below (compared to what was presented in Section 4). For more information on the nature of these adjustments, please see many excellent Refs. [80–83,91]. The procedure also describes steps to align the insertable-halfwave plate (IHWP) used for slow helicity reversals, and a remotely controlled rotatable-halfwave plate (RHWP) used to align the axis of residual linear polarization relative to the strain-axis of the photocathode.

The alignment procedure references Stokes parameters (S_0 , S_1 , S_2 and S_3) which are commonly used to describe the polarization of laser light [172,173]: S_0 describes the degree of polarization, S_1 the DoLP along horizontal/vertical axes, S_2 describes the DoLP along $\pm 45^\circ$ diagonal axes, and S_3 describes the DoCP. The alignment procedure references only S_1 and S_2 , which is sufficient. This is because the laser light is not unpolarized, such that $S_0 = 1$, thereby making S_3 redundant with S_1 and S_2 measurements.

The term PITA is frequently used in references cited above. Originally it stood for “polarization induced transport asymmetry”, which describes the variations in beam current observed between two helicity states stemming from differences in reflectivity for “s” and “p” polarized light at laser transport mirrors (i.e., circularly-polarized light became elliptically polarized upon reflection from laser transport mirrors, providing different laser powers in the two helicity states). Today however, PITA means something different, namely it stands for “phase induced transport anomaly” and rather than describing an unintended consequence, it describes the process of adjusting Pockels cell voltages to minimize helicity-correlated charge asymmetry.

In the CEBAF tunnel enclosure, Pockels cell alignment procedure [91]

- Set the laser beam size and divergence at the Pockels cell by adjusting the position of the collimating lens near the PPLN frequency doubling crystal. Laser beam size should be ~ 1 mm (2 sigma) and divergence < 1 mrad. (This adjustment impacts the laser spot size at the photocathode. The laser beam size at the photocathode should be 0.5 mm (4 sigma), but not smaller because photocathode QE degrades more quickly with small laser beams [141])
- Using a handheld infrared viewer, center the Pockels cell aperture on the laser beam using a piece of cellophane tape or lens cleaning tissue placed in front of the cell, to disperse a portion of the light while still providing a clear image of the primary transmitted beam.
- Using the handheld infrared viewer, look for back reflections of light from the Pockels cell crystal faces, align the Pockels cell pitch and yaw so that the back reflections overlap the incoming beam as closely as possible.
- Coarse adjustment of Pockels cell: Insert a laser-power meter or photodiode into the laser path downstream of the Pockels cell. Now install a spinning linear polarizer between the Pockels cell

and laser-power meter, and note the sinusoidal-modulated laser power on the oscilloscope. Adjust Pockels cell voltages, pitch, roll and yaw to maximize the degree of circular polarization (DoCP) and minimize the degree of linear polarization (DoLP). For both helicity states, DoLP should be 5% or less (calculate DoLP and DoCP using Eqs. (4.1) and (4.2)).

- Coarse alignment of the insertable half waveplate (IHWP): Insert the IHWP – used to provide a slow helicity reversal – and adjust its angular orientation to obtain the highest possible degree of circular polarization (DoCP).
- Iteratively refine the alignment of both elements, the Pockels cell and IHWP, adjusting the Pockels cell voltages, pitch, roll and yaw.
- Once 99.9% circular polarization is achieved for both IHWP-out and IHWP-in configurations, verify the DoLP for the other three CEBAF lasers at the same Pockels cell voltage settings already obtained. The DoCP for all lasers should be 99.9%. If not, make the laser beams more collinear at the cell.
- Now with more precision, using a dedicated DAQ and a fixed Glan-Taylor linear polarizer aligned to pass light in the horizontal and then vertical plane (i.e., the so-called Stokes parameter S_1), minimize the laser-power asymmetry in the two helicity states by adjusting Pockels cell voltages.
- Next, rotate the Glan-Taylor linear polarizer $\pm 45^\circ$ relative to horizontal/vertical planes and minimize the laser power asymmetry in the two helicity states by adjusting the Pockels cell pitch and yaw angles for KD*P cells. For RTP cells, adjust the Pockels cell roll.
- Use a quadrant photodiode to measure/minimize steering effects:
 - With no analyzer in place (i.e., the downstream linear polarizer removed), measure steering effects using a quadrant photodiode located downstream of the Pockels cell: for the KD*P Pockels cell, translate the cell in X and Y, for the RTP cell, adjust voltage settings.
 - Attempt to reduce the birefringence gradient effects in S_1 , the analyzing-like position differences, using the Pockels cell pitch and yaw angle (true for both styles of Pockels cell, KD*P and RTP).
- Measure helicity-correlated spot-size asymmetries with a linear-photodiode array, by orienting the photodiode array in various directions: horizontal, vertical, and $\pm 45^\circ$. All of these configurations must be evaluated to assign an upper bound to the helicity-correlated spot-size asymmetry. For KD*P Pockels cell, slight angular adjustments may reduce spot-size asymmetries. For RTP Pockels cell, slight translational adjustments may reduce spot size asymmetries.
- With the photocathode biased at low voltage (~ 100 V), apply laser light to extract ~ 1 uA of electron beam, and measure the analyzing power of the photocathode which is typically 3–7%. Specifically, turn OFF the Pockels cell to illuminate the photocathode with linearly polarized light, and measure the photocurrent while rotating the orientation of the linearly polarized light through 360° using the RHWP to record maximum/minimum QE values.

Each step of the alignment procedure described above addresses progressively higher moments of beam setup: electron-beam polarization, helicity-correlated charge asymmetry (0th moment), helicity-correlated position/angle differences (1st moment), and helicity-correlated spot-size asymmetry (2nd moment). The helicity-correlated charge asymmetry and position/angle differences will be evaluated by monitoring the electron beam directly, and feedback loops are used to minimize these values (described below). Helicity-correlated spot size asymmetries however, can only be measured and bounded on the laser table.

The procedure now shifts from hands-on laser table work to electron beam-based measurements, with adjustments to Pockels cell and RHWP made remotely.

Fine tuning of the alignment of the Pockels cell and RHWP using the electron beam

- With the photocathode biased at high voltage, deliver electron beam to the first Faraday Cup of the baked beamline, approximately 5 m from the photogun. Measure helicity-correlated charge and position asymmetries using the BPMs located in this section of beamline.
- Rotate the photocathode puck inside the photogun to minimize its sensitivity to whatever linear polarization is produced by the vacuum window, using RHWP scans as diagnostic. In this step, the objective is to align the axes of photocathode (that exhibit different QE values when illuminated with linearly-polarized light) relative to the birefringence axes of the vacuum window such that the photocathode provides identical electron beam in both helicity states. For example: if the vacuum-window birefringence axes are aligned $\pm 45^\circ$, and introducing linear polarization oriented in the vertical plane, the photocathode QE axes should also be aligned at $\pm 45^\circ$, to minimize helicity-correlated charge and position asymmetries, and more importantly, to minimize a helicity-correlated spot size asymmetry that cannot be measured. (Note, this step requires repeated tunnel accesses.)
- Once the photocathode QE anisotropy axes are properly oriented relative to the vacuum window, find the RHWP angle corresponding to S_1 , where the PITA slope is the largest, i.e., the RHWP angle where the photocathode QE is most sensitive to changes in Pockels cell voltage. For this RHWP setting, adjust Pockels cell voltages to minimize the helicity-correlated charge asymmetry.
- Then choose a RHWP angle near S_2 (i.e. where the PITA slope is small, where the photocathode QE is least sensitive to changes in Pockels cell voltage), and set Pockels cell voltage to minimize helicity-correlated charge asymmetry.
- For the RTP Pockels cell, apply position-difference feedback, applying appropriate voltages (more below) over 10 min time intervals to reduce/minimize helicity-correlated position differences.
- Compare RHWP scans for both IHWP-in and IHWP-out. For PV experiments, where active charge-asymmetry feedback is performed continuously throughout the experiment, the choice of RHWP setting is determined by position difference cancellation considerations. If active charge asymmetry feedback is **not** going to be performed, when choosing the RHWP setting, the requirements of all the experiment halls must be considered, as the RHWP position determines the extent of Pockels cell thermally-induced fluctuations in charge asymmetry.
- Refine RTP voltage settings to minimize position differences in both IHWP-in and IHWP-out configurations, and “turn on” position feedback, verify it works to maintain small helicity-correlated position asymmetries.
- Examine the helicity-correlated position differences further down the injector beam-line, past the chopper, into the MeV region, making sure the position differences remain small and there is no significant clipping on apertures.
- Adjust the laser Intensity Asymmetry controller (IA) settings to minimize the charge asymmetry for beam delivered to the neighboring halls

Feedback loops that run during the experiment, manual adjustments and automated

After setting up the electron gun and laser table and verifying acceptable beam quality at the CEBAF injector, accelerator staff work to deliver the beam to the experiment hall(s). Ideally, the “optics” of the accelerator are set to provide *adiabatic damping* which serves to minimize helicity-correlated beam asymmetries at the experiment hall –

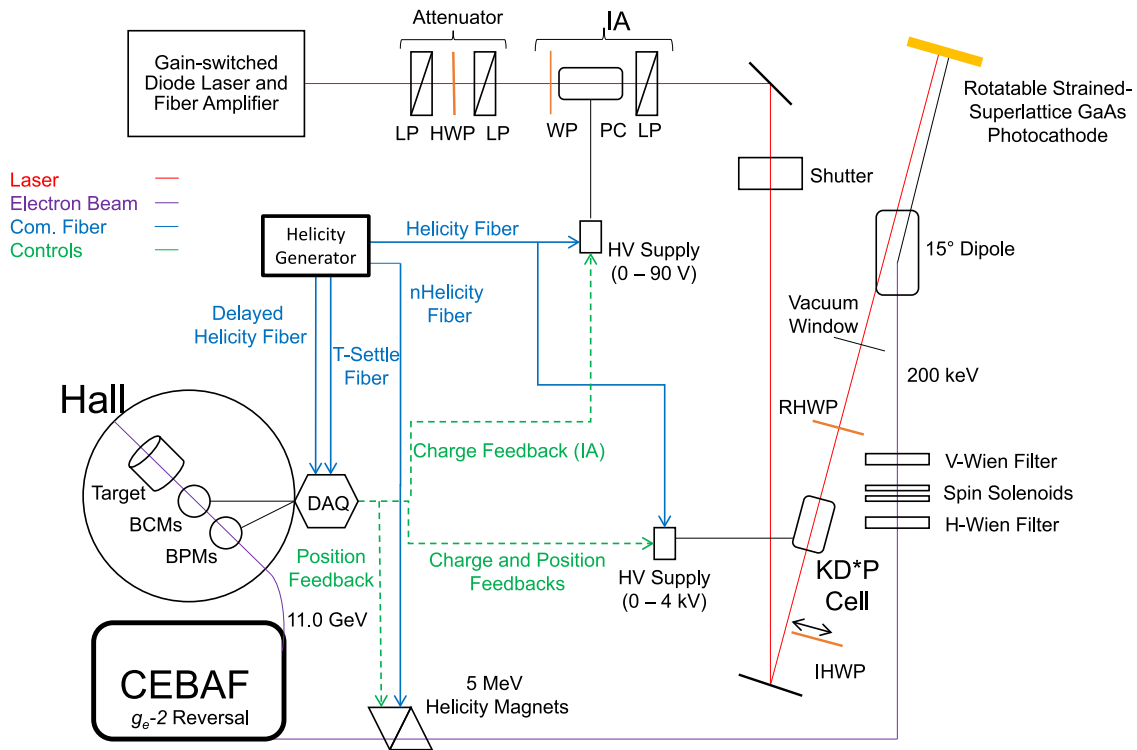


Fig. 12.1. Schematic showing the various methods to implement feedback to reduce the magnitude of helicity-correlated beam asymmetries. In this schematic, the Pockels cell is KD*P. When using an RTP Pockels cell, there are eight Pockels cell control voltages enabling both charge and position asymmetry corrections.

more on this topic in Section 15. But even with optimized laser/optical components and optimized accelerator settings that provide adiabatic damping, feedback is employed to keep helicity-correlated charge and position asymmetries acceptably small. A schematic of the feedback loops employed during PV experiments is shown in Fig. 12.1.

For both types of Pockels cell, KD*P and RTP, charge feedback is implemented by adjusting the voltages applied to the Pockels cell (the so-called PITA process). By adjusting Pockels cell voltages, the drive laser light can possess varying levels of linearly-polarized light, which combined with the QE anisotropy of the photocathode, provides a “knob” to vary the amount of beam current (or charge) in each helicity state. Factors which necessitate charge feedback include slow drifts from temperature fluctuations of the RTP Pockels cell, variations in beam losses at the injector apertures which shift the value of measure helicity-correlated charge asymmetry and the convergence rate and tight experimental goals on charge asymmetry.

Statistically, the theoretical limit for the rate of convergence of the measured helicity-correlated charge asymmetry, A_Q , is between $A_Q \text{ RMS} / \sqrt{N_{\text{interval}}}$ and $A_Q \text{ RMS} / N_{\text{interval}}$ depending on the type of noise being measured. Typically, when feedback is employed, charge asymmetry converges faster than $A_Q \text{ RMS} / \sqrt{N_{\text{interval}}}$ and nearly as fast as $A_Q \text{ RMS} / N_{\text{interval}}$. N_{interval} is the number of patterns during the interval time of interest (running time). One of the biggest challenges for feedback is dealing with accelerator beam trips and subsequent recovery of beam delivered to the hall. Frequent beam trips complicate A_Q feedback convergence. Feedback was performed in 7.5 s intervals at the two RHWP settings, IHWP-in and IHWP-out. After approximately 10 min, the accumulated A_Q measured at injector BPMs converges to < 1 ppm. After approximately 2 h, the accumulated A_Q converged to < 0.1 ppm.

A benefit to using the RTP Pockels cell is that in addition to providing a means to implement helicity-correlated charge feedback, the RTP Pockels cell voltages also provides a means to minimize position asymmetries. When the KD*P Pockels cell is used, position feedback can be implemented using fast-responding steering magnets located in the 5 MeV region of the injector, described below in Section 14.

13. Faster helicity flipping and the new RTP Pockels cell

As mentioned above, experimenters do not take data during the transition between helicity states, which can be described as “dead-time”. Since the start of the PV experimental program at CEBAF, there has been a trend toward faster and faster helicity flipping, for example to address target-thickness variations associated with boiling [110]. This section describes efforts to reduce the deadtime between helicity states to improve the overall efficiency of each PV experiment.

The first Pockels cell high-voltage switch used at CEBAF [174] was homemade and utilized two metal-oxide-semiconductor field-effect transistor (MOSFET) switches capable of driving the cell to ± 2000 V in less than $1 \mu\text{s}$. Unfortunately, at each helicity transition, the voltage would oscillate – or ring – for approximately $500 \mu\text{s}$ before stabilizing. In addition, the MOSFET drive circuitry required relatively high current and this caused the voltage of the regulated high-voltage power supplies feeding the circuitry to “droop”. This voltage droop introduced a long settling time that was evident when using a pseudo-random/non-toggle helicity flip pattern. Specifically, distinct asymmetry values were observed depending on the state of the previous helicity pair (or quartet, or octet, etc.). This phenomenon was termed “Pockels cell memory”, however in hindsight, this behavior was not related to the Pockels cell as much as it was related to the non-constant voltages applied to the Pockels cell. Thinking that problems were related to the “homemade” nature of the switch, it was replaced with a commercial system that was expected to provide much faster rise/fall times and constant voltage throughout the duration of each helicity state (according to the vendor). Surprisingly, the new switch (that also used MOSFET technology) produced nearly identical results. Furthermore, and perhaps more problematic, the commercial switch radiated helicity information that could be picked up by nearby electrical systems. These observations suggested ringing was not a drive circuit problem, but were associated with piezo-electric properties of the KD*P cell [175]. Indeed, in order to obtain a shorter transition to a new helicity state, voltage needed to be applied more slowly to avoid inducing piezo-electric ringing. Whereas a 50 ns switch speed would induce ringing

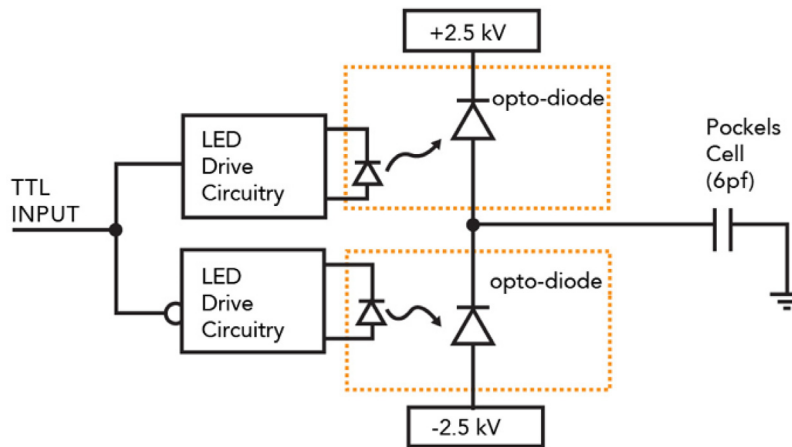


Fig. 13.1. Opto-diode based Pockels cell high-voltage switch.

that made the electron beam unusable for 500 μ s, a slower switch rate that carefully ramped the voltage over 50 μ s provided quality electron beam within 60 μ s.

Knowing that high-speed MOSFET switches were no longer necessary or desirable, a new Pockels cell high-voltage switch was constructed using high-voltage optical diodes that “reverse conduct” when light is applied via light-emitting diodes (LEDs). A custom transistor-to-transistor logic (TTL) drive circuit was designed to sequentially apply light to two optical diodes in series, and thereby flip the polarity of the voltage applied to the Pockels cell (Fig. 13.1). The optical diodes are suitably fast, providing 60 μ s rise/fall times and the capacitance of the switch circuit is very small. Consequently, voltage stability throughout each helicity state was markedly better compared to previous switches, with “Pockels cell memory” small enough to be ignored. Finally, the simplicity of the optical diode switching provided an improved level of confidence in our ability to control parasitic currents that were previously leaking or radiating into the helicity data acquisition systems.

Despite an improved understanding of Pockels cell helicity flipping, further progress was not expected for KD*P Pockels cells because of the material’s intrinsic piezoelectric properties [175]: KD*P provides a transition time minimum of about 60 μ s and cannot be reduced further. As such, KD*P could not satisfy the requirements of the future MOLLER PV experiment which requires a much higher helicity flip rate compared to past experiments, \sim 2 kHz [27]. If the experiment were performed using a KD*P Pockels cell with an optimized helicity transition time of 60 μ s, the experiment would incur deadtime of \sim 12% which is deemed unacceptable for an experiment requiring three years of floor time.

To prepare for the MOLLER PV experiment, a new Pockels cell [91, 176] was developed and evaluated during the recent PREx2 [25] and CREx [26] PV experiments. The new Pockels cell is composed of two crystals made of rubidium titanyl phosphate (RbTiOPO₄ or simply “RTP”) which has a low piezo-electric coefficient [177–179]. Because there is virtually no piezoelectric ringing in RTP crystals, the helicity-transition time was reduced to $<$ 10 μ s. However, compared with KD*P, the optical uniformity of RTP is not as good resulting in poorer extinction ratios, and producing helicity-dependent laser beam motion. In addition, RTP is highly birefringent which means the field uniformity is extremely dependent on the crystal face-cut angles; parallelism between face-cut angles differing by just 0.1 mrad can have significant impact on extinction ratios and helicity-correlated position differences. However, these drawbacks can be overcome – the RTP-based Pockels cell described here provides the best of both worlds: fast transition times between helicity states and improved effective uniformity.

RTP is a biaxial-crystal material frequently used in electro-optical devices. RTP has been used recently for ultra-fast Pockels cell switches

due to its lack of piezo-electric resonances at frequencies up to several hundred MHz. They are also used to quickly turn ON and OFF the electron beam at CEBAF via the tune mode generator, as described above in Section 11. This feature allows the material to withstand impulses during fast electrical switching without exciting strong resonances as occurs in KD*P, thereby avoiding compromising the optical state until ringing diminishes. The transitions for RTP crystals are relatively fast and clean.

RTP crystals have a high-intrinsic birefringence even without an electric field applied. An RTP crystal 1 cm long, standing alone, functions as a \sim 1000th order waveplate at 780 nm. As a result, laser light with typical spectral bandwidth will become depolarized when traversing an RTP crystal. Furthermore, RTP crystals suffer heavily from wavelength and temperature dependence. To avoid depolarization as well as severe wavelength and temperature dependent effects, RTP-based Pockels cell developed for PV experiments are composed of two crystals with their fast and slow axes aligned in opposite orientations, a so-called “thermal compensating” design [176]. With such a design, each crystal provides 1/8 wavelength phase delay, with two crystals in series providing the required quarter wavelength phase delay needed to make circularly-polarized light. But in this configuration, the unwanted temperature and wavelength phase shifts of the first RTP crystal are canceled by the second RTP crystal. The crystals used at CEBAF (Raicol, 12x12x10 mm long, with antireflection coating) were cut very precisely to be of equal length (within 2 μ m) so that the net birefringence is near zero when no voltage is applied. This solution is the same as that employed in making ‘zero-order’ waveplates: use two components of nearly equal lengths with their birefringent axes oriented opposite to one another. Each of the RTP crystals induces equal and opposite phase shifts such that the Pockels cell acts as a zero-order waveplate when inactive. Hence, two RTP crystals are employed in an RTP Pockels cell device to make it nearly zero-order, thereby avoiding the many complications associated with what is effectively an extremely high order waveplate.

All crystals – including KD*P – suffer some degree of optical non-uniformity. In a Pockels cell, refractive index gradients and variations in crystal length across the profile of the cell act as an optical wedge, leading to electric-field dependent beam steering through Snell’s law. In order to counteract this non-uniformity and minimize helicity-correlated beam asymmetries, an innovation in the design of the RTP Pockels cell was required: the cell was designed to control the electric-field magnitudes and electric-field gradients in each crystal. By controlling the electric-field gradients, the helicity-correlated position differences could be suppressed. To implement the design, high-voltage plates were mounted on opposite sides of each crystal in order to induce an electric field. (Although the term “high voltage” is used here, RTP cells with transverse-electric field require significantly lower voltage

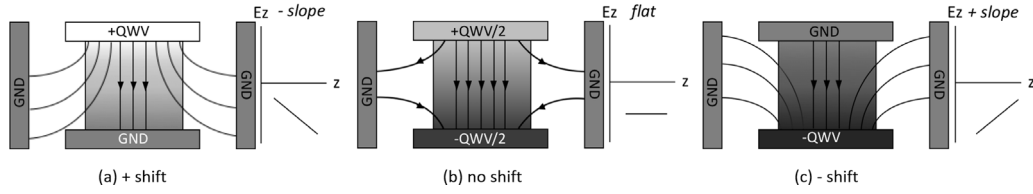


Fig. 13.2. Conceptual diagram of the electric-field gradient control afforded by the RTP Pockels cell design. The electric potential is illustrated by gray-scale and the electric field lines are drawn conceptually. Diagrams a, b and c correspond to + shift, no shift and – shift, respectively. The laser light direction is out of the page [91,176]. QWV: quarter wave voltage, GND: ground potential.

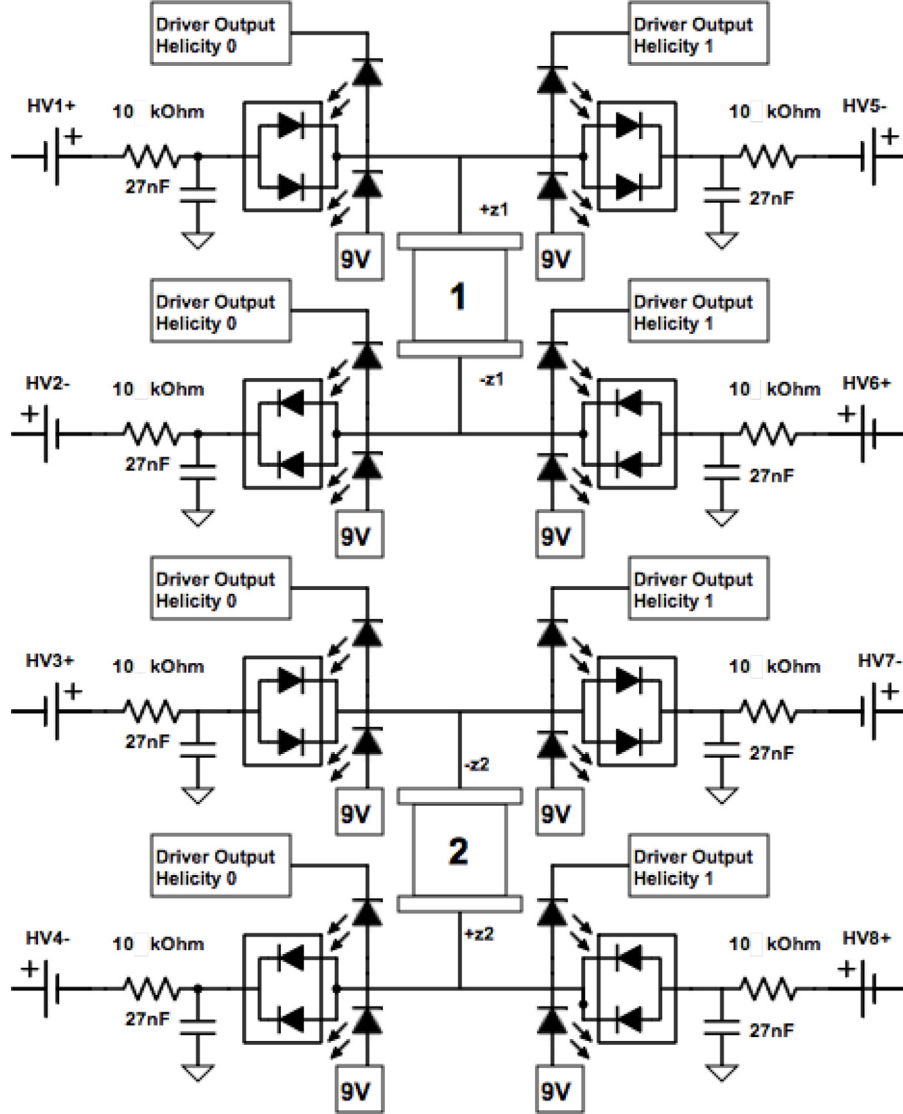


Fig. 13.3. Diagram of the electrical control system for the RTP Pockels cell, with eight voltage supplies and opto-diodes to provide rapid helicity flipping [91,176].

compared to KD*P Pockels cells. Typical RTP voltages are ~ 100 V). Ground plates are attached to the other sides to induce a controlled electric-field gradient. Fig. 13.2 illustrates the range of possible electric-field configurations for a single crystal for a single helicity state. For each situation depicted in the figure, the same net voltage is applied between the top and bottom plates, therefore creating the same electric field, but with differing electric-field gradients induced by shifting the voltage on both plates equally relative to adjacent grounded side panels which affect the field gradient. In this manner, there is independent control of the electric field and the electric-field gradient within each crystal.

For each helicity state, there are four voltages, two voltages per crystal. Voltages are flipped to obtain the other helicity spin state, hence there are eight independent voltages used in total, as shown in Fig. 13.3. Opto-diode switches, as described above, are used to quickly flip the voltages applied to the crystal electrode plates.

The electrode configuration for each crystal is rotated 90° relative to the other, to control beam steering along independent axes (Fig. 13.4, left). A custom designed Pockels cell mount was built to provide control of the relative pitch, roll, yaw, and horizontal/vertical translation between the two crystals, as well as the pitch, roll, yaw and horizontal/vertical translation of the entire assembly (Fig. 13.4, right).

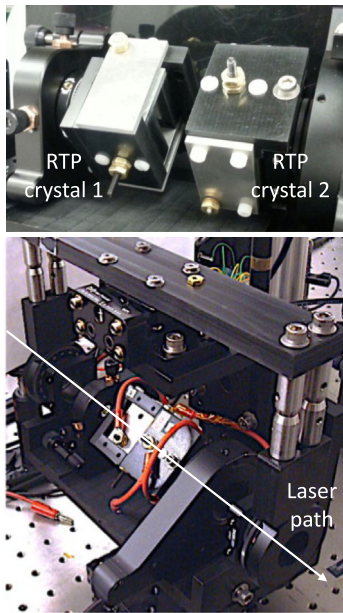


Fig. 13.4. (top): Photograph of the two RTP crystals that make up the RTP Pockels cell, (bottom) the RTP Pockels cell mount that provides pitch, roll and yaw adjustment of the two crystals and the entire apparatus relative to the laser beam [91,176].

In summary, the new RTP Pockels cell provides two benefits compared to KD*P: faster transition times between helicity states and improved effective field uniformity. In this new RTP Pockels cell design, crystal intrinsic non-uniformity effects are counteracted with controlled electric-field gradients so that helicity-correlated beam position motion is controllable and kept at the ~ 10 nrad, 10 nm level, while transition time between helicity states is ~ 10 μ s. The RTP Pockels cell enables feedback to control/minimize helicity-correlated position asymmetry.

14. Helicity magnets

During the G0 forward-angle experiment [11], helicity-correlated position feedback was employed with mixed success. The method relied on moving the laser beam delivered to the photocathode inside the photogun in a helicity-correlated manner. This was accomplished by mounting the last laser table steering mirror (labeled as PZT mirror in Fig. 12.1) to a piezo electric transducer [180]. The method was problematic because beam orbit corrections occurred upstream of injector apertures. Helicity-correlated beam motion induced by the PZT-mirror sometimes created helicity-correlated charge asymmetry, and it was difficult to decouple the two. To address this complication, and to directly influence only the helicity-correlated position asymmetry, steering (dipole) magnets with fast response time were manufactured and installed in the ~ 5 MeV region of the injector, downstream of the quarter cryomodule and all injector apertures. These so-called *helicity magnets* are made of Litz wire [181], which is intended for alternating current applications up to ~ 1 MHz. In this case, however, Litz wire accommodates the relatively fast transition between helicity states, achieving a constant magnetic field in each helicity state within a few microseconds. The helicity magnets are electrically isolated from the accelerator beamline, and are powered using an electrically-isolated electronics rack, to avoid transmitting helicity information to the data streams. There are four helicity magnets, two for horizontal motion and two for vertical motion.

The helicity magnets were commissioned during the Qweak experiment [182] and deemed very effective at minimizing helicity-correlated position asymmetry at the experiment hall. Before employing feedback, the magnet response was characterized at the injector and the

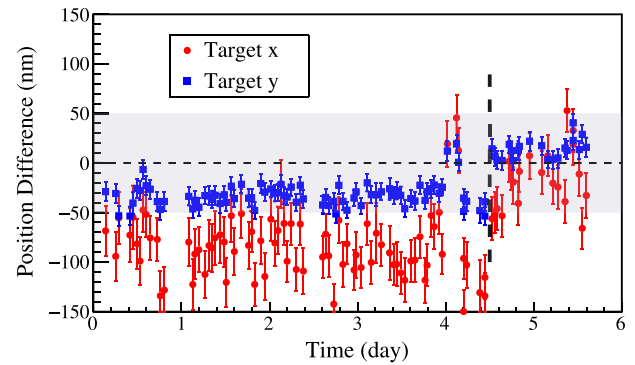


Fig. 14.1. Horizontal and vertical (red and blue, respectively) helicity-correlated position differences at the Qweak target versus time, over a period of six days. The black dashed line marks the beginning of application of feedback from helicity magnets, achieving great improvement in the size of HC differences. Outlying measurements to the left of the black dashed line correspond to tests of the helicity magnets to quantify responses. The gray band corresponds to the desired ± 50 nm range for helicity-correlated position differences.

experiment hall, to determine the appropriate response function. The response function remained stable as long as the accelerator optics remained unchanged. In fact, because machine stability was good, the feedback was applied manually, and not via continuously running automated feedback program. When significant changes were made to the accelerator optics, a new response function was required, but the time required to determine the response function was relatively small (~ 1 h). Fig. 14.1 illustrates the utility of the helicity magnets. When the helicity magnets were employed, the collaboration received beam that met the specification for helicity-correlated position asymmetry, with values in the range of ± 50 nm.

15. Electron beam optics, adiabatic damping and the “phase trombone”

Ideally, the phenomenon known as adiabatic damping [183] would ensure the reduction of the helicity-correlated position asymmetry by a factor of $\sqrt{p_{final}/p_{gun}}$, where p references the electron beam momentum at the photogun and at the experiment hall. For a photogun biased at 100 keV and with final beam energy of 3 GeV, a typical energy for parity experiments, one expects helicity-correlated position damping of the order 100. In reality, deviations from design beam transport can obliterate this damping and even make the helicity-correlated position asymmetry grow. So-called *transport anomalies* can be categorized as cross-plane coupling (XY coupling) and near-singular transport due to grossly mismatched optics (mismatch) which cause beam phase-space (emittance) blowup. (*Mismatch* describes the deviation between real and desired electron beam envelope along the length of the accelerator beamline, aka the betatron wavefunction.) These two effects can compound each other, and the effects can quickly fall out of coherence making it very difficult to simultaneously correct the beam shape and the orbit [184,185]. Helicity-correlated orbit variations are typically 10–100 times smaller than the electron-beam spot size, and can exist without causing beam loss (at least for beam delivered past injector apertures). What follows below is an abbreviated description of adiabatic damping “lessons-learned” from the publications of Y. Chao [184,185], and experiences from Qweak as reported by E. Kargiantoulakis [182].

Methods for Eliminating Transport Anomaly

In 2004, dedicated accelerator time was devoted to characterizing beam transport through five-pass CEBAF in pursuit of maximum adiabatic damping to support the PV program [184,185]. A series of beam-based measurements followed: the technique relied on making intentional helicity-correlated orbits by moving the laser beam at the

photocathode using a mirror attached to a piezoelectric transducer (PZT), synchronized to the helicity flip rate. Comparing the BPM signals in the two helicity states, “difference orbits” could be generated that illustrate the presence (or lack thereof) of adiabatic damping. Analysis of the outcome soon pointed to the low-energy front end as the main source of strong beam phase-space (emittance) blowup. This was primarily attributed to near singular transport across the SRF cavities (the injector quarter cryomodule and full cryomodules) because effective modeling of beam transport through these cavities at such low energy was very difficult. This was likely exacerbated by XY coupling present in the higher order mode couplers of these cavities, leading to phase space blowup described above. Coincidence between jumps in PZT amplitude and locations of the cryomodules was unmistakable. Similar blowup signatures were also observed between the end of the injector (60 MeV) and the two linacs, although at a much lower level. With the above observations, a two-stage strategy was formulated to address transport anomaly and reclaim expected adiabatic damping:

- For 100 keV to 60 MeV beam, with accurately measured transport and sufficient correction elements, develop a model-based solution.
- For 60 MeV to 3 GeV, lacking an accurate long-range model, apply an empirical approach.

100 keV to 60 MeV

Four-dimensional transfer matrices defining transport of the electron beam 4D phase space coordinates (X, X', Y, Y') were measured across all injector cryomodules using the PZT-based difference-orbit method. The result displayed high degrees of near-singularity in the 4D transport, confirming initial suspicions. Furthermore, all measured transfer matrices satisfied the linear 4D symplectic condition, implying proper transport could be restored using only linear elements. An optimization program was developed to use existing quadrupoles and skew quadrupoles to eliminate XY coupling and minimize singularity from 100 keV to 60 MeV while complying with multiple constraints dictated by operation and hardware considerations (e.g., the beam pipe diameter). The solution, once implemented, showed significant improvement in all transport characteristics. The solution eliminated XY coupling and brought singularity in the original transport down to near-ideal levels. Fig. 15.1 shows the BPM difference orbit from 100 keV to 800 MeV, before (blue) and after (orange) corrections were made.

60 MeV to 3 GeV

Beyond the injector, the PZT-induced helicity-correlated orbit variations occurred mainly in the section up to 200 MeV and these were attributed to a number of factors including: imperfect model of the accelerator, field cross talk, and an inaccurate linac energy profile. Although betatron mismatch appeared more dominant than XY coupling, this can still be fertile ground for projected emittance growth given the right amount of otherwise harmless XY coupling. The CEBAF linacs consisted of 20 cryomodules each (now 25 each), with the same HOM-induced coupling. Skew quads were installed near each cryomodule for local compensation. Beam based tests [186] nonetheless suggested that residual coupling could be uncertain by up to 20%. Since XY coupling can add coherently, it was interesting to examine how a betatron mismatch could exacerbate the effect of such coupling. Simulations were carried out to quantify this effect. Different amounts of betatron mismatch were introduced from the injector to the main accelerator, followed by 5-pass propagation in the presence of said residual coupling. Two parameters were examined: projected beam emittance and the beam orbit mismatch factor.

For well-matched beam (Courant Snyder parameter, $CS = 1$), the presence of residual coupling has very little impact on beam emittance. But if $CS = 5$, the projected emittance can be 30 times larger at 3 GeV. Fig. 15.2 shows BPM difference orbits at 3 GeV at experimental Hall A,

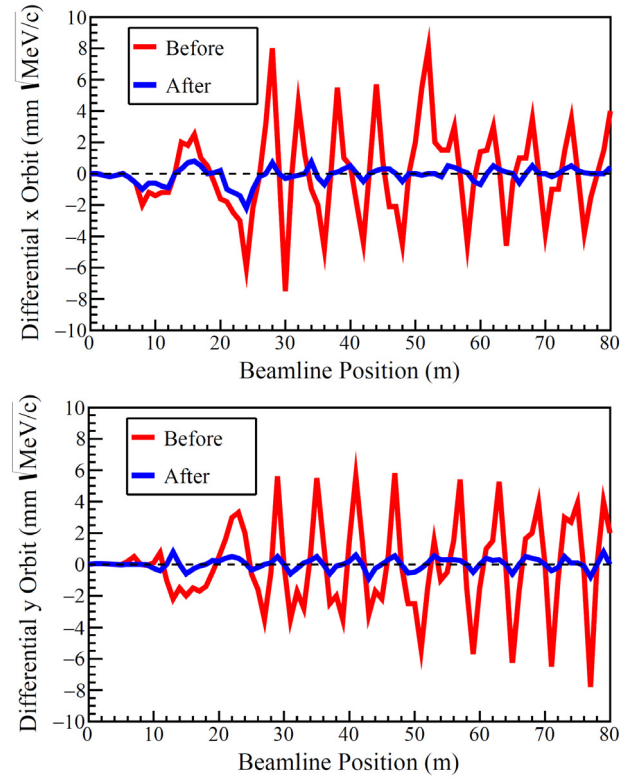


Fig. 15.1. PZT-mirror induced difference orbits before (red) and after (blue) injector matching. The PZT mirror moved the laser at the photocathode in the horizontal plane, and the plots show beam response in horizontal (top) and vertical (bottom) planes. Similar plots were obtained for laser motion in the vertical plane. The beam energy increased from 100 keV to 60 MeV along the X axis. The Y-axis is displayed in units of $\text{mm}\sqrt{\text{MeV}/c}$ to normalize the difference orbit data with respect to beam momentum.

before and after corrections were made. The reduction in difference orbit excursion from cathode to target was significant. This translated into unprecedented small helicity-correlated position difference, as reported by the HAPPEX collaboration [12–14].

Despite the success described above, in practice it is difficult to achieve the desired adiabatic damping, and to date, only HAPPEX II enjoyed small helicity-correlated position differences obtained passively, by virtue of the accelerator setup. During QWeak [21–24], there were unsuccessful attempts to achieve adiabatic damping. Ultimately, position feedback was successfully employed during QWeak using the helicity magnets described in Section 14. For PREXII [25] and CREX [26], exceedingly small helicity-correlated position differences were achieved via feedback applied using the RTP Pockels cell described in Section 13.

Phase trombone

There is an accelerator-optics technique referred to as the “phase trombone” [187] that can be used to minimize helicity-correlated position differences at the experiment target, but at the expense of increasing helicity-correlated beam trajectory/angle differences. For some experiments, this is acceptable. The term “phase” references the betatron phase advance that describes the electron beam envelope along the length of the accelerator beamline. A group of eight quadrupole magnets located in a non-dispersive region of the beam transport line (upstream of the arc) can be used to add or subtract the desired values of the horizontal and vertical phase advance at the target without altering the optics (i.e., the Courant–Snyder parameters, aka, Twiss parameters) in the arc-through-target region. The aforementioned group of eight quadrupole magnets permits independent modification of the horizontal or vertical phase advance over ± 90 degrees. This results in a tradeoff between helicity-correlated position and

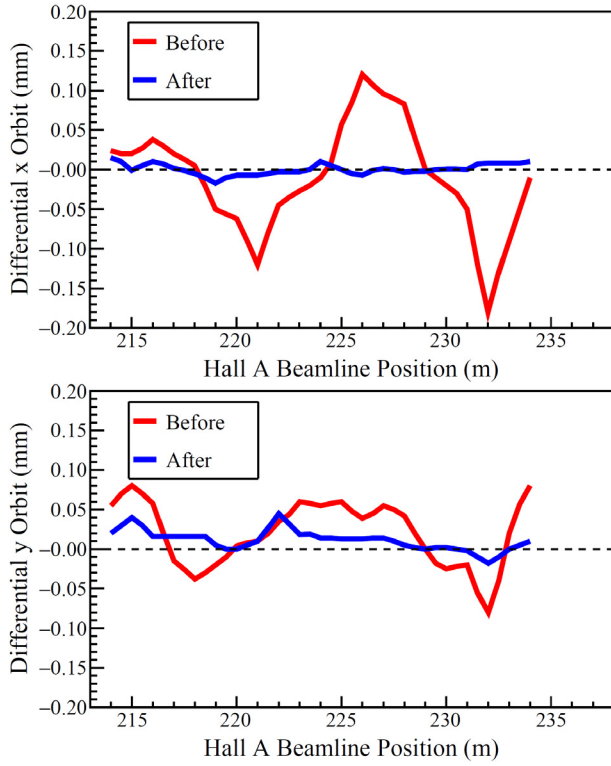


Fig. 15.2. PZT-mirror induced difference orbits at experiment Hall A for 3 GeV beam, before (red) and after (blue) injector matching. The PZT mirror moved the laser at the photocathode in the horizontal plane and the plots show beam response in the horizontal (top) and vertical (bottom) planes. Similar plots were obtained for laser motion in the vertical plane.

angle differences, decreasing one while increasing the other. Besides reducing the magnitude of helicity-correlated position differences, the phase trombone can be employed to reverse the sign of a position difference, to cancel an effect incurred during an earlier part of the experiment.

16. Future work

Of all the completed or proposed PV experiments at CEBAF, the MOLLER PV experiment [27], scheduled for beam delivery during 2025, is the most ambitious PV experiment to date with the smallest predicted physics asymmetry and as a result, the most demanding helicity-correlated beam specifications. Looking at Table 1.1, we must demonstrate improved beam quality for the metrics of charge and position asymmetry. In this final section, a brief description of planned accelerator improvements is presented to address the MOLLER-specific challenges.

During the upcoming 2023 Scheduled Accelerator Down, the long-discussed injector upgrade will be completed, and this is expected to improve the beam quality for PV experiments by eliminating injector transport anomalies described above in Section 15. The present CEBAF photoinjector (Section 7) employs a DC high-voltage photogun biased at 130 kV, a normal conducting copper-cavity “capture” section used to accelerate the beam from the photogun to ~630 keV and the quarter cryomodule that contains two 1497 MHz SRF five-cell cavities similar to those used in full cryomodules, to reach the photoinjector design energy of ~5 MeV. Although very reliable, beam passing through the quarter cryomodule suffers a significant transverse deflection caused by asymmetric fields that are present on the beamline axis stemming from the design and implementation of the RF fundamental power couplers and stub tuners [188–190]. In addition, there is strong coupling of

XY motion which makes it difficult to set the optics on either side of quarter cryomodule to obtain a matched beta function across the quarter cryomodule, which in turn limits the achievable adiabatic damping that can be obtained for beam delivered to the experiment halls.

To address these issues, a new cryomodule was constructed to replace the quarter cryomodule. The so-called “booster” cryomodule [191,192] is composed of a 2-cell superconducting capture section, and a 7-cell superconducting cavity that provides most of the beam acceleration. The booster employs modern forward power couplers and stub tuners [193–198] to eliminate or greatly reduce the transverse beam deflection associated with the induced electric fields inside the cavities, and a modern higher order mode damper [199] that provides inherent up/down symmetry, which reduces the skew quadrupole contribution to the field to nearly zero, which in turn significantly reduces the XY coupling. In addition, the CEBAF photoinjector will become less complicated, with fewer RF components – since the room temperature capture cavity will be removed – with space made available for more beamline diagnostics such as BPMs. Injector setup should be easier using optics matching tools [200] to set focusing strength of elements on both sides of the booster to improve lattice matching in support of enhanced adiabatic damping. And because the photogun will be biased at 200 kV, beam will be stiffer resulting in less beamloss at injector apertures used to set the launch into critical downstream components.

Recently, the 2-Wien spin flipper and baked injector beamline was reconfigured to address the poor choice of placement of the pre-injector prebuncher. Besides accomplishing “spin manipulation”, Wien filters also serve as very sensitive “beam energy analyzers”, with the beam trajectory unperturbed only for a very precise beam energy. Originally, the prebuncher was placed upstream of the horizontal Wien filter. As a result, the beam orbit could change significantly downstream of the horizontal Wien filter when the phase of the RF signals applied to the photogun drive lasers or prebuncher were adjusted, sometimes necessitating lengthy periods of beam tuning to restore parity-quality beam (the prebuncher can add/subtract energy from the beam if the electron bunches do not arrive at “zero-crossing”). By placing the prebuncher downstream of the horizontal Wien, we expect to eliminate this complication, maintaining a constant beam trajectory even when the RF phases of the laser and prebuncher are adjusted. Importantly, this beamline modification should make it easier to implement feedback with the horizontal Wien filter to minimize transverse polarization at the MOLLER target.

As an alternative to using the horizontal Wien filter of the 2-Wien spin flipper to zero the transverse component of the polarization for the MOLLER PV experiment, via automated feedback, it could be more effective and less troublesome to install an additional horizontal Wien filter in the ~6 MeV portion of the injector beamline. The new Wien filter would be located downstream of all injector apertures. As a result, the feedback associated with zeroing the transverse polarization would be decoupled from the other feedback loops designed to minimize helicity-correlated beam asymmetries, and therefore less likely to introduce unintended consequences. Although the MeV Wien filter would only be required to rotate polarization by just a few degrees, the electrodes would need to be longer than those used in the keV Wien filters, and providing higher field strengths.

Although the systematic error associated with helicity-correlated spot size variations can be bounded using the 180° “slow” helicity spin flip provided by the two-Wien spin flipper, there are two ideas worth pursuing that could possibly provide a more quantitative assessment of an experiment’s sensitivity to helicity-correlated spot size variations. Accelerator physicists at KEK have demonstrated non-invasive beam spot size measurements based on a multipole-moment analysis of the electromagnetic fields excited by the beam inside a BPM possessing eight antennas [201]. Such BPMs could be added to the CEBAF injector and hall beamlines to directly measure the helicity-correlated spot size variations. And related to this, the helicity dipole magnets described

in Section 14 could be rewired to function as quadrupole magnets. In such a configuration, the beam size could be intentionally varied in a helicity-correlated manner, to directly measure experimental sensitivity to helicity-correlated spot size variation, or together with the KEK-style BPM, feedback could be applied to minimize helicity-correlated spot size variations.

Because the MOLLER experiment requires electron beam at 11 GeV, the total number of spin rotations in the CEBAF arcs will be large, of the order 120π . As a result, it will be possible to provide a desired “slow” helicity spin flip – while maintaining very similar electron-beam optical properties – by changing the beam energy by only a relatively small amount (~ 93 MeV). This type of helicity reversal is referred to as a $g - 2$ reversal where g is the “ g -factor” related to the anomalous magnetic moment a by the expression, $a = \frac{g-2}{2}$. This can be accomplished by reducing the gradient of each linac by just 4.6 MeV, since beam passes through each linac five times. This small change in linac gradient should have very little impact of the accelerator optics. Similarly, invasive modifications to the experiment configuration are not expected. As a result, the backgrounds and spectrometer optics should remain very similar. For these reasons, this type of helicity reversal is expected to be very effective, changing only the sign of the measured scattering asymmetry. However, since this method is disruptive to other halls, MOLLER expects to employ a $g - 2$ reversal only a few times over the duration of the entire multi-year run.

Finally, BCM sensitivity to beam position should be evaluated on the bench using the Goubau Line apparatus [103] described in Section 5, together with beam-based evaluation.

Declaration of competing interest

The authors declare that they have no known competing financial interests or personal relationships that could have appeared to influence the work reported in this paper.

Data availability

Data will be made available on request.

Acknowledgments

Notice: Authored by Jefferson Science Associates under U.S. DOE Contract No. DE-AC05-84ER40150 and with funding from the DOE Office of High Energy Physics and the Americas Region ILC R&D program. The U.S. Government retains a non-exclusive, paid-up, irrevocable, world-wide license to publish or reproduce this manuscript for U.S. Government purposes.

Special thanks to the many people who contributed to this work, including the HAPPEX, G0 and QWeak collaborations, members of the Engineering Division, members of the Accelerator Division and past members of the electron gun group.

References

- [1] C.W. Leemann, D.R. Douglas, G.A. Krafft, The continuous electron beam accelerator facility: CEBAF at the Jefferson Laboratory, *Annu. Rev. Nucl. Part. Sci.* 51 (2001) 413.
- [2] P. Adderley, et al., CEBAF at 12 GeV, in preparation. expected publication 2023..
- [3] New insights into the structure of matter: the first decade of science at Jefferson Lab, *J. Phys. Conf. Ser.* (ISSN: 1742-6588) 299 (2011).
- [4] L. Cardman, R. Ent, N. Isgur, J.M. Laget, C. Leemann, C. Meyer, Z.E. Meziani, The science driving the 12 GeV upgrade of CEBAF, 2011, United States. <https://www.osti.gov/servlets/purl/1345054>.
- [5] D.S. Armstrong, R.D. McKeown, Parity-violating electron scattering and the electric and magnetic strange form factors of the nucleon, *Annu. Rev. Nucl. Part.* 62 (2012) 337.
- [6] Reza Kazimi, Joseph Grames, John Hansknecht, Alicia Hofler, George Lahti, Tomasz Plawski, Matt Poelker, Riad Suleiman, Yan Wang, Four-beam generation for simultaneous four-hall operation at CEBAF, in: *Proceedings, 7th International Particle Accelerator Conference, IPAC 2016, Busan, Korea, May, 2016*, pp. 8–13, <http://dx.doi.org/10.18429/JACoW-IPAC2016-THPOY060>.
- [7] R. Kazimi, A. Freyberger, J. Grames, J. Hansknecht, A. Hofler, T. Plawski, M. Poelker, M. Spata, Y. Wang, Operational results of simultaneous four-beam delivery at Jefferson Lab, in: *Proc. of the 10th International Particle Accelerator Conference, IPAC'19 Melbourne, Australia, 2019*, pp. 19–24.
- [8] K.A. Aniol, et al., Measurement of the neutral weak form factors of the proton, *Phys. Rev. Lett.* 82 (1999) 1096, <http://dx.doi.org/10.1103/PhysRevLett.82.1096>.
- [9] K.A. Aniol, et al., New measurement of parity violation in elastic electron-proton scattering and implications for strange form factors, *Phys. Lett. B* 509 (2001) 211, [http://dx.doi.org/10.1016/S0370-2693\(01\)00446-4](http://dx.doi.org/10.1016/S0370-2693(01)00446-4).
- [10] K.A. Aniol, et al., Parity-violating electroweak asymmetry in e^-p scattering, *Phys. Rev. C* 69 (2004) 065501, <http://dx.doi.org/10.1103/PhysRevC.69.065501>.
- [11] D.S. Armstrong, et al., Strange-quark contributions to parity-violating asymmetries in the forward G0 electron-proton scattering experiment, *Phys. Rev. Lett.* 95 (2005) 092001, <http://dx.doi.org/10.1103/PhysRevLett.95.092001>.
- [12] K.A. Aniol, et al., Parity-violating electron scattering from ^4He and the strange electric form factor of the nucleon, *Phys. Rev. Lett.* 96 (2006) 022003, <http://dx.doi.org/10.1103/PhysRevLett.96.022003>.
- [13] A. Acha, et al., Precision measurements of the nucleon strange form factors at $Q^2 \sim 0.1$ GeV², *Phys. Rev. Lett.* 98 (2007) 032301, <http://dx.doi.org/10.1103/PhysRevLett.98.032301>.
- [14] K.A. Aniol, et al., Constraints on the nucleon strange form factors at $Q^2 \sim 0.1$ GeV², *Phys. Lett. B* 635 (2006) 275, <http://dx.doi.org/10.1016/j.physletb.2006.03.011>.
- [15] D. Androić, et al., Strange quark contributions to parity-violating asymmetries in the backward angle G0 electron scattering experiment, *Phys. Rev. Lett.* 104 (2010) 012001, <http://dx.doi.org/10.1103/PhysRevLett.104.012001>.
- [16] Z. Ahmed, et al., New precision limit on the strange vector form factors of the proton, *Phys. Rev. Lett.* 108 (2012) 102001, <http://dx.doi.org/10.1103/PhysRevLett.108.102001>.
- [17] D. Wang, et al., Measurements of parity-violating asymmetries in electron-deuteron scattering in the Nucleon Resonance Region, *Phys. Rev. Lett.* 111 (2013) 082501, <http://dx.doi.org/10.1103/PhysRevLett.111.082501>.
- [18] D. Wang, et al., Measurement of parity violation in electron-quark scattering, *Nature* 506 (2014) 67, <http://dx.doi.org/10.1038/nature12964>.
- [19] D. Wang, et al., Measurement of parity-violating asymmetry in electron-deuteron inelastic scattering, *Phys. Rev. C* 91 (2015) 045506, <http://dx.doi.org/10.1103/PhysRevC.91.045506>.
- [20] S. Abrahamyan, et al., Measurement of the neutron radius of ^{208}Pb through parity violation in electron scattering, *Phys. Rev. Lett.* 108 (2012) 112502, <http://dx.doi.org/10.1103/PhysRevLett.108.112502>.
- [21] D. Androić, et al., First determination of the weak charge of the proton, *Phys. Rev. Lett.* 111 (2013) 141803, <http://dx.doi.org/10.1103/PhysRevLett.111.141803>.
- [22] D. Androić, et al., Precision measurement of the weak charge of the proton, *Nature* 557 (2018) 207, <http://dx.doi.org/10.1038/s41586-018-0096-0>.
- [23] D. Androić, et al., Parity-violating inelastic electron-proton scattering at low Q^2 above the resonance region, *Phys. Rev. C* 101 (2020) 055503, <http://dx.doi.org/10.1103/PhysRevC.101.055503>.
- [24] D. Androić, et al., Determination of the ^{27}Al neutron distribution radius from a parity-violating electron scattering measurement, *Phys. Rev. Lett.* 128 (2022) 132501, <http://dx.doi.org/10.1103/PhysRevLett.128.132501>.
- [25] D. Adhikari, et al., Accurate determination of the neutron skin thickness of ^{208}Pb through parity-violation in electron scattering, *Phys. Rev. Lett.* 126 (2021) 172502, <http://dx.doi.org/10.1103/PhysRevLett.126.172502>.
- [26] D. Adhikari, et al., Precision determination of the neutral weak form factor of ^{48}Ca , *Phys. Rev. Lett.* 129 (2022) 042501, <http://dx.doi.org/10.1103/PhysRevLett.129.042501>.
- [27] J. Benesch, et al., The MOLLER experiment: An ultra-precise measurement of the weak mixing angle using Møller scattering, <http://dx.doi.org/10.48550/arXiv.1411.4088>, arXiv:1411.4088.
- [28] SoLID (Solenoidal Large Intensity Device), Updated Preliminary Conceptual Design Report, the SoLID Collaboration, 2019, <https://solid.jlab.org/DocDB/0002/000282/001/solid-precd-2019Nov.pdf>.
- [29] C.K. Sinclair, Accelerator setups which provide longitudinal beam polarization to more than one experimental hall simultaneously, Jefferson Lab Technical Note TJNAF-TN-96-032.
- [30] C.K. Sinclair, Beam energy combinations which provide simultaneous longitudinal electron polarization in two experimental halls, Jefferson Lab Technical Note TJNAF-TN-97-021.
- [31] J. Grames, Magic energies for the 12 GeV upgrade, Jefferson Lab Technical Note TJNAF-TN-04-042.
- [32] D.W. Higinbotham, Electron spin precession at CEBAF, AIP Conf. Proc. 1149 (2009) 751, <http://dx.doi.org/10.1063/1.3215753>, arXiv:0901.4484.

- [33] D.W. Higinbotham, Using polarimetry to determine the CEBAF beam energy, 2013, p. 014, <http://dx.doi.org/10.22323/1.182.0014>, PoS PSTP2013.
- [34] M. Hauger, et al., Nuclear instruments and methods in physics research A462, 2001, p. 382.
- [35] A. Narayan, et al., Precision electron-beam polarimetry at 1 GeV using diamond microstrip detectors, Phys. Rev. X 6 (2016) 011013.
- [36] J. Magee, et al., A novel comparison of Møller and Compton electron-beam polarimeters, Phys. Lett. B 766 (2017) 339–344.
- [37] V. Glamazdin, et al., Fizika B 8 (1999) 91, hep-ex.
- [38] O. Glamazdin, Nuovo Cimento C 35 (2012) 176, <http://dx.doi.org/10.1393/ncc/i2012-11275-8>.
- [39] S. Escoffier, et al., Nucl. Instrum. Methods A 551 (2005) 563, <http://dx.doi.org/10.1016/j.nima.2005.05.067>, physics.
- [40] CLAS Collab, B.A. Mecking, et al., Nucl. Instrum. Methods A 503 (2003) 513, [http://dx.doi.org/10.1016/S0168-9002\(03\)01001-5](http://dx.doi.org/10.1016/S0168-9002(03)01001-5).
- [41] J.M. Grames, C.K. Sinclair, M. Poelker, X. Roca-Maza, M.L. Stutzman, R. Suleiman, Md. A. Mamun, M. McHugh, D. Moser, J. Hansknecht, B. Moffitt, T.J. Gay, High precision 5 MeV Mott polarimeter, Phys. Rev. C 102, 015501.
- [42] J.M. Grames, C.K. Sinclair, J. Mitchell, E. Chudakov, H. Fenker, A. Freyberger, D.W. Higinbotham, M. Poelker, M. Steigerwald, M. Tiefenback, C. Cavata, S. Escoffier, F. Marie, T. Pussieux, P. Vernin, S. Danagoulian, V. Dharmawardane, R. Fatemi, K. Joo, M. Zeier, V. Gorbenco, R. Nasseripour, B. Raue, R. Suleiman, B. Zihlmann, Unique electron polarimeter analyzing power comparison and precision spin-based energy measurement, Phys. Rev. ST Accel. Beams 7 (2010) 042802; Phys. Rev. ST Accel. Beams 13 (2004) 069901, Published 19; Erratum.
- [43] K. Aulenbacher, E. Chudakov, D. Gaskell, J. Grames, K.D. Paschke, Precision electron beam polarimetry for next generation nuclear physics experiments, Internat. J. Modern Phys. E 27 (2018) 7, <http://dx.doi.org/10.1142/S0218301318300047>, 1830004 (57 pages).
- [44] S.M. Sze, Physics of Semiconductor Devices, John Wiley & Sons, New York, 1981.
- [45] J.S. Blakemore, et al., Semiconducting and other major properties of gallium arsenide, J. Appl. Phys. 53 (1982) R123.
- [46] D.T. Pierce, F. Meier, P. Zurcher, Appl. Phys. Lett. 26 (1975) 670.
- [47] J. Kessler, Polarized Electrons, Springer-Verlag, Berlin, 1985.
- [48] B.M. Dunham (Ed.), Investigation of the Physical Properties of Photoemission Polarized Electron Sources for Accelerator Applications, (Ph. D. Thesis), University of Illinois at Urbana-Champaign, 1993.
- [49] G.L. Bir, A.G. Aronov, G.E. Piku, Spin relaxation of electrons due to scattering by holes, Sov. Phys.-JETP 42 (1976) 705.
- [50] M.I. D'Yakonov, V.I. Perel, Sov. Phys.-JETP 33 (1971) 1053.
- [51] R.J. Elliott, Phys. Rev. 96 (1954) 266, Y. Yafet, Solid State Physics, vol 14, chapter1, page 1. Academic Press, 1963.
- [52] M. Zolotarev, Effect of Radiation Trapping on Polarization of Photoelectrons from Semiconductors, SLAC Pub 432, 1994, p. 435.
- [53] Wei Liu, Matt Poelker, Xincun Peng, Shukui Zhang, Marcy Stutzman, A comprehensive evaluation of factors that influence the spin polarization of electrons emitted from bulk GaAs photocathodes, J. Appl. Phys. 122 (2017) 035703.
- [54] T. Maruyama, et al., Observation of strain-enhanced electron-spin polarization in photoemission from InGaAs, Phys. Rev. Lett. 66 (1991) 2376.
- [55] T. Nakanishi, H. Aoyagi, H. Horinaka, Yu. Kamiya, T. Kato, S. Nakamura, T. Saka, M. Tsubata, Large enhancement of spin polarization observed by photoelectrons from a strained GaAs layer, Phys. Lett. A 158 (6–7) (1991) 345–349.
- [56] Yu.A. Mamaev, Yu.P. Yashin, A.V. Subashiev, et al., Phys. Low Dim. Struct. 7 (1994) 27.
- [57] Yu. P. Yashin, Yu. A. Mamaev, A.N. Ambrazhei, in: Yu. A. Mamaev, et al. (Eds.), Proc. of the Low Energy Polarized Electron Workshop LE-98, St.-Petersburg, SPES-Lab-Pub., 1998, p. 27, 1998.
- [58] T. Omori, Y. Kurichara, Y. Takeuchi, et al., Jpn. Journ. Appl. Phys. 33 (1994) 5676.
- [59] T. Nakanishi, S. Okumi, M. Tavana, et al., in: C.W.D. de Jager, et al. (Eds.), Proc. of 12th International Symposium on High-Energy Spin Physics, Amsterdam, 1996, World Scientific, 1997, p. 712.
- [60] Yu. A. Mamaev, A.V. Subashiev, Yu. P. Yashin, et al., Phys. Low Dim. Struct. 10 (1995) 61.
- [61] T. Nakanishi, S. Okumi, K. Togawa et al., Polarized gas targets and polarized beams, in: R. Holt, et al. (Eds.), 7th Intern. Workshop, Urbana, 1997, in: AIP Conf. Proc. c., vol. 421, 1997, p. 300.
- [62] T. Maruyama, D.-A. Luh, A. Brachmann, J.E. Clendenin, E.L. Garwin, S. Harvey, J. Jiang, R.E. Kirby, A.M. Moy, R. Prepost, C.Y. Prescott, Systematic study of polarized electron emission from strained GaAs/ GaAsP superlattice photocathodes, Appl. Phys. Lett. 85 (2004) 2640.
- [63] Strained-layer GaAs photocathode from bandwidth semiconductor, LLC, 25 Sagamore Park Drive, Hudson, NH 03051, <https://www.bandwidthsemi.com>.
- [64] Strained-superlattice GaAs/GaAsP photocathode SVT associates, Inc. 7620 Executive drive, Eden Prairie, MN 55344, <http://www.svta.com>.
- [65] T. Saka, T. Kato, T. Nakanishi, M. Tsubata, K. Kishino, H. Horinaka, Y. Kamiya, S. Okumi, C. Takahashi, Y. Tanimoto, et al., New-type photocathode for polarized electron source with distributed Bragg reflector, Japan. J. Appl. Phys. 32 (1993) 1837.
- [66] J.C. Grobli, D. Oberli, F. Meier, Polarization resonances of optically spin-oriented photoelectrons emitted from strained semiconductor photocathodes, Phys. Rev. Lett. 74 (1995) 2106.
- [67] L.G. Gerchikov, K. Aulenbacher, J.E. Clendenin, V.V. Kuz'michev, Y.A. Mamaev, T. Maruyama, V.S. Mikhlin, J.S. Roberts, V.M. Ustinov, D.A. Vasilev, A.P. Vasiliev, Y.P. Yashin, A.E. Zhukov, Highly effective polarized electron sources based on strained semiconductor superlattice with distributed Bragg reflector, AIP Conf. Proc. 980 (2008) 124.
- [68] S. Zhang, M.L. Stutzman, M. Poelker, Y. Chen, Aaron Moy, Observation of significant quantum efficiency enhancement from a polarized photocathode with distributed Bragg reflector, in: Proceedings of IPAC2015, Richmond, USA, 2015.
- [69] Wei Liu, Yiqiao Chen, Wentao Lu, Aaron Moy, Matt Poelker, Marcy Stutzman, Shukui Zhang, Record-level quantum efficiency from a high polarization strained GaAs/GaAsP superlattice photocathode with distributed Bragg reflector, Appl. Phys. Lett. 109 (2016) 252104.
- [70] Xiuguang Jin, Naoto Yamamoto, Yasuhide Nakagawa, Atsushi Mano, Takanori Kato, Masatoshi Tanioku, Toru Ujihara, Yoshikazu Takeda, Shoji Okumi, Masahiro Yamamoto, Tsutomu Nakanishi, Takashi Saka, Hiromichi Horinaka, Toshihiro Kato, Tsuneo Yasue, Takanori Koshikawa, Super-high brightness and high-spin-polarization photocathode, Appl. Phys. Express 1 (2008) 045002.
- [71] X. Jin, A. Mano, N. Yamamoto, Y. Takeda, High-performance spin-polarized photocathodes using a GaAs/GaAsP strain-compensated superlattice, Appl. Phys. Express 6 (2013) 015801, <http://dx.doi.org/10.7567/APEX.6.015801>.
- [72] F. Pockels, Abhandlungen Der Gesellschaft Der Wissenschaften Zu Gottingen, Vol. 39, p. 11893.
- [73] F. Pockels, Lehrbuch Der Kristallographie, Leipzig, 1906.
- [74] B.H. Billings, The electro-optic effect in uniaxial crystals of the type XH_2PO_4 ; I, theoretical, J. Opt. Soc. Am. 39 (1949) 797, <http://dx.doi.org/10.1364/JOSA.39.000797>.
- [75] B.H. Billings, The electro-optic effect in uniaxial crystals of the type XH_2PO_4 , II experimental, J. Opt. Soc. Am. 39 (1949) 802, <http://dx.doi.org/10.1364/JOSA.39.000802>.
- [76] B.H. Billings, The electro-optic effect in uniaxial crystals of the type XH_2PO_4 , III, Measur. Coefficients 40 (4) (1950) 225–229, <http://dx.doi.org/10.1364/JOSA.40.000225>.
- [77] E. Lebiush, R. Lavi, Y. Tsuk, N. Angert, A. Gachechiladze, M. Tseitlin, A. Zharov, M. Roth, RTP as a Q-switch for high repetition rate application, in: Proceedings of the Conference Advanced Solid-State Lasers Trends Opt. Photonics Ser. Vol. 34, 2000, pp. 63–65.
- [78] M. Roth, N. Angert, M. Tseitlin, Potassium Titanyl Phosphate (KTP) - An oxide of choice for nonlinear optical and electro-optic applications, in: Proceedings of the 2nd Israeli-Russian Workshop on the Optimization of Composition, Structure and Properties of Metals, Oxides, Composites, Nanomaterials and Amorphous Materials, Jerusalem, 2003, pp. 233–235.
- [79] M. Roth, N. Angert, M. Tseitlin, G. Wang, T.P.J. Han, H.G. Gallagher, N.I. Leonyuk, E.V. Kopylovina, S.N. Barilo, L.A. Kurnevich, Recent developments in crystal growth and characterization of nonlinear optical borate and phosphate materials, in: Proceedings of the III International Conference Single Crystal Growth, Strength Problems, and Heat and Mass Transfer, Obninsk, Vol. 2, 2000, pp. 416–426.
- [80] K.D. Paschke, Controlling helicity-correlated beam asymmetries in a polarized electron source, Eur. Phys. J. A 32 (2007) 549–553.
- [81] K.D. Paschke, Sources of helicity-correlated electron beam asymmetries, in: Proceedings of the 18th International Spin Physics Symposium, SPIN2008, in: AIP Conf. Proc., vol. 1149, 2008, p. 853.
- [82] T.B. Humensky, R. Alley, A. Brachmann, M.J. Browne, G.D. Cates, J. Clendenin, J. deLamare, J. Frisch, T. Galetto, E.W. Hughes, K.S. Kumar, P. Mastromarino, J. Sodja, P.A. Souder, J. Turner, M. Woods, SLAC's polarized electron source laser system and minimization of electron beam helicity correlations for E-158 parity violation experiment, Nucl. Instrum. and Meth. A 521 (2004) 261.
- [83] Brian Thomas Humensky, Probing the Standard Model and Nucleon Structure Via Parity-Violating Electron Scattering, (Ph.D. thesis), Princeton University, 2003.
- [84] Peter Mastromarino, T. Brian Humensky, Perry Anthony, Carlos Arroyo, Klejda Bega, Axel Brachmann, Gordon Cates, James Clendenin, Franz-Josef Decker, Ted Fieguth, Emlin Hughes, G. Mark Jones, Yuri Kolomensky, Krishna Kumar, David Relyea, Steve Rock, Owen Saxton, Zen Szalata, Jim Turner, Mike Woods, Helicity-correlated systematics for SLAC experiment E158, IEEE Trans. Nucl. Sci. 49 (3) (2002).
- [85] Marcos Zayat, David Almendro, Virginia Vadillo, David Levy, Sol-Gel Materials for Optics and Electrooptics Handbook of Sol-Gel Science and Technology, ISBN: 978-3-319-19454-7, 2017.
- [86] Thibault Dartigalongue, François Hache, Precise alignment of a longitudinal pockels cell for time-resolved circular dichroism experiments, J. Opt. Soc. Am. B 20 (8) (2003) 1780, <http://dx.doi.org/10.1364/JOSAB.20.001780>.

- [87] R.L. Goldstein, User's Guide for BBO, KD*P, RTP and Lithium Niobate Q-switches and Modulators for Q-switching, Chopping and Pulse Extraction, instruction manual from Fast Pulse Technologies, Inc..
- [88] R.A. Mair, R. Prepost, H. Tang, E.L. Garwin, T. Maruyama, G. Mulholland, Anisotropies in strain and quantum efficiency of strained GaAs grown on GaAsP, *Phys. Lett. A* 212 (1996) 231–236.
- [89] T. Maruyama, D.-A. Luh, A. Brachmann, J.E. Clendenin, E.L. Garwin, S. Harvey, J. Jiang, R.E. Kirby, C.Y. Prescott, R. Prepost, A.M. Moy, Systematic study of polarized electron emission from strained GaAs/GaAsP superlattice photocathodes, *Appl. Phys. Lett.* 85 (13) (2004) 27, <http://dx.doi.org/10.1063/1.1795358>.
- [90] Rupesh Silwal, Probing the Strangeness Content of the Proton and the Neutron Radius of ^{208}Pb using Parity-Violating Electron Scattering (Ph.D. thesis), University of Virginia, 2012.
- [91] C. Palatchi, Laser and Electron Beam Technology for Parity Violating Electron Scattering Measurements (Ph.D. thesis), University of Virginia, 2019, <http://dx.doi.org/10.18130/v3-vvcs-m369>.
- [92] N. Solmeyer, K. Zhu, D.S. Weiss, Note: Mounting ultra-high vacuum windows with low stress-induced birefringence, *Rev. Sci. Instrum.* 82 (2011) 066105, <http://dx.doi.org/10.1063/1.3606437>.
- [93] CEBAF electronic logbook entry: <https://logbooks.jlab.org/entry/3855100>.
- [94] L. Merminga, J.J. Bisognano, C. Hovater, G.A. Krafft, S.N. Simrock, K. Kubo, Operation of the CEBAF linac with high beam loading, in: Proceedings of the Particle Accelerator Conference, Washington, D.C, 1993, <http://dx.doi.org/10.1109/PAC.1993.309702>.
- [95] Edward Thoenig, Transient Beam Loading Studies in Radiofrequency Cavities (Masters thesis), The University of British Columbia, 2018.
- [96] T. Plawski, T. Allison, R. Bachimanchi, H. Dong, C. Hovater, J. Musson, New RF control system for the 12 GeV energy upgrade of the CEBAF accelerator at Jefferson Lab, in: Proc. of SPIE 7124 71240J-2, <http://dx.doi.org/10.1117/12.817948>.
- [97] Alexander Wu Chao, Karl Hubert Mess, Maury Tigner, Frank Zimmermann (Eds.), Handbook of Accelerator Physics and Engineering, World Scientific, Hackensack, USA, 2013, doi:10.1142/8543.
- [98] C. Yan, P. Adderley, D. Barker, J. Beaufait, K. Capek, R. Carlini, J. Dahlberg, E. Feldt, K. Jordan, B. Kross, W. Oren, R. Wojcik, J. VanDyke, Superharp - A wire scanner with absolute position readout for beam energy measurement at CEBAF, *Nucl. Instrum. Meth. A* 365 (1995) 261.
- [99] K. Wittenburg, Summary of the joint ARIES-ADA workshop on scintillation screens and optical technology for transverse profile measurements, in: Joint ARIES-ADA Workshop on Scintillation Screens and Optical Technology for Transverse Profile Measurements, Krakow, Poland, April, 2019, pp. 1–3, see for example https://indico.cern.ch/event/765975/contributions/3250550/attachments/1821689/2979882/Scintillating_Screens_at_BNL_Toby_Miller.pdf.
- [100] Ernst-Eckhard Koch (Ed.), Handbook on Synchrotron Radiation, Vol. 1a, North-Holland Publishing Company, New York, 1983.
- [101] Helix Coaxial Cable, See For Example, <http://www.rfparts.com/coax/helixcoax.html>.
- [102] K.B. Unser, Design and preliminary tests of a beam intensity monitor for LEP, in: Proceedings of the 1989 IEEE Particle Accelerator Conference, Vol. 1, 1989, p. 71.
- [103] J. Musson, K. Cole, S. Rubin, Application of Goubau surface wave transmission line for improved bench testing of diagnostic beamline elements, in: PAC 2009, 4-8 2009, Vancouver, British Columbia, Canada..
- [104] L. Couch, Digital and Analog Communications, fourth ed., MacMillan Coll Div., 1993.
- [105] Walter Barry, A general analysis of thin wire pickups for high frequency beam position monitors, Jefferson Lab technical note, CEBAF PR-90-024.
- [106] J.R. Taylor, An Introduction to Error Analysis, University Science Books, 1982.
- [107] M. Spata, T. Allison, K. Cole, J. Musson, J. Yan, Evaluation and correction of the non-linear distortion of CEBAF beam position monitors, in: Proceedings of 2011 Int'L. Particle Accelerator Conference, San Sebastian, Spain, 2011, pp. 1440–1442.
- [108] Buddhini P. Waidyawansa, A 3% Measurement of the Beam Normal Single Spin Asymmetry in Forward Angle Elastic Electron-Proton Scattering using the Qweak Setup, (Ph.D. thesis), Ohio University, 2013, https://misportal.jlab.org/ul/publications/downloadFile.cfm?pub_id=12540.
- [109] Riad Suleiman, Roger Flood, John Hansknecht, Scott Higgins, Helicity Control Board User's Guide: Programming and Hardware, Jefferson Lab Technical Note JLAB-TN-20-037, 2020.
- [110] D.S. Armstrong, B. Moffitt, R. Suleiman, Target Boiling, Target Density Fluctuations and Bulk Boiling in Hall A Cryotarget, JLAB-TN-03-017, Jefferson Lab Technical Note, 2003.
- [111] D. Ramsay, False asymmetry from fixed-frequency noise in the Qweak DAQ, Qweak document database, 2009, QweakDocDB-906.
- [112] D. Ramsay, Acceptance of the Qweak DAQ in the frequency domain, Qweak document database, 2008, QweakDocDB-732-v2.
- [113] D. Ramsay, Use of DAQ patterns to cancel types of noise, Qweak document database, QweakDocDB-888.
- [114] P. Nepal, P. King, Helicity Pattern Evaluation, for the MOLLER Collaboration, Ohio University, 2022.
- [115] W. Diamond, The injector for the CEBAF CW superconducting linac, 1987, p. 1907, PAC.
- [116] W. Diamond, R. Pico, Status of the CEBAF injector, 1988, p. 403, WE3-37, LINAC.
- [117] R. Kazimi, C.K. Sinclair, G.A. Krafft, Setting and measuring the longitudinal optics in CEBAF injector, in: LINAC, Monterey, CA, 2000, p. 125.
- [118] Y. Wang, A. Hofler, R. Kazimi, Commissioning of the 123 MeV injector for CEBAF, in: IPAC 2015, Richmond, VA, p. 1920.
- [119] R. Abbott, S. Benson, M. Crofford, D. Douglas, R. Gonzales, R. Kazimi, D. Kehne, G.A. Krafft, P. Liger, H. Liu, D. Machie, C. Sinclair, Design, commissioning and operation of the upgraded CEBAF injector, in: LINAC 1994, p. 777, TH-30.
- [120] R. Kazimi, Simultaneous four-hall operation for 12 GeV CEBAF, in: IPAC 2013, Shanghai, China, p. 3502.
- [121] R. Kazimi, H. Wang, J. Hansknecht, M. Spata, Source and extraction for simultaneous four-hall beam delivery system at CEBAF, in: IPAC 2013, Shanghai, China, p. 2896.
- [122] M. Breidenbach, M. Foss, J. Hodgson, A. Kulikov, A. Odian, G. Putallaz, H. Rogers, R. Schindler, K. Skarpaas, M. Zolotarev, An inverted-geometry, high-voltage polarized electron gun with UHV load lock, *Nucl. Inst. Meth.* 350 (1994) 1.
- [123] C.K. Sinclair, P.A. Adderley, B.M. Dunham, J.C. Hansknecht, P. Hartmann, M. Poelker, J.S. Price, P.M. Rutt, W.J. Schneider, M. Steigerwald, Development of a high average current polarized electron source with long cathode operational lifetime, *Phys. Rev. ST Accel. Beams* A10 (2007) 023501.
- [124] P.A. Adderley, J. Clark, J. Grooms, J. Hansknecht, K. Surles-Law, D. Machie, M. Poelker, M.L. Stutzman, R. Suleiman, Load-locked DC high-voltage GaAs photogun with an inverted-geometry ceramic insulator, *Phys. Rev. ST Accel. Beams* 13 (2010) 010101.
- [125] J.M. Grooms, P.A. Adderley, J.F. Benesch, J. Clark, J. Hansknecht, R. Kazimi, D. Machie, M. Poelker, M.L. Stutzman, R. Suleiman, Y. Zhang, Two Wien filter spin flipper, in: Proceedings of 2011 Particle Accelerator Conference, PAC'11, New York, NY, 2011.
- [126] J. Hansknecht, M. Poelker, Synchronous photoinjection using a frequency-doubled gain-switched fiber-coupled seed laser and ErYb-doped fiber amplifier, *Phys. Rev. ST Accel. Beams* 9 (2006) 063501.
- [127] V. Tioukine, K. Aulenbacher, Operation of the MAMI accelerator with a wien filter based spin rotation system, *Nucl. Instrum. Methods A* 568 (2006) 537.
- [128] J. Haimson, Two wien filter spin flipper, in: Proceedings of 2011 Particle Accelerator Conference, PAC'11, New York, NY, 2011.
- [129] J. Haimson, Technical Proposal for Design, Fabrication, Testing and Delivery of Two Bi-Mode 499 MHz Microwave Deflecting Cavities for the CEBAF Injector - Vol. 1, Jefferson Lab Technical Note, 22-023.
- [130] J.D. Lawson, The Physics of Charged Particle Beams, Oxford University Press, 1977.
- [131] Mark Crofford, Curt Hovater, George Lahti, Chip Piller, Matt Poelker, The RF system for the CEBAF polarized photoinjector, in: LINAC 1998, p. 552, TU4067.
- [132] G.A. Krafft, Correcting M56 and T56 to obtain very short bunches at CEBAF, AIP Conf. Proc. 367 (1996) 46, <http://dx.doi.org/10.1063/1.50330>, Published Online: 12 2008.
- [133] S. Wang, J. Guo, R.A. Rimmer, H. Wang, The new design for capture cavity of CEBAF, in: IPAC 2014, p. 3955, THPR1080.
- [134] C.W. Leemann, The CEBAF superconducting accelerator—An overview, in: LINAC 1986, Stanford, CA, p. 194.
- [135] C.W. Leemann, D.R. Douglas, G.A. Krafft, The continuous electron beam accelerator facility: CEBAF at the Jefferson Laboratory, *Annu. Rev. Nucl. Part. Sci.* 51, 413–450, <http://dx.doi.org/10.1146/annurev.nucl.51.101701.132327>, (Volume publication date 2001).
- [136] General particle tracer, pulsar physics, <http://www.pulsar.nl/gpt>.
- [137] Gisela Pöplau, Ursula van Rienen, Bas van der Geer, Marieke de Loo, Multigrid algorithms for the fast calculation of space-charge effects in accelerator design, *IEEE Trans. Magn.* 40 (2) (2004) 714.
- [138] S.B. van der Geer, O.J. Luiten, M.J. de Loos, G. Pöplau, U. van Rienen, 3D space-charge model for GPT simulations of high brightness electron bunches, *Inst. Phys. Conf. Ser.* (175) (2005) 101.
- [139] K. Aulenbacher, Operating experience with the MAMI polarized electron source, in: Proceedings of the Workshop on Photocathodes for Polarized Electron Sources for Accelerators, SLAC 432-Rev. SLAC, Stanford, CA, 1994, p. 1.
- [140] Wei Liu, Shukui Zhang, Marcy Stutzman, Matt Poelker, Effects of ion bombardment on bulk GaAs photocathodes with different surface-cleave planes, *Phys. Rev. Accel. Beams* 19 (2016) 103402.
- [141] J. Grooms, R. Suleiman, P.A. Adderley, J. Clark, J. Hansknecht, D. Machie, M. Poelker, M.L. Stutzman, Charge and fluence lifetime measurements of a DC high voltage GaAs photogun at high average current, *Phys. Rev. ST Accel. Beams* 14 (2011) 043501.
- [142] Md Abdullah A. Mamun, Abdelmageed A. Elmustafa, Marcy L. Stutzman, Philip A. Adderley, Matthew Poelker, Effect of heat treatments and coatings on the outgassing rate of stainless steel chambers, *J. Vacuum Sci. Technol. A* 32 (2014) 021604.
- [143] Marcy L. Stutzman, Philip A. Adderley, Md. Abdullah A. Mamun, Matt Poelker, Nonevaporable getter coating chambers for extreme high vacuum, *J. Vac. Sci. Technol. A* 36 (2018) 031603.

- [144] J.M. Grames, et al., CEBAF 200 kV inverted electron gun, in: Proc. PAC'11, New York, NY, USA, Mar.-Apr. 2011, pp. 1501–1503, paper WEODS3.
- [145] J.T. Yoskowitz, Ion Production and Mitigation in DC High-Voltage Photoguns (Ph.D. thesis), Old Dominion University, Norfolk, VA, 2022.
- [146] J.T. Yoskowitz, J. Grames, J. Hansknecht, C. Hernandez-Garcia, G.A. Krafft, G. Palacios-Serrano, M. Poelker, M.L. Stutzman, R. Suleiman, S.B. Van Der Geer, S. Wijethunga, Phys. Rev. Accel. and Beams (2023) in press.
- [147] C. Hernandez-Garcia, M. Poelker, J. Hansknecht, High voltage studies of inverted-geometry ceramic insulators for a 350kV DC polarized electron gun, IEEE Trans. Dielectr. Electr. Insul. 23 (1) (2016).
- [148] G. Palacios-Serrano, F. Hannon, C. Hernandez-Garcia, M. Poelker, H. Baumgart, Electrostatic design and conditioning of a triple point junction shield for a -200 kV DC high voltage photogun, Rev. Sci. Instrum. 89 (2018) 104703.
- [149] C. Hernandez-Garcia, D. Bullard, F. Hannon, Y. Wang, M. Poelker, High voltage performance of a DC photoemission electron gun with centrifugal barrel-polished electrodes, Rev. Sci. Instrum. 88 (2017) 093303.
- [150] J. Grames, Magic Energies for the 12 GeV Upgrade, Jefferson Lab Technical Note TJNAF-TN-04-042.
- [151] W. Wien, Untersuchungen über die elektrische Entladung in verdünnten Gasen, Ann. Phys. 301 (6) (1898) 440–452, <http://dx.doi.org/10.1002/andp.18983010618>.
- [152] K. Tsuno, D. Ioanoviciu, The Wien Filter, Advances in Imaging and Electron Physics, Vol. 176, Academic Press, 2013.
- [153] G. Palacios-Serrano, P. Adderley, H. Baumgart, J. Benesch, D. Bullard, J. Grames, C. Hernández-García, A. Hofler, D. Machie, M. Poelker, M. Stutzman, R. Suleiman, High voltage design and evaluation of wien filters for the CEBAF 200 keV injector upgrade, in: 12th Int. Particle Acc. Conf. IPAC2021, Campinas, SP, Brazil, <http://dx.doi.org/10.18429/JACoW-IPAC2021-MOPAB324>.
- [154] B. Steiner, W. Ackermann, W.F.O. Muller, T. Weiland, Wien filter as a spin rotator at low energy, MOPAN013, in: Proceedings of PAC07, Albuquerque, New Mexico, USA.
- [155] D.S. Armstrong, et al., G0 Collaboration, Transverse beam spin asymmetries in forward-angle elastic electron-proton scattering, Phys. Rev. Lett. 99 (2007) 092301, <http://dx.doi.org/10.1103/PhysRevLett.99.092301>.
- [156] D. Androic, et al., G0 Collaboration, Transverse beam spin asymmetries at backward angles in elastic electron- proton and quasi-elastic electron-deuteron scattering, Phys. Rev. Lett. 107 (2011) 022501, <http://dx.doi.org/10.1103/PhysRevLett.107.022501>.
- [157] S. Abrahamyan, et al., HAPPEX, PREX Collaborations, New measurements of the transverse beam asymmetry for elastic electron scattering from selected nuclei, Phys. Rev. Lett. 109 (2012) 192501, <http://dx.doi.org/10.1103/PhysRevLett.109.192501>.
- [158] D. Androic, et al., QWeak Collaboration, Precision measurement of the beam-normal single-spin asymmetry in forward-angle elastic electron-proton scattering, Phys. Rev. Lett. 125 (2020) 112502, <http://dx.doi.org/10.1103/PhysRevLett.125.112502>.
- [159] D. Androic, et al., Measurement of the beam normal single spin asymmetry for elastic electron scattering from ^{12}C and ^{27}Al , Phys. Rev. C 104 (2021) 014606, <http://dx.doi.org/10.1103/PhysRevC.104.014606>.
- [160] D. Adhikari, et al., New measurements of the beam-normal single spin asymmetry in elastic electron scattering over a range of spin-0 nuclei, Phys. Rev. Lett. 128 (2022) 142501, <http://dx.doi.org/10.1103/PhysRevLett.128.142501>.
- [161] J.D. Lawson, The Physics of Charged Particle Beams, Oxford University Press, 1977.
- [162] P. Franken, A. Hill, C. Peters, G. Weinreich, Generation of optical harmonics, Phys. Rev. Lett. 7 (4) (1961) 118, <http://dx.doi.org/10.1103/PhysRevLett.7.118>.
- [163] R. Boyd, The nonlinear optical susceptibility, in: Nonlinear Optics, third ed., ISBN: 9780123694706, 2007, pp. 1–67, <http://dx.doi.org/10.1016/B978-0-12-369470-6.00001-0>.
- [164] See, for example, P.T. Ho, Picosecond Optoelectronic Devices, Academic, New York, 1984.
- [165] S. Zhang, M. Poelker, A versatile and highly reliable green-light drive laser for high current photoinjectors, Jefferson Lab Tech Note 21-037.
- [166] At CEBAF, there are four beam modes: OFF, CW, viewer-limited and tune-mode. CW stands for continuous wave and describes electron bunches present during every RF cycle (note, since the 12 GeV CEBAF upgrade, there are some empty RF buckets during four hall operation). Viewer-limited and tune-mode represent reduced duty factor conditions.
- [167] J. Hansknecht, Tune mode generator alignment procedure, https://wiki.jlab.org/ciswiki/index.php/Tune_Mode_generators.
- [168] J. Hansknecht, Tune generator design package 2017, https://wiki.jlab.org/ciswiki/index.php/Tune_Mode_generators.
- [169] M. Roth, N. Angert, M. Tseitlin, G. Wang, T.P.J. Han, H.G. Gallagher, N.I. Leonyuk, E.V. Kopolulina, S.N. Barilo, L.A. Kurnevich, Recent developments in crystal growth and characterization of nonlinear optical borate and phosphate materials, in: Proceedings of the III International Conference Single Crystal Growth, Strength Problems, and Heat and Mass Transfer, Vol. 2, Obninsk, 2000, pp. 416–426.
- [170] E. Lebiush, R. Lavi, Y. Tsuk, N. Angert, A. Gachechiladze, M. Tseitlin, A. Zharov, M. Roth, RTP as a Q-switch for high repetition rate application, in: Proceedings of the Conference Advanced Solid-State Lasers, in Trends Opt. Photonics Ser., Vol. 34, 2000, pp. 63–65.
- [171] C. Sinclair, Time Response Requirement for the BLM/FSD System, Jefferson Lab Tech Note TN 92-046.pdf.
- [172] Beth Schaefer, Edward Collett, Robert Smyth, Daniel Barrett, Beth Fraher, Measuring the Stokes polarization parameters, Amer. J. Phys. 75 (2007) 163, <http://dx.doi.org/10.1119/1.2386162>.
- [173] E. Wolf, Optics in terms of observable quantities, Nuovo Cimento 12 (1954) 884–888.
- [174] J. Hansknecht's summary of helicity flipping and Pockels cells used at CEBAF: http://www.jlab.org/accel/inj_group/laser2001/pockels_files/pockels_switch_notebook.htm.
- [175] Joseph F. Stephany, Piezo-optic resonances in crystals of the dihydrogen phosphate type, 1965, pp. 136–142, <http://dx.doi.org/10.1364/JOSA.55.000136>, 55 (2).
- [176] Caryn Palatchi and Kent Paschke, RTP Pockels Cell with Nanometer-Level Position Control, arXiv:2106.09546v1.
- [177] M. Roth, N. Angert, M. Tseitlin, Potassium titanyl phosphate (KTP) - an oxide of choice for nonlinear optical and electro-optic applications, in: Proceedings of the 2nd Israeli-Russian Workshop on the Optimization of Composition, Structure and Properties of Metals, Oxides, Composites, Nanomaterials and Amorphous Materials, Jerusalem, 2003, pp. 233–235.
- [178] M. Roth, N. Angert, M. Tseitlin, G. Wang, T.P.J. Han, H.G. Gallagher, N.I. Leonyuk, E.V. Kopolulina, S.N. Barilo, L.A. Kurnevich, Recent developments in crystal growth and characterization of nonlinear optical borate and phosphate materials, in: Proceedings of the III International Conference Single Crystal Growth, Strength Problems, and Heat and Mass Transfer, Vol. 2, Obninsk, 2000, pp. 416–426.
- [179] E. Lebiush, R. Lavi, Y. Tsuk, N. Angert, A. Gachechiladze, M. Tseitlin, A. Zharov, M. Roth, RTP as a Q-switch for high repetition rate application, in: Proceedings of the Conference Advanced Solid-State Lasers, in Trends Opt. Photonics Ser., Vol. 34, 2000, pp. 63–65.
- [180] Kazutaka Nakahara, in: Advisor D.H. Beck (Ed.), Measurement of the Strange Quark Contribution to Proton Structure Through Parity Violating Electron-Proton Scattering (Ph.D. thesis, Thesis No.: 1832), University of Illinois, Champaign-Urbana, 2006.
- [181] Frederick E. Terman, Radio Engineers' Handbook, McGraw-Hill, 1943.
- [182] Emmanouil Kargiantoulakis, A Precision Test of the Standard Model Via Parity-Violating Electron Scattering in the Qweak Experiment (Ph.D. thesis), University of Virginia, 2015, <https://qweak.jlab.org/DocDB/0022/002276/002/dissertation.pdf>.
- [183] S. Peggs, T. Satogata, Introduction to Accelerator Dynamics, Cambridge University Press, 2017.
- [184] Y. Chao, Generation and control of high precision beams at Lepton accelerators, in: Proceedings of Particle Accelerator Conference, Albuquerque, New Mexico, 2007.
- [185] Y. Chao, et al., CEBAF accelerator achievements, J. Phys. Conf. Ser. 299 (2011) 012015.
- [186] Y. Chao, Linac skew quad calibration, 2003, http://www.jlab.org/chao/Skew_quad_calib.pdf.
- [187] Alex Bogacz, Phase trombone for parity experiments, JLAB-TN-07-039.
- [188] C. Reece, Cornell University Laboratory of Nuclear Studies SRF Note No. SRF860201EXA, 1986.
- [189] C.G. Yao, Effects of Field Asymmetry in the Coupler, Jefferson Laboratory Tech Note CEBAF-TN-89-183, 1989.
- [190] G. Wu, H. Wang, C.E. Reece, R.A. Rimmer, Waveguide coupler kick to beam bunch and current dependency on SRF cavities, in: SRF Workshop 2007, Peking.
- [191] F.E. Hannon, A. Hofler, R. Kazimi, Optimizing the CEBAF injector for beam operation with a higher voltage electron gun, in: PAC'11, New York, 2011, pp. 2023–2025, WEP288.
- [192] R. Kazimi, A. Freyberger, F.E. Hannon, A. Hofler, A. Hutton, Upgrading the CEBAF injector with a New Booster, higher voltage gun, and higher final energy, in: Proc. IPAC'12, New Orleans, LA, USA, 2012, pp. 1945–1947, paper TUPPR055.
- [193] H. Wang, et al., Injector cavities fabrication, vertical test performance and preliminary cryomodule design, WEPW030, in: IPAC 2015.
- [194] H. Wang, 12 GeV CEBAF injector quarter CryoModule (QCM) SRF cavities specification document, QCM project document, April 3, 2015.
- [195] H. Wang, Reconstruction of cavity to coupler transition field from 3D eigen solutions, 2013, JLAB TN publication in April.
- [196] H. Wang, G. Cheng, F. Hannon, A. Hofler, R. Kazimi, J. Preble, R.A. Rimmer, RF design optimization for new injector cryo unit at CEBAF, in: Proc. IPAC'13, Shanghai, China, 2013, pp. 2471–2473, Paper WEPW0073.
- [197] G. Cheng, J. Henry, J. Mammossier, R.A. Rimmer, H. Wang, M. Wiseman, S. Yang, Mechanical design of a new injector cryomodule 2-cell cavity at CEBAF, in: Proc. PAC'13, Pasadena, CA, USA, 2013, pp. 880–882, paper WEPAC47.

- [198] G. Cheng, M. Drury, J. Fischer, R. Kazimi, K. Macha, H. Wang, JLAB new injector cryomodule design, fabrication and testing, in: 18th International Conference on RF Superconductivity, SRF2017, Lanzhou, China, JACoW Publishing, ISBN: 978-3-95450-191-5, <http://dx.doi.org/10.18429/JACoW-SRF2017-MOPB045>.
- [199] F. Marhauser, H. Wang, Quadrupole decomposition of the C100 cavity accelerating field, JLAB-TN-09-016, Thomas Jefferson National Accelerator Facility, Newport News, VA.
- [200] Dennis L. Turner, Software tools for emittance measurement and matching for 12 GeV CEBAF, in: Proceedings of IPAC2016, Busan, Korea, <http://dx.doi.org/10.18429/JACoW-IPAC2016-WEPOR053>.
- [201] T. Suwada, M. Satoh, K. Furukawa, Nondestructive beam energy-spread monitor using multi-strip-line electrodes, Phys. Rev. ST Accel. Beams 6 (2003) 032801, <http://dx.doi.org/10.1103/PhysRevSTAB.6.032801>.